ABSTRACT

Title of dissertation: *IN SITU* GROWTH AND DOPING STUDIES OF TOPOLOGICAL INSULATOR BISMUTH SELENIDE

Jack Hellerstedt, Doctor of Philosophy, 2015

Dissertation directed by: Professor Michael Fuhrer
Department of Physics

The past decade has borne witness to the rapid development of a new field of theoretical and experimental condensed matter physics commonly referred to as "topological insulators". In a (experimentalist's) single sentence a topological insulator can be thought of as material that behaves like an empty metal box: the i-dimensional material (i = 2,3) is insulating, but conducting states exist at the (i-1)-dimensional boundaries. These edge or surface states possess non-trivial properties that have generated interest and excitement for their potential utility in solving practical problems in spin electronics as well as the creation of condensed matter systems for realizing and testing new physics. The most extensively studied materials systems with these properties suffer a major drawback in that the interior of the metal box is not "empty" (insulating) but instead filled with metal. The goal of this work has been to understand why the box is full instead of empty, and explore a particular pathway to making it empty.

To address these outstanding questions in the literature pertaining to the per-

sistent n-doping of topological insulator Bi_2Se_3, a custom apparatus was developed for combined epitaxial thin film growth with simultaneous, *in situ* measurement of transport characteristics (resistivity, Hall carrier density and mobility). Bi_2Se_3 films are found to be n-doped before exposure to ambient conditions and this doping appears to be interfacial in origin. This work and methodology was extended to study the efficacy of an amorphous MoO_3 capping layer. MoO_3 acts as an electron acceptor, p-doping the Bi_2Se_3 up to a $|\Delta n| = 1\text{x}10^{13}$ cm^{-2} change in carrier density. Complimentary X-ray photoemission spectroscopy (XPS) on bulk crystals showed that this was enough to put the Fermi level into the topological regime. Thin films were too highly n-doped initially to reach the topological regime, but the same magnitude change in doping was observed via the Hall effect. Finally, a Bi_2Se_3 film with a 100 nm capping layer of MoO_3 was vented to ambient, and found to retain a stable doping for days of ambient exposure, demonstrating the effectiveness of MoO_3 for passivation.

IN SITU GROWTH AND DOPING STUDIES OF TOPOLOGICAL INSULATOR BISMUTH SELENIDE

by

John Thery Hellerstedt

Dissertation submitted to the Faculty of the Graduate School of the
University of Maryland, College Park in partial fulfillment
of the requirements for the degree of
Doctor of Philosophy
2015

Advisory Committee:
Professor Michael Fuhrer, Chair/Advisor
Professor Johnpierre Paglione
Professor Ian Appelbaum
Professor Victor Galitski
Professor Janice Reutt-Robey

Table of Contents

List of Figures

List of Abbreviations

AFM	Atomic Force Microscopy
HOMO	Highest Occupied Molecular Orbital
LUMO	Lowest Unoccupied Molecular Orbital
MBE	Molecular Beam Epitaxy
RHEED	Reflection High Energy Electron Diffraction
STI	Strong Topological Insulator
STM	Scanning Tunneling Microscopy
UHV	Ultra High Vacuum
WTI	Weak Topological Insulator
XPS	X-ray Photoemission Spectroscopy

Chapter 1: Introduction

1.1 General Introduction

Topological Insulators are a recently discovered class of materials that have already been the subject of literature reviews from various subfield perspectives [18] [19] [20] [21] [22], as well as a (now dated, but) definitive and comprehensive review in *Reviews of Modern Physics* [23]. The purpose of this chapter is to give a brief overview of the origins of the field, and subsequently focus on current literature concerning bulk doping and surface impurities in these materials, which will be relevant to the subsequent chapters of this thesis.

The field of condensed matter physics has long been defined by Landau's classification of matter and phase transitions according to symmetry breaking. The most accessible example of this is the phase transition of water from liquid to ice. Liquid water's constituent molecules, while highly correlated, lack long range order: liquid water has continuous translational and rotational symmetry. Ice is crystalline, conforming to a lattice, so translational symmetry becomes discrete instead of continuous, and rotational symmetry is broken. In magnetism, the Curie temperature can be described in terms of breaking rotational symmetry (paramagnetic states are rotationally symmetric; Ferro-, Ferri-, and Antiferromagnetic states aren't). The

most simple superconducting transition is described by the energy gap order parameter, understood in terms of gauge symmetry breaking. Despite this breadth in applicability of symmetry breaking, the beginning of the 1980's saw the discovery of the quantum Hall effect, experimental evidence that symmetry breaking was not a universally applicable explanation for distinguishing new phases.

The (integer) quantum Hall effect is observed in a two dimensional electron gas subjected to an out of plane magnetic field. The effect of the magnetic field is to force the electrons into cyclotron orbits at discrete values of energy called Landau levels. This leads to the well known quantization of Hall conductivity:

$$\sigma = \frac{e^2}{h}\nu \; ; \; \nu \in \mathbb{Z} \tag{1.1}$$

Initially observed by von Klitzing in 1980 [24], figure (1.1) shows a more illustrative experimental realization of the plateaus caused by the quantization of the transverse conductivity.

What is clear from the figure is that the system is transitioning between distinct, measurably different states described by different integers ν, but in this case there is no simple explanation using symmetry breaking. Instead, the language and mathematics of topological order has been used to explain these transition phenomena.

The first explanation of this effect was offered by Laughlin, who analyzed the problem using the magnetic flux through a cylindrical ring geometry [25]. Limitations to this approach were pointed out by Thouless, Kohmoto, Nightingale and

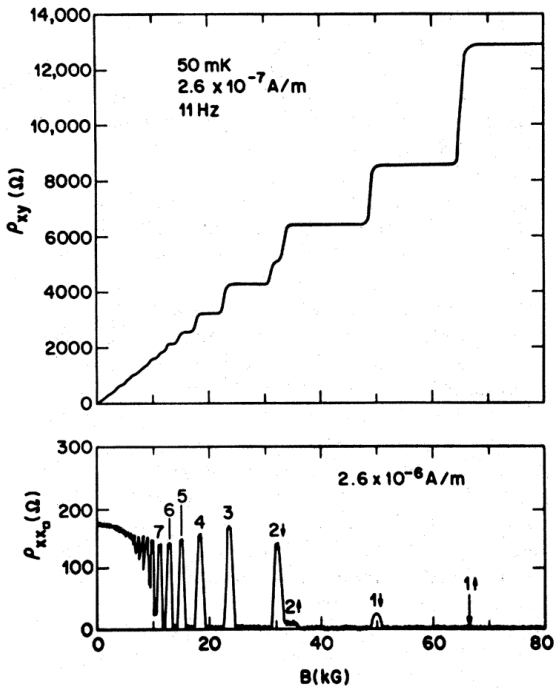

Figure 1.1: Transverse (ρ_{xy}) and longitudinal (ρ_{xx}) resistances measured against perpendicular magnetic field in a GaAs-$Al_xGa_{1-x}As$ 2DEG, demonstrating the integer quantum Hall effect. Figure reproduced from reference [1].

den Nijs (TKNN), who used the Kubo linear response formula on a periodic torus surface to derive the same quantized conductance [26]. The phase space geometry of the TKNN result in particular is crucial to making the connection to the underlying mathematics.

The Gauss-Bonnet theorem from the field of differential geometry connects the integral of the Gaussian curvature (K) over a closed two-dimensional surface (S) to the Euler characteristic of the surface:

$$\frac{1}{2\pi}\int_S KdA = \chi(S) \in \mathbb{Z} \tag{1.2}$$

Chern showed that this result could be generalized to a broader class of manifold [27]. This result allowed for the Gauss-Bonnet theorem to be applied instead to the integration over the Brillouin zone of the 'curvature' of wavefunctions, which is better known as the Berry curvature (the bracketed quantity in eq. 1.3) [28]:

$$\frac{i}{2\pi}\int_{BZ} d^2k\,[\nabla \times \langle u_m|\nabla_k|u_m\rangle] = n_m \in \mathbb{Z} \tag{1.3}$$

Here the m subscript refers to the particular band, and the $|u_m\rangle$ refer to the Bloch wavefunctions. The integer in this case is refered to as the Chern number for the m^{th} band. Shortly after the TKNN result was derived, Avron *et al.* identified the underlying mathematics of their method as a particular Chern class [29], [30]. In a recent review of the field [18], Ando provided a simple calculation using perturbation theory to derive the quantized Hall conductivity in a 2D system of electrons, equation (1.1), where he reduces his expression for the Hall conductivity $\sigma_{xy} = \frac{\langle j_x\rangle}{E_y}$

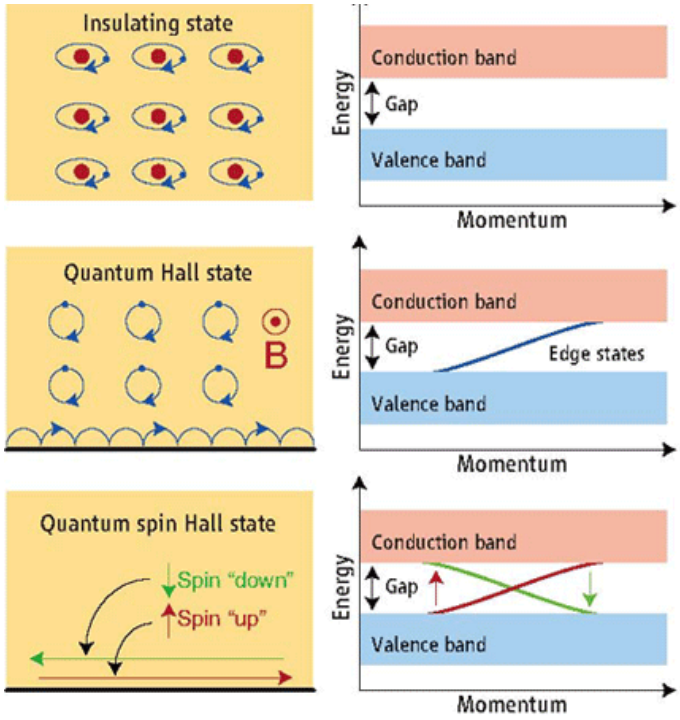

Figure 1.2: Illustration of the distinction between quantum and spin quantum Hall effects. The left hand images are in real space, the right hand images show the corresponding dispersion relations. Figure reproduced from references [2], [3].

(current density at right angle to the E-field direction) to an expression involving the Berry phase:

$$\sigma_{xy} = \frac{e^2}{h} \sum_n \frac{i}{2\pi} \int_{BZ} d^2k [\nabla \times \langle u_{nk} | \nabla_k | u_{nk} \rangle]$$

where the summation in n counts the contributing bands, and the expression integrated over the Brillouin zone is exactly equation (1.3), and therefore an integer. In this simple model of a square 2D electron system of finite size, with an applied out of plane magnetic field and in plane electric field, the Hall conductance is quantized in multiples of e^2/h: in this case the topological mathematics of the Chern number can be thought of as 'counting' the number of contributing bands.

The topological description of the quantum Hall effect laid the groundwork

for the theoretical prediction of the so-called quantum spin Hall effect [31] [32] [33]. While the Hall effect is the spatial separation of different charges due to a magnetic field, the spin Hall effect is the momentum separation of different spin states as the result of application of an electric field. This difference is highlighted in figure 1.2, which illustrates the difference between three different states. In an insulating state, electrons are highly localized, which manifests itself as the presence of a gap in the band structure. The quantum Hall state is characterized by the presence of a magnetic field causing the electrons to "run loops", where the loop size is quantized. This motivates a simple way to think about the presence of an edge state, where the loop-like path of the electron repeatedly runs into the boundary of the conduction media, imposing a momentum direction. The quantum spin Hall effect comes from a spin orbit interaction term instead of an external magnetic field. This means that electrons with opposite spin states have to be traveling in opposite directions, which leads to unusual boundary phenomena: these phenomena are why topological insulators are so interesting.

The advantage of using the aforementioned Chern classification scheme is that it can be expanded to quantitatively describe the more complicated quantum spin Hall edge states. Kane and Mele extended the Chern class idea by introducing a so called Z_2 topological invariant [34]. To get to the Z_2 invariant, it is instructive to start with Haldane's model for graphene [4].

He considered in particular a periodic local magnetic flux density "with the full symmetry of the lattice, and with zero total flux through the unit cell", visualized in detail in figure (1.3). He showed that despite no net magnetization, it was possible to

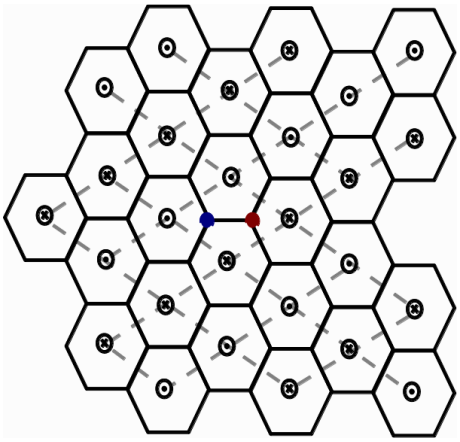

Figure 1.3: Illustration of the Haldane model for graphene. The grey dotted lines delineate the unit cells of graphene (enclosing the two sublattices- blue and red dots). The dots and crosses represent the periodic placement of magnetic dipole moments leading to zero total flux through each unit cell. Figure created based on the description in reference [4].

break time reversal symmetry, which leads to an integer quantum Hall state, instead of just a trivial semiconductor. Kane and Mele's essential innovation [34] was to expand the Haldane model in a time reversal symmetric manner by including spin-orbit interaction terms, as a way of accounting for spin. They considered the time reversal operator on a two band model using mathematics common in conformal field theory, constructing an integer result to a contour integration in the Brillouin zone whose result (odd or even) determines if the system in question exhibits the quantum spin Hall phase (odd) or is a trivial insulator (even)- the Z_2 invariant. They further studied spin orbit coupling in graphene to see if the quantum spin Hall effect might be experimentally accessible [35]; this was subsequently shown to be unrealistic because the effect would be too weak [36]. An alternate route to the Z_2 index was given by Xu and Moore [37], a many-body approach exploiting the time reversal symmetry condition and Kramers degeneracy, allowing them to investigate

the stability of the quantum spin Hall state to interactions and disorder. Bernevig and Zhang also studied this problem, using a strain gradient to induce quantization, strictly preserving time reversal symmetry [33]. They extended this work to make a concrete theoretical prediction for finding this state in HgTe quantum wells [38], experimentally verified thereafter [39].

Figure 1.2 provides a simple illustration highlighting the similarities and differences between the quantum, and quantum spin Hall effects. In both instances one sees edge states produced by an external field acting on the electrons. However, here the distinction of the time reversal symmetry become manifest: the QSHE is symmetric in momentum about the edge state crossing point, where no such symmetry exists in the QHE band diagram. One can also see that the spin states are momentum segregated in the QSH state, no such distinction being present in the QH state.

This discussion has so far been limited to two dimensions. However, the Kane and Mele [34] description of the underlying topological invariants allowed for generalizations of Z_2 into higher dimension. Kane and Mele's original work on Z_2 was first extended to three dimensions by Moore and Balents, who used homotopy theory to show that in 3D, each band pair is characterized by four Z_2 integers instead of just one [40]. Building on this work, Fu, Kane and Mele offered a different approach to the four Z_2 integers $\nu_0;(\nu_1\nu_2\nu_3)$, and an interpretation of the latter three as related to the Miller indices of the reciprocal lattice space [5]. The Z_2 integers are calculated relative to the time reversal invariant momentum (TRIM) points from the reciprocal lattice vectors. They enumerate the different ways a Fermi arc can

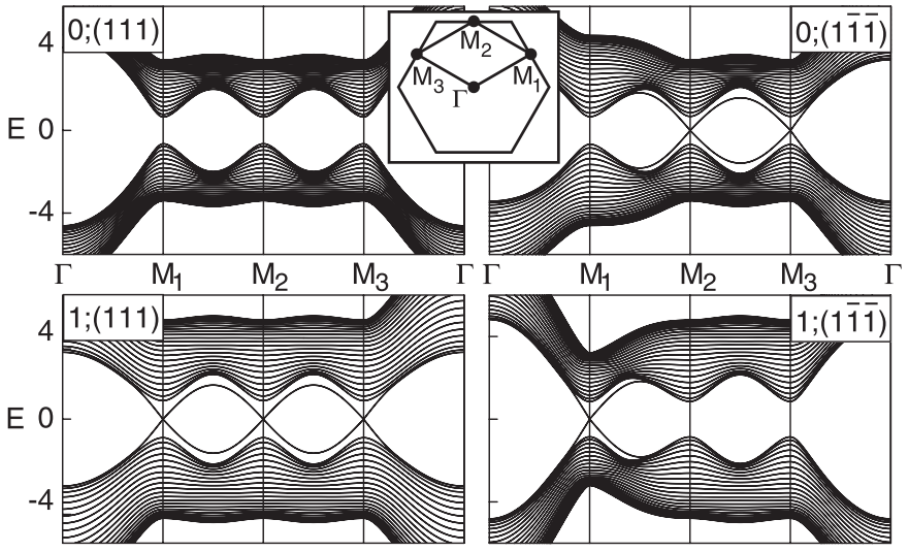

Figure 1.4: Band structure calculation for a (111) slab of diamond lattice. The four subplots are different phases labelled according to their Miller indices. In the top (bottom) two diagrams ν_0=0 (1), and there are an even (odd) number of crossings at E=0. Figure reproduced from [5].

enclose the TRIM points in the brillouin zone. The parity of the first index ν_0 defines two broad categories: $\nu_0 = 0$ are weak topological insulators (WTI), where the consequent $\nu_{1,2,3}$ indices force an even number of Dirac points enclosed by the surface Fermi arc. This makes these surface states susceptible to localization as a result of disorder. The strong topological insulator (STI) case is when $\nu_0 = 1$: an odd number of Dirac points are enclosed by the surface Fermi arc. This introduces a π Berry phase to the electron wave function, suppressing back-scattering [41], the phenomena commonly referred to as "topological protection" and assigned in real space to the surface. This time-reversal symmetric 3D topological insulator state will be the major topic of this thesis and I will refer to it generically as "topological insulator" in the subsequent chapters.

They employed this analysis to consider a tight binding model of a diamond

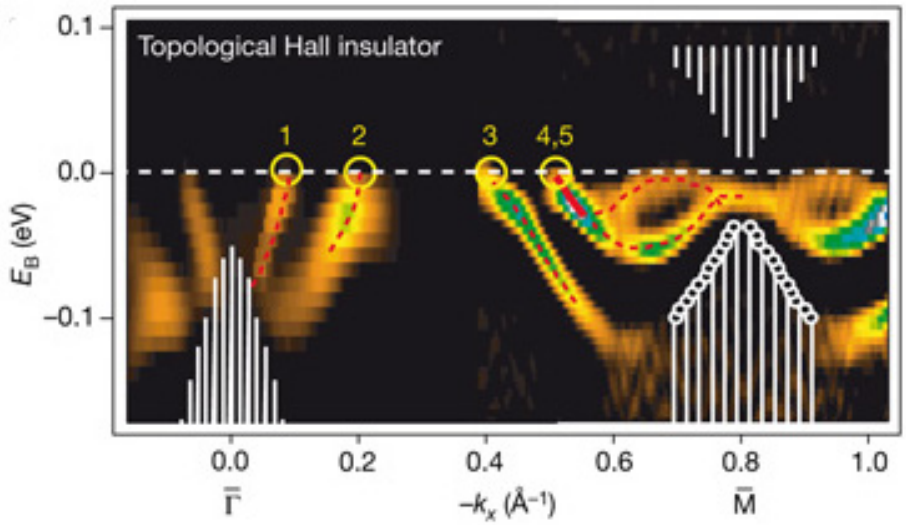

Figure 1.5: ARPES measurement of $Bi_{0.9}Sb_{0.1}$ along $\bar{\Gamma} - \bar{M}$. The white lines are a projection of bulk band data, the yellow circles indicate the (odd) number of surface state Fermi level crossings. Figure reproduced from reference [6].

lattice with the spin-orbit interaction, and saw these different (weak, strong) phases in different crystallographic directions. Figure 1.4 shows their band structure computations for different sets of topological indices, where this odd/even paradigm is explicitly manifest in the number of Dirac cone band crossings at E=0.

Fu *et al.* [5] also built a tight binding model and applied their results to bismuth, in consideration of Murakami's work showing that bismuth would be a good candidate material in which to try and realize the quantum spin Hall state [42]. Further work by Fu, Teo, and Kane tightened theoretical predictions for the specific alloy system $Bi_{1-x}Sb_x$ [43], [44]. This was within months of the first experimental work on the same material system, where angle resolved photoemission spectroscopy (ARPES) showed an odd number of Fermi level crossings providing evidence for the topological nature of the material (figure 1.5) [6]. ARPES utilizes a source of high intensity photons (e.g. a synchrotron) to photoexcite electrons in a given sample;

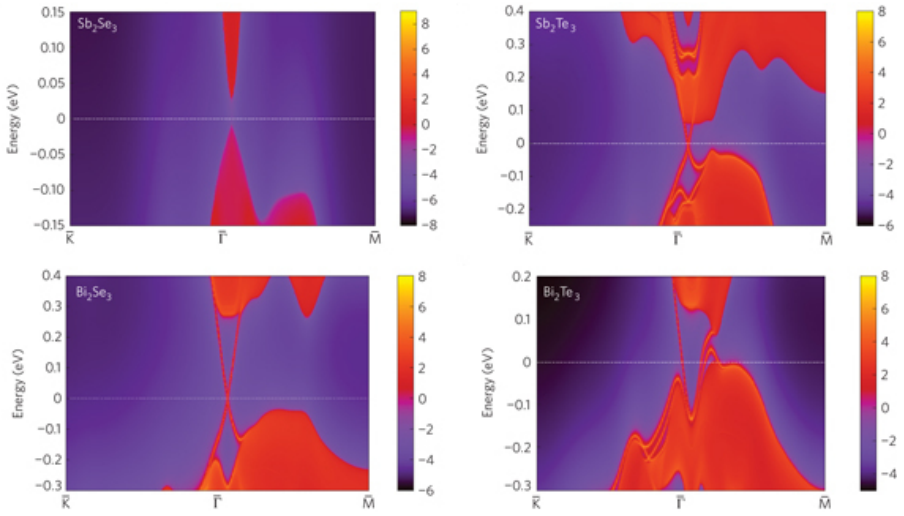

Figure 1.6: Energy and momentum dependence for the denoted chalcogenide systems calculated theoretically using density function theory. The red color indicate a higher local density of states, the presence of a band. Figure reproduced from reference [7].

measuring the momentum of these electrons directly maps the band structure (E vs. k). This means that figures 1.5 and 1.4 are plotting the same things, albeit for different material systems, and experiment vs. theory.

However, $Bi_{1-x}Sb_x$ is an alloy. This means there isn't an easily defined crystalline structure, making it hard to model theoretically. For this reason, Zhang et al. chose instead to investigate the layered stochiometric crystals Sb_2Te_3, Sb_2Se_3, Bi_2Te_3, and Bi_2Se_3 (figure 1.6) [7].

Their first-principles calculations predicted both a single Dirac cone crossing and a bulk gap of 0.3 eV for Bi_2Se_3, notable for how it is an order of magnitude larger than the energy scale of room temperature, 0.025 eV. This was experimentally confirmed by Hasan's group, who had moved to the Bi_2Se_3 system from $Bi_{1-x}Sb_x$ for the same reasons [8]. They grew single crystal of Bi_2Se_3 via the Bridgeman

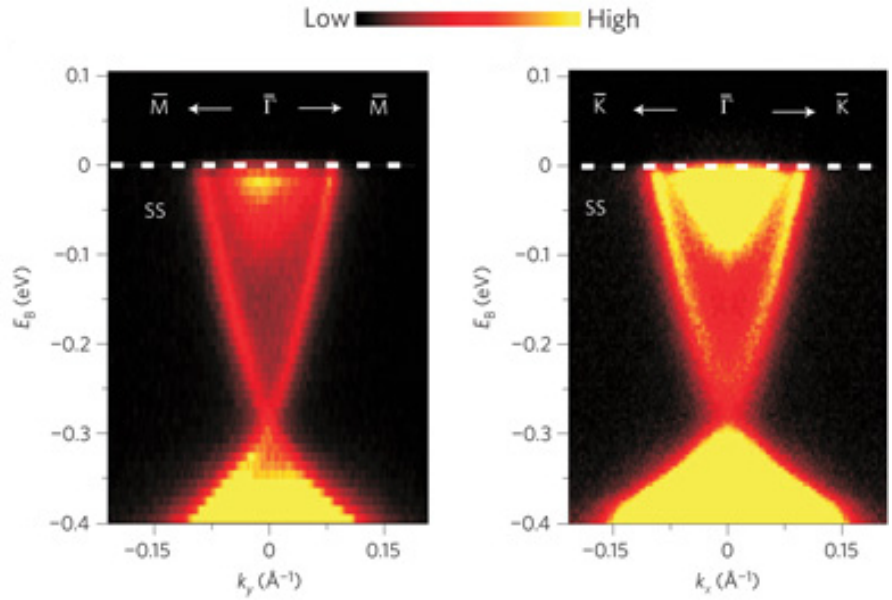

Figure 1.7: First experimental ARPES measurement of surface electronic band dispersion for cleaved Bi_2Se_3 single crystal, taken along two different momentum-space cuts. The bright red 'Dirac cone' is evidence of the surface state for example predicted in the lower left of figure 1.6. Note the position of the Fermi level (0 E_B) in the bulk conduction band. Figure reproduced from reference [8].

method, which was subsequently cleaved in vacuum and characterized by ARPES (figure 1.7).

The spin-correlated 'Dirac'-like dispersion of the surface states is the core concept of topological insulators. Expanding the nuance and complexity of our understanding of condensed matter systems has intrinsic value, in the spirit of Anderson's manifesto 'More is Different' [45], but has generated additional excitement for the regions of previously unexplored physics these systems could be used as a building block to access. Qi and Zhang do a good job outlining in broad strokes some of the potential applications, notably heterostructures that would act like magnetic monopoles, or exhibit non-Abelian statistics [2]. A less esoteric application would be the obvious utility of control of spin-correlated surface conduction states in de-

veloping practical spin electronics, a possibility broadly outlined by Pesin and MacDonald [22]. These exciting avenues of new physics and applications have generated considerable excitement, but formidable obstacles remain before their realization. The data in figure (1.7) clearly demonstrates an immediate experimental shortcoming that is the subject of active research. As noted in the caption, the position of the Fermi level in the system is far into the bulk conduction band, making this sample of Bi_2Se_3 a bulk conductor, instead of a bulk insulator. These bulk states in practice make the surface states of interest incredibly hard to detect in any experimental transport scheme, a necessary precursor for exploiting their unusual properties. The following sections review various approaches to dealing with this problem.

1.2 Experimental Approaches to Access Topological Surface States

There are several experimental routes to making surface state phenomena more prominent in a transport measurement, among them chemical doping to move the Fermi level, and designing the geometry of the device to increase the ratio of surface to bulk contribution. The drawback to chemical doping is the disorder into the system it necessarily introduces. Preparation methods that allow the control of surface/bulk ratio (thin film or nanowire growth) generally produce materials of much lower quality than bulk grown crystals. For the purposes of accessing the surface states, there are also various schemes of electrostatically tuning the Fermi surface into the bulk gap of the chalcogenide material systems.

This series of bismuth-based chalcogenides have been studied extensively in

the past for their thermoelectric properties, so their crystal structure [46] and bulk characteristics [47] have been known for decades, while the 'surface states' have only been subject to much more recent scrutiny. As recently as 2002, Bi_2Se_3 was being discussed in terms of its thermoelectric properties, establishing from ARPES data that bulk crystals are *n*-doped [48], also noted by Xia *et al.* [8]. This issue of doping has been studied extensively from the perspective of optimizing thermoelectric material systems, in particular *n*-type Bi_2Te_3 [49].

The crystal structure of these chalcogenides is notable in having quintuple layers of alternating bismuth and selenium or tellurium that are strongly bonded to one another (figure 1.8). However, between the quintuple layers, the bonding is of the weaker van der Waals type [7]. This makes the bulk crystal resemble graphene in that the 'scotch tape' method pioneered by Geim's group to exfoliate thin layers of graphite [50] can be applied to make similarly thin flakes and therefore potentially reduce the bulk contribution to transport. In addition to bulk exfoliation, it is also possible to grow these materials by molecular beam epitaxy (MBE) on a variety of substrates [51] [52] [53]. This process is referred to as "van der Waals epitaxy" because of the inter-quintuple-layer bonding; this particular bonding allows films of these materials to be grown on substrates with a large lattice mismatch.

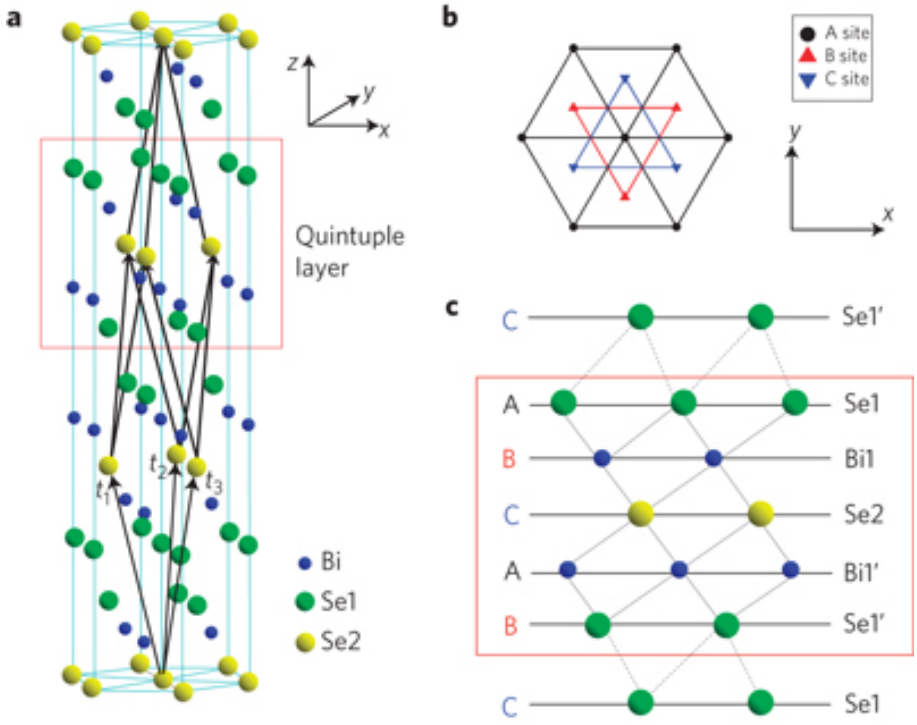

Figure 1.8: Bi_2Se_3 crystal structure, with additional side view of the stacking order. Figure reproduced from reference [7].

1.2.1 Chemical Mediation for Bulk Suppression

1.2.1.1 Se Vacancies

Selenium vacancies are universally cited as one of the leading reasons for the persistent n- doping of even the most meticulously prepared bulk crystals of Bi_2Se_3 [54]. This has been confirmed by direct STM/STS measurement of Se defect sites (see for example [55]). Various other approaches beyond preparation of the most stoichiometric Bi_2Se_3 possible are also being extensively researched.

1.2.1.2 Chemical Substitution

One approach to addressing the intrinsic doping problem of bismuth selenide involves substitutional doping. Initial efforts focused on calcium doping of Bi_2Se_3 to compensate for the electron doping produced by selenium vacancies (figure 1.9, [56] [9]).

Devices fabricated from similarly Ca- compensated bulk Bi_2Se_3 have shown evidence of having sufficiently low initial bulk carrier density to be successfully gated into the surface state dominant regime [57]. Pb and Sb have also been shown to successfully move the Fermi surface from above to below the Dirac point [58].

1.2.1.3 Stoichiometries Beyond Binary Compounds

More recent work has focussed on even more complicated stoichiometries involving Bi, Sb, Se, and Te (see for example [59], [60], [61] [62]). A review of ternary

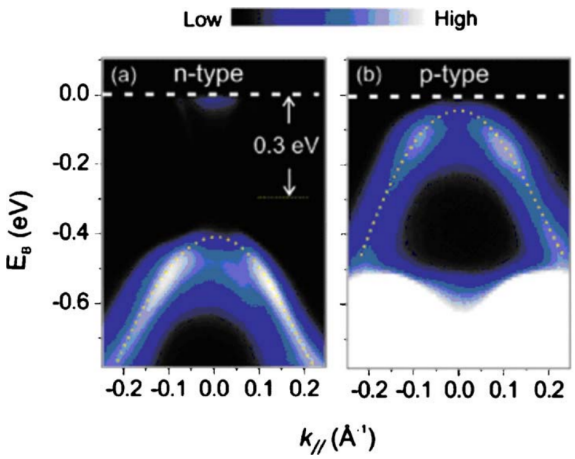

Figure 1.9: ARPES data comparing n-type Bi_2Se_3 (left) with $Bi_{1.98}Ca_{0.02}Se_3$ (right), showing a clear change in the position of the bulk bands. The explanation in the paper leaves ambiguous whether only observing the bulk bands (no evidence of the surface state in the gap) was deliberate. Figure reproduced from reference [9].

compounds beyond just the bismuth based materials has recently been completely by the Hasan group [63], [64]. One of the most recent transport works available on the Bi_2Te_2Se system identifies the crossover temperature from bulk to surface conduction at 30K [65], which is still a far way off from ready electronic access at room temperature.

In the so-called BSTS system, the specific stoichiometry of $Bi_{1.5}Sb_{0.5}Te_{1.7}Se_{1.3}$ has very promising transport characteristics. Lee *et al.* calculate that their samples have a bulk:surface conductance ratio of 26% (6%) at 290 K (4.2 K) [66]. In more recent work using crystals of $Bi_{1.5}Sb_{0.5}Te_{1.8}Se_{1.2}$, Wang *et al.* reported an 8% surface conductance contribution at low temperature, where they analyzed their data with respect to surface, bulk and impurity bands [62]. STM [67] and ARPES [68] studies provide evidence that the Fermi level can be tuned to the Dirac point with the correct composition.

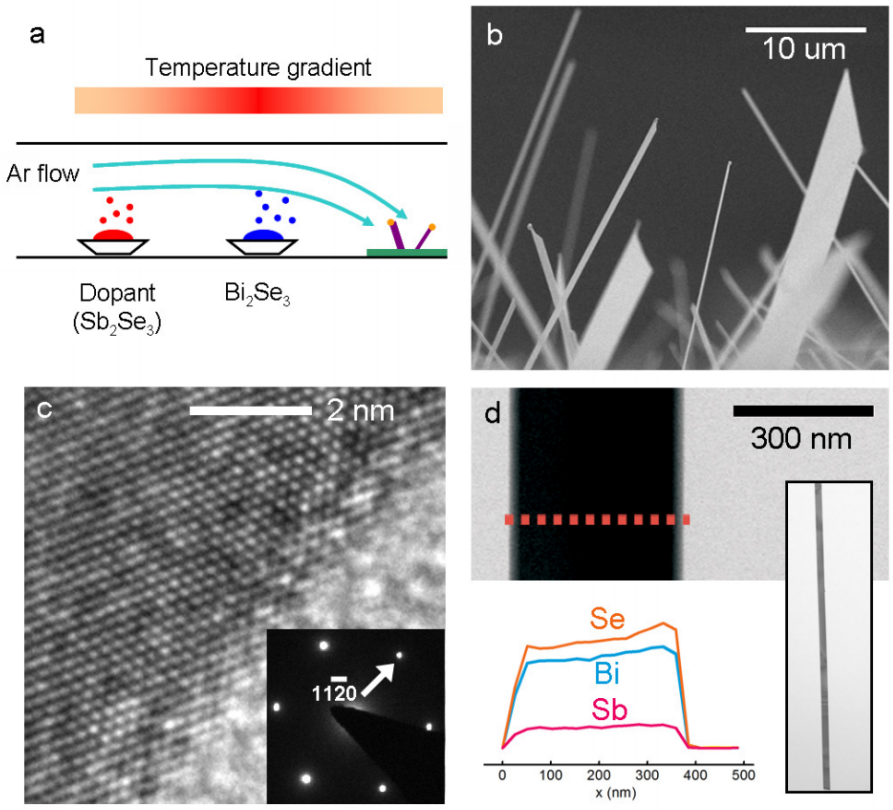

Figure 1.10: Schematic showing vapor-liquid-solid growth technique, and resultant nanoribbons of $(Bi_{1-x}Sb_x)_2Se_3$, characterized by SEM (b) and TEM (c). d) is an EDX profile showing the consistency of dopant introduced. Figure reproduced from reference [10].

1.2.2 Geometric Suppression of Bulk States

Nanoribbons by construction favor surface effects over the bulk, because of the favorable ratio of surface area to volume. Various efforts have shown success in using a vapor-liquid-solid growth technique to grow nanoribbons of Bi_2Se_3 (figure 1.10) [69] [10].

Hong *et al.* [10] showed that subsequent Sb doping combined with a ZnO protective layer allowed them to access the ambipolar transport region associated

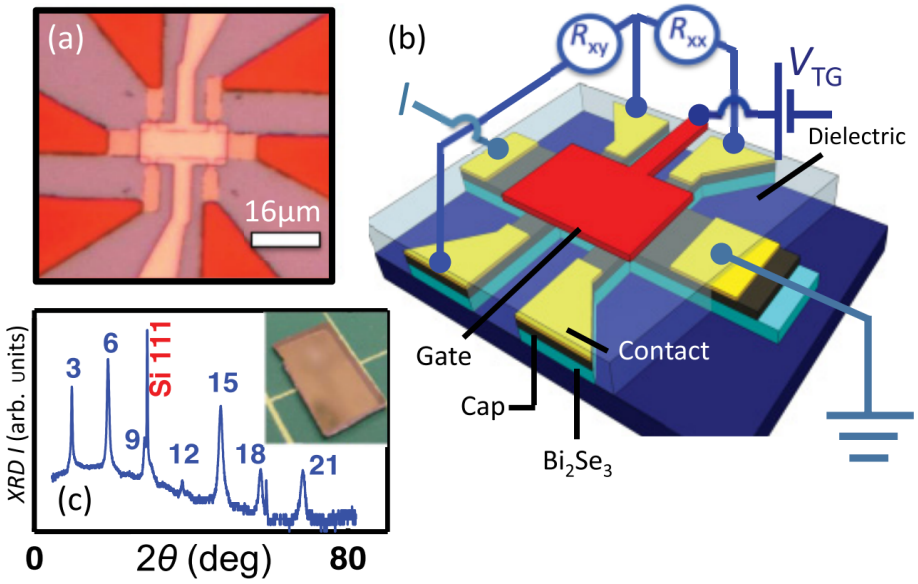

Figure 1.11: a) shows an optical image of the particular photopatterned device with contacts and a top gate. b) shows the general scheme for top and bottom gating. c) is X-ray diffraction data giving a measure of the quality of the Bi_2Se_3 film, indicating that it is growing in the c-axis direction, matching the substrate termination used. Figure reproduced from reference [11].

with surface transport [12].

1.2.3 Electrostatic Gating

There now exists a host of literature using both bulk exfoliated and thin film devices with various gating schemes to quantify the transport properties of these materials. Photopatterned devices of bismuth selenide and telluride have been gated from the top [11] [70], and also through the substrate [71]. Figure (1.11) is broadly representative of the general device geometry used. Figure (1.12) shows representative transport evidence for successful gating from n-doped to p-doped, through the bulk gap.

Band bending has been employed in a variety of experimental studies to de-

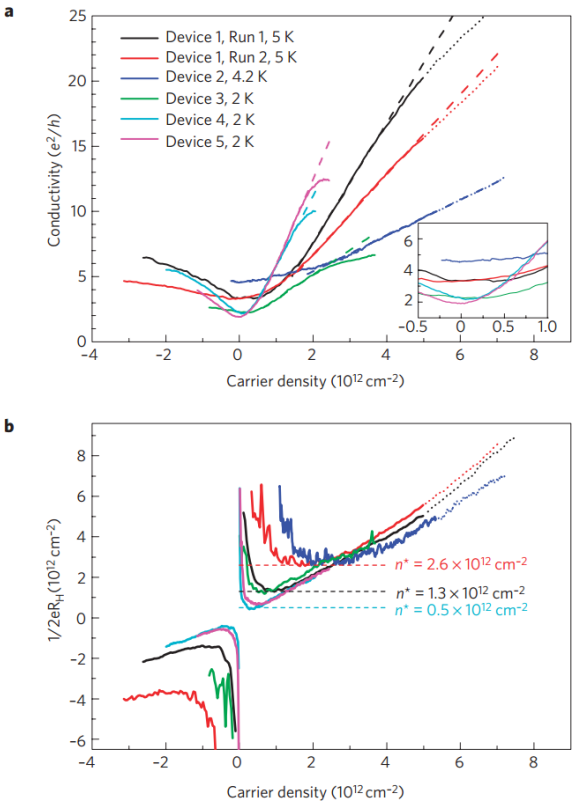

Figure 1.12: Exfoliated Bi_2Se_3, gated with an electrochemical double layer capacitor scheme. a) shows the conductivity minimum (Dirac point) achieved in a variety of samples as a function of the carrier density, extracted from Hall data. b) shows the change in sign of the charge carriers, indicating a transition from n- to p-doped material. Here n^* is the residual carrier density, attributed to electron and hole puddles. Figure reproduced from reference [12].

scribe the various conduction schemes involving the bulk, top and bottom surfaces [72] [11] [73] [10] [57]. It has also been used theoretically to connect the initial n-doping of these materials with their subsequent poor bulk resistivity [74]. Checkelsky *et al.* attribute a reduction in the size of the bulk band gap to band bending, with negative implications for accessing the surface states at room temperature [57]. Steinberg et al. lay out a very careful argument using interfacial band bending to explain where the Fermi surface sits at the top and bottom surfaces in their exfoliated, top and bottom gated flakes of Bi_2Se_3 [73]. However, this is hard to reconcile with recent results from Kim *et al.*, who showed no difference between the effects of back or top gate, suggesting that the surfaces are electrostatically coupled (difference in thickness between the two studies) [12]. Band bending could still be relevant in the presence of charge traps in the bulk, or large dopant compensation, due to the amounts of charge that are being electrostatically compensated. It could also be the case that the temperature dependence interpreted as activation from bulk valence to surface conduction bands in the Kim study was incorrectly attributed to band bending in refs. [57] and [73]. This is speculative at this time and remains an area of active research.

1.3 Magnetic Impurities

The spin-orbit interaction is time reversal symmetric. The degeneracy at the Dirac point is protected by time reversal symmetry: the two states are a Kramers pair thus must be degenerate as long as there is time reversal symmetry. Introducing

magnetic impurities would break time reversal symmetry in a localized manner, in particular affecting the surface states of the topological insulator. Initial theory work demonstrated magnetic impurities suppressing the local density of states, opening a local gap [75]. Subsequent theoretical work is more material specific, for example first principles calculations for Co impurities on Bi_2Se_3 [76], or Mn doping of Bi_2Te_3 [77]. Schmidt *et al.* conclude that Co doping opens a gap [76], while Henk *et al.* compute a non-trivial surface spin texture, and survival of the surface state [77]. This same diversity of results is present in the experimental literature on doping with magnetic impurities. Both magnetic and nonmagnetic impurities (Cs, Gd, Rb) deposited on bulk Bi_2Se_3 with concurrent ARPES, showed identical, negligible degradation of the surface state (figure 1.13) [13].

A substantial number of studies done using Fe as a dopant have also yielded conflicting conclusions. Studies of Fe deposited on the surface of Bi_2Se_3 have been interpreted as evidence of opening a band gap [78] [79], and lack of a band gap [80]. A later STM study showed an in-plane magnetic anisotropy for Fe impurities, evidence that a gap is not opened [81]. X-ray magnetic circular dichroism of Fe and Co deposited on bulk cleaved Bi_2Te_3 concluded that the adatoms do not induce long range magnetic order [82]. This conclusion is supported by another STM work done with Co doping [83].

In contrast with all the surface dopant studies demonstrating how magnetic dopants do not destroy the surface states, thin films of Bi_2Se_3 grown with increasing concentrations of Cr [84], and Mn [85], show a transition from weak anti-localization to weak localization, with additional ARPES measurements supporting

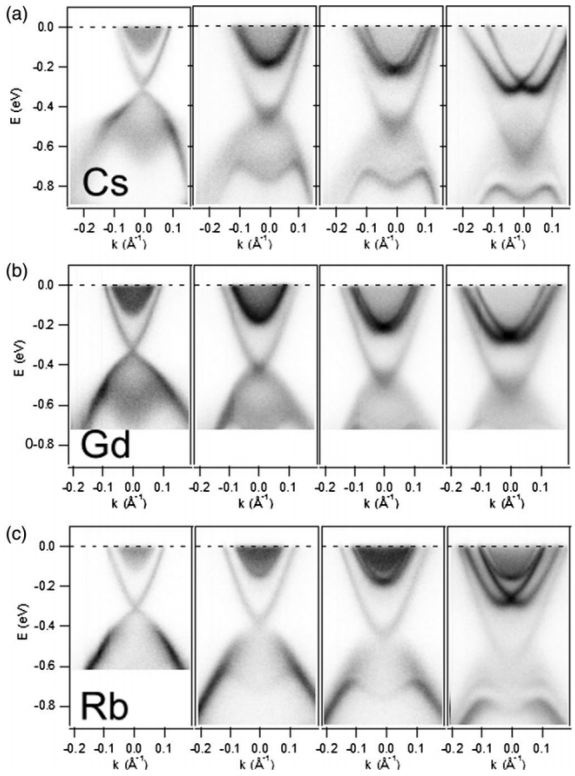

Figure 1.13: Cleaved, bulk Bi_2Se_3 with Cesium (a), Gadolinium (b) and Rubidium (c) adsorped on the surface. From left to right, pristine to maximally doped surface. Note the persistence of the surface bands despite increased doping. Figure reproduced from reference [13].

the conclusion that the surface states are suppressed. Similar work on Mn doped $Bi_2Te_{3-y}Se_y$ showed results suggesting one-dimensional conduction along magnetic domain walls [86], consistent with the picture that magnetic impurities will create local ferromagnetic domains without inducing long range ferromagnetic order.

1.4 Nonmagnetic Impurities

Another theoretical consequence of the π Berry phase and spin texture of topological insulator surface states is the predicted suppression of backscattering from nonmagnetic impurities on the surface. Evidence of this was inferred from the standing wave patterns observed by low temperature STM imaging of Ag impurities on the surface of Bi_2Te_3 film [87]. Similar work on Bi_2Se_3 showed intercalation of the Ag impurities into the quintuple layers, but ARPES results indicated that the surface states were preserved [88]. Ye *et al.* noted that while backscattering is theoretically prohibited under conditions of time reversal symmetry, scattering from arbitrary angles is not necessarily prohibited. Their work argues that the intercalation of Ag impurities pushes the real space location of the surface state into the bulk, away from the physical surface, which may provide an avenue for preserving its unique properties despite environmental exposure.

1.5 Environmental Effects

A great deal of work has been done characterizing the response of the chalcogenides to environmental exposure, work directly related to the doping problems

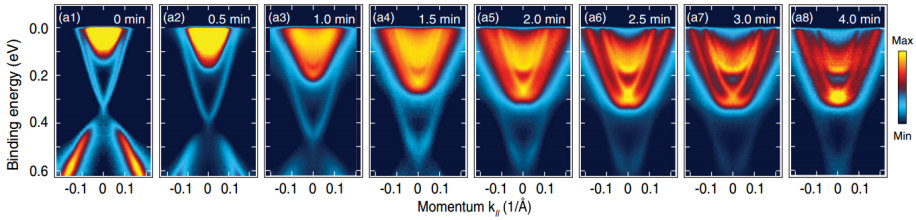

Figure 1.14: ARPES data of bulk cleaved Bi_2Se_3 systematically exposed to Potassium. Evidence of Rashba splitting in the more heavily doped spectrum (degeneracy lifted in momentum), and shift of the Fermi level further into the bulk conduction band. Figure reproduced from reference [14].

previously discussed in the context of transport studies. Degradation of the surface state attributed to oxidation has been measured in Bi_2Se_3 using x-ray photoelectron spectroscopy (XPS) [89]. An exfoliated bulk crystal of Bi_2Se_3 systematically exposed to trace amounts of water was demonstrated by ARPES to develop quantum well states at the surface, attributed to band bending [90]. This same effect was also observed in the $Bi_2(Se_{3-x}Te_x)$ system [91]. When potassium was used instead of water, the result was similar quantum well states developing on the surface, as well as a downward shift of the Dirac point (figure 1.14) [14]. This change in doping puts the Fermi level further into the bulk conduction band, away from the 'topological regime' where the surface states would be predominant in transport.

In a different study, a film of Bi_2Se_3 was exposed to atmosphere for days, and repeatedly measured. The magnetic field dependence was fit to a two-carrier model (surface and bulk carriers) [92]. They interpreted their measured increase in doping and decrease in mobility observed on exposure to atmosphere as predominately in the bulk state, and that the surface doping and mobility remained relatively stable. This supports an interpretation of the surface states being robust, but the bulk of

the material being acutely sensitive to environmental exposure. DFT focused on surface oxidation concluded that chemisorption of O_2 does not affect the existing surface states, where reaction with atomic O does effect a change [93]. There is a consensus in the literature that the particular chemistry associated with exposure to atmosphere (e.g. water and oxygen) is detrimental to achieving a low doping to make the surface states easily accessible in devices.

In work similar to the aforementioned studies done with Ag ([87] [88]), Rb deposited on Bi_2Se_3 measured via STM demonstrated evidence that Rb becomes intercalated upon annealing; subsequent ARPES indicates stability of bands to systematic oxygen exposure [94]. Bianchi *et al.* [94] have a similar conclusion to Ye *et al.* [88] about the feasibility of using intercalation to gain better control of the surface states.

1.5.1 Selenium Capping Layer

Another possible avenue to controlling the surface states, or at least minimizing the environmental effects, is a capping layer. Lang *et al.* grew Bi_2Se_3 film by MBE [95], with Shubnikov deHaas oscillations providing evidence that the presence of an *in situ* 2nm Al passivation layer on top of the TI film preserved the surface state of interest. As mentioned before, Hong *et al.* used a ZnO layer to protect their Bi_2Se_3 nanoribbons [10].

Another common method, especially with thin film growth, is to add a Se capping layer to protect the surface of the film [96] [84]. The ability to de-cap and

restore a pristine Bi_2Se_3 surface has been demonstrated via STM [97], and has been used in various studies involving bismuth selenide films (see for example [98], [99]).

1.6 Surface Transfer Doping

Surface transfer doping is another potential method to remove the n-type doping. It provides an alternative route to conventional bulk doping, as it does not involve introducing impurities into the bulk lattice and has been successfully implemented across a range of other materials [100] [101] [102] [103]. In the case of acceptor doping, high electron affinity molecules deposited onto the surface result in the transfer of electrons from the substrate into the molecular overlayer. This form of molecular doping on Bi_2Se_3 was recently demonstrated using the strong electron accepting molecule tetrafluorotetracyanoquinodimethane (F4-TCNQ) on mechanically exfoliated thin Bi_2Se_3 crystals on SiO_2/Si substrates. It was found that enough excess charge was removed to place the Fermi level near the conduction band edge, allowing the field-effect to be utilized to further tune the Fermi level through the topological regime [12] [104] [105].

Chapters 5 and 6 address this topic, specifically using molecular MoO_3 to p-dope Bi_2Se_3, demonstrate its stability as a capping layer, and develop a model to describe the charge transfer mechanism.

1.7 Current Material Limitations

Recent work about defects and the limitations they place on surface mobility suggest that aggressive chemical mediation is not an avenue to improvement that can be pursued limitlessly. Charged disorder in the Bi_2Se_3 system has been studied theoretically [106] and experimentally, both by transport [12] and STM [107]. Kim *et al.* measured mobilities and carrier density through the ambipolar regime (n- to p-type conduction transition) and found that the residual carrier density was proportional to the disorder [12]. Because dopant densities in bismuth selenide are typically on the order of 10^{13} cm^{-2}, this limits the mobility to ~ 1000 cm^2/Vs.

1.8 Summary & Open Questions

There remains a substantial gap between the bold theoretical predictions for topological insulators and what has been achieved experimentally to date. Substantial progress has been made in understanding the material limitations preventing access to the nontrivial surface states of interest. At the same time, theory pushing past symmetry breaking, further expanding our understanding of topological order, has continued to evolve. Notably, there has been rapidly expanding interest in so called 'topological crystalline insulators', labelled as such because lattice symmetries, instead of time reversal symmetry, are the basis of protected metallic surface states [108].

The following chapters of this thesis discuss experiments I performed to un-

derstand exactly how these issues of atmospheric exposure and doping arise and are related to the the carrier density of Bi_2Se_3 as it is grown in vacuum by molecular beam epitaxy. Additional experiments were performed to study various avenues of reducing the carrier density and passivate samples exposed to ambient conditions. Chapter 2 lays out the novel technique of growing an epitaxial thin film in vacuum while making simultaneous transport measurements, originally appearing as an SPIE conference proceeding [109]. Chapter 3 uses this technique to do a transport based growth study of Bi_2Se_3 thin films, to better understand the origins of the persistent n-doping in thin-film samples. These results appeared in *Applied Physics Letters* [110]. Chapter 4 is a second methods section outlining the technique of X-ray photoemission spectroscopy (XPS), which pertains to the results presented in chapter 5, where XPS was used to study the doping of Bi_2Se_3 using the molecular electron acceptor MoO_3, subsequently appearing in *ACS Nano* [111]. Chapter 6 discusses the transport aspects of the MoO_3 study in greater detail. Chapter 7 provides a final summary and outlook of future work.

Chapter 2: Methods I: Molecular Beam Epitaxy with Simultaneous Electrical Transport Measurements

2.1 General Introduction: Molecular Beam Epitaxy

Molecular beam epitaxy (MBE) refers to the process of growing crystalline materials in an ordered fashion ("epitaxially") on a substrate, through deposition of atomic or molecular reactants in stringent vacuum conditions. This allows for high purity, crystalline, single layer growth. MBE systems are typically equipped with anywhere from two to six reactant sources (or more), effusion cells or electron beam evaporators, a variable temperature growth stage, and apparatus to examine the crystallinity of the substrate and grown material, such as a reflection high energy electron diffraction system (RHEED). The vacuum chamber itself has a liquid nitrogen cooled shroud to maintain pressures in the 10^{-10} Torr or better during the growth process. By varying the relative flux densities of the various sources, the temperature of the substrate, and considering the initial substrate surface quality and lattice constant relative to the crystal structure of the film to be grown, the desired results can be achieved. RHEED gives real time continuous feedback about the crystallinity of the sample; by monitoring the diffraction pattern as it comes in

and out of focus, layer-by-layer control can be achieved.

The experimental challenge with topological insulators is making ready electronic access to the non-trivial edge and surface states, when there is interference from the trivial bulk states as a result of intrinsic material doping, as well as the subsequent effects of ambient exposure. Bismuth selenide exemplifies these challenges, having surface states of interest that are very difficult to separate from the trivial bulk conduction signals, as well as suffering material instabilities making it susceptible to doping when exposed to air, complicating *ex situ* device fabrication.

This project was originally conceived by graduate student Jianhao Chen to develop the ability to grow films by MBE while replacing the typical feedback apparatus (e.g., RHEED) with the ability to make real time, *in situ* electrical contact to the sample during and after growth. The rest of this chapter details how these instrumentation needs were met as well as the changes that had to be made on the sample side to make this possible. The essential feature is the placement of the growth stage simultaneously in a variable magnetic field while being inside the vacuum chamber. This required several key features: a growth stage with an electrical feedthrough for transport measurements, a stencil mask to exactly define the growth region, and the *ex situ* preparation of an insulating growth substrate with pre-wired, electrical contacts. These aspects will be discussed in greater detail in the following sections.

2.2 Electrical Transport

The electrical conductivity, carrier type and density, mobility, and how these properties respond as functions of temperature, magnetic field, are the parameter space of transport measurements in the broadest sense. There are a myriad of ways to measure these data; this section focusses on the Hall bar geometry used for the experiments in this thesis. This measurement geometry was chosen because it allows measurement of both components of the 2D resistivity tensor, eliminates the effect of contact resistance in measuring the resistivity tensor, is insensitive to how contact to the sample is made (no strict edge requirement like van der Pauw measurements), and lends itself to the fabrication of a physical stencil mask, the growth through which defines the measurement area.

2.2.1 Hall Effect

Considering the Lorentz force is how to understand the transverse Hall voltage and its relationship to the carrier density. An electron (charge q) in an electric field E moving with velocity v and magnetic field B feels a Lorentz force $\mathbf{F_{Lorentz}} = q(\mathbf{E} + \mathbf{v} \times \mathbf{B})$.

In the Hall bar geometry, an out of plane magnetic field $\mathbf{B}$ (figure 2.1, green inset) creates a lateral force ($\mathbf{F_{Lorentz}}$) on a moving electron ($\mathbf{v}$, from the applied current I_{SD}). This is balanced by the transverse potential that develops across the sample as a result of the charge accumulation:

$$\mathbf{F_{Lorentz}} = 0 = q|\mathbf{E}| + q|\mathbf{v}||\mathbf{B}| \rightarrow \frac{qV_{xy}}{W} = -q|\mathbf{v}||\mathbf{B}|$$

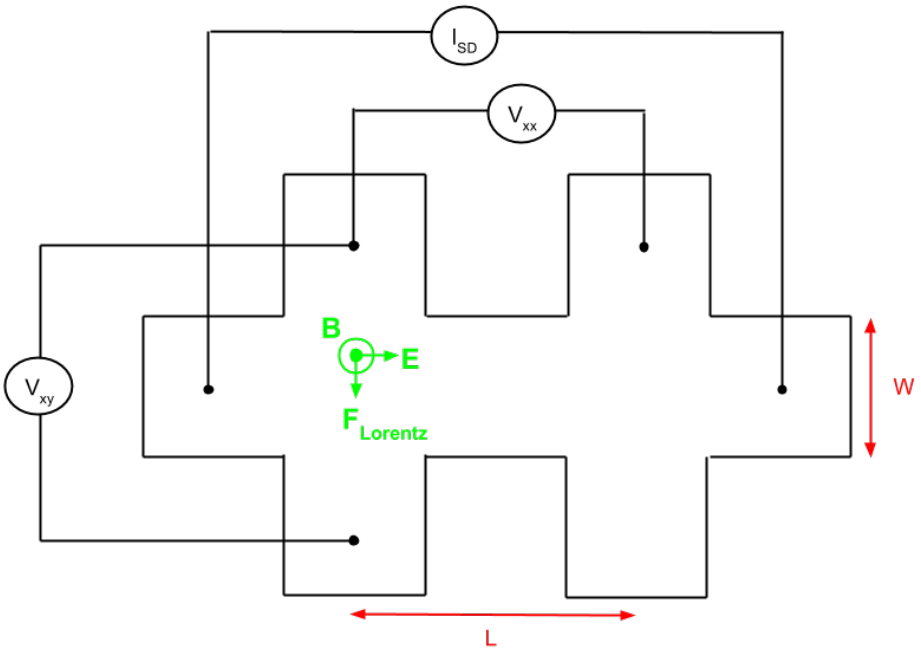

Figure 2.1: Hall bar measurement geometry. The length (L) and width (W) determine the length/width ratio (L/W). I_{SD} is the source- drain current, V_{xx} is the longitudinal voltage, and V_{xy} is the transverse voltage. The (green) inset shows the direction of the electric field, magnetic field (out of plane) and resulting Lorentz force.

Writing the (measurable) current I in terms of the volume charge density n_{3D}, geometric factors W, L, and t (sample thickness), and charge velocity $|\mathbf{v}|$:

$I = qnWt|\mathbf{v}| \rightarrow q|\mathbf{v}| = \frac{I}{n_{3D}Wt}$

Substituting this in to the Lorentz expression: $\frac{qV_{xy}}{W} = -\frac{I|\mathbf{B}|}{n_{3D}Wt}$

Solving for n in the case of electron conduction (q = e):

$\frac{1}{n} = e\frac{dR_{xy}}{dB}$

Where $n \equiv n_{3D}t$ is the two dimensional carrier density. Finally, note that in the case of the transverse signal, $V_{xy} = |\mathbf{E}|W$ and $I = jW$, where W is the width of the Hall bar, so the Hall resistivity is equivalent to the Hall resistance:

$$\rho_{xy} \equiv \frac{|\mathbf{E}|}{j} = \frac{V_{xy}/W}{I/W} = \frac{V_{xy}}{I} \equiv R_{xy} \tag{2.1}$$

So the expression for the carrier density can be written as:

$$\frac{1}{n} = e\frac{d\rho_{xy}}{dB} \tag{2.2}$$

With n, the mobility can be computed using the sheet resistance data:

$$\frac{1}{\mu} = ne\rho_{xx} \tag{2.3}$$

($\rho_{xx} = \frac{V_{xx}}{I}\frac{W}{L}$ is the sheet resistivity)

The sign of n indicates the carrier type (holes or electrons) and its magnitude is a direct measure of the integrated density of states. In the context of Bi_2Se_3, "doping" refers to how far up the Fermi level is in the conduction band, which is

exactly what n is indicating. Mobility can be interpreted as a figure of merit for the electrical conduction efficiency of a semiconductor which makes it a good measure of disorder. By these measures, "good" Bi_2Se_3 samples have low doping ($n = 0$ when $E_F = E_D$ in a naive sense) and high mobility.

2.2.2 AC vs DC measurements

AC lock-in measurement techniques have the advantage of working under low excitation power, a necessary condition for making measurements at low temperature. In contrast, making measurements at growth temperatures ($\sim$200°C) required a completely different approach. Geometric constraints limit how small and well defined the sample can be; the limited magnitude of the magnetic field also conspire to make the Hall signal small and difficult to measure. A 10 μA positive DC excitation was used in an effort to increase the size of the transverse Hall signal, which still required additional amplification using an SR560 voltage preamplifier. The transverse signal was generated by periodically sweeping the magnetic field through zero to positive and negative maximum values. The macroscopic nature of the sample causes a parasitic contribution of ρ_{xx} to the ρ_{xy} signal that was eliminated by subtracting a linear fit to the changing zero-field, ρ_{xx} signal from the linear fit of the $\rho_{xy}(B)$ transverse signal.

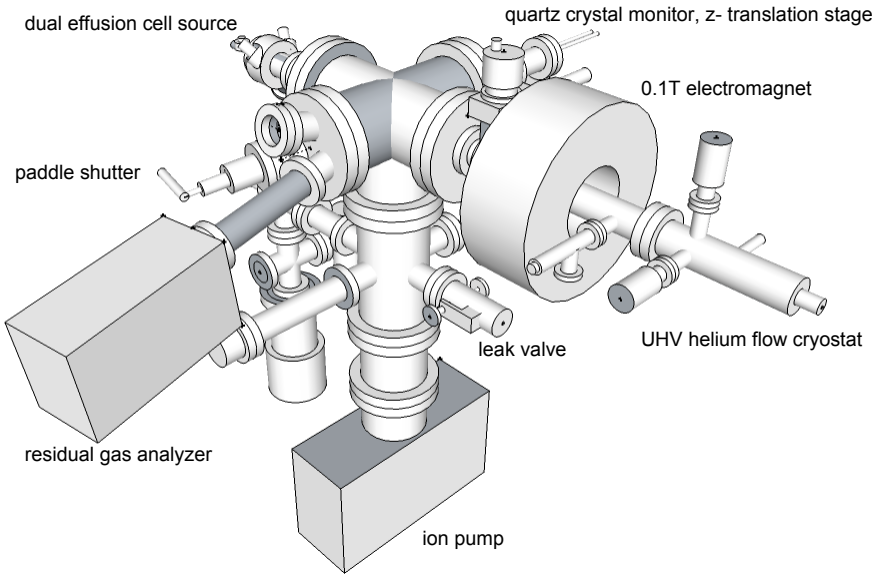

Figure 2.2: Scale diagram of in situ transport thin film growth chamber.

2.3 System Specific Details

2.3.1 Apparatus

To accomplish this *in situ* transport growth measurement, the apparatus in figure 2.2 was constructed. The working distance between the custom built, dual effusion cell source and the growth substrate is 30 cm. The growth substrate is mounted on a commercial UHV helium flow cryostat (Advanced Research Systems Inc. model no. LT3B-110), sitting centered in the bore of a GMW magnet systems (model no. 11901111) water cooled electromagnet capable of continuously sweeping the magnetic field strength from negative to positive 1100 Gs at the sample. The base pressure is 5x10^{-9} torr; during growth, the chamber pressure will rise to 1x10^{-7}

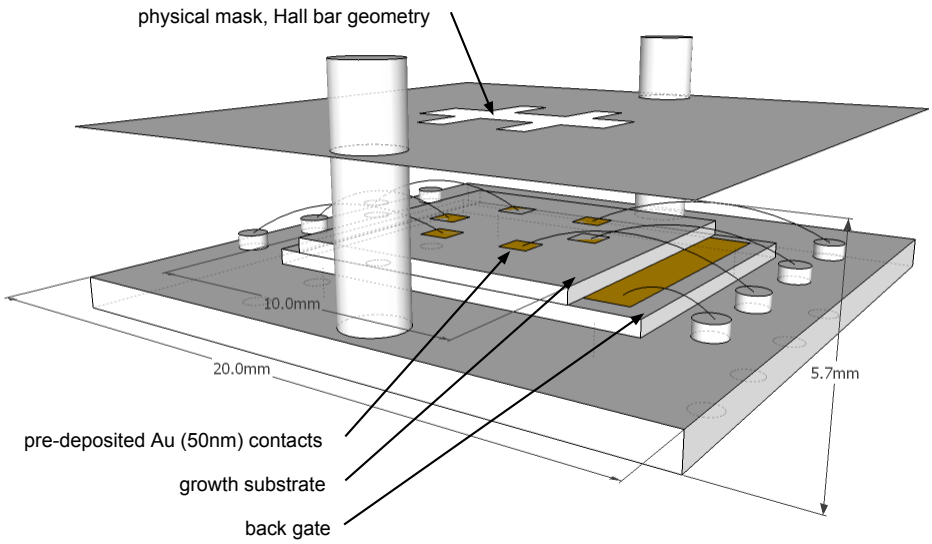

Figure 2.3: Scale diagram of substrate stage for film growth illustrating connections for simultaneous transport measurement.

torr.

2.3.2 Growth Stage

Figure 2.3 shows a detail of the growth stage: electrical contacts are pre-deposited on the substrate surface, and wire-bonded to pins connected through the cryostat. A physical mask mounted above the substrate ensures the growth of the film in the Hall bar geometry.

External heat tape at the cryostat, combined with a nichrome wire heater installed internally, directly underneath the growth stage allows for substrate growth temperatures between 100-250°C. Liquid helium cooling can reduce the sample tem-

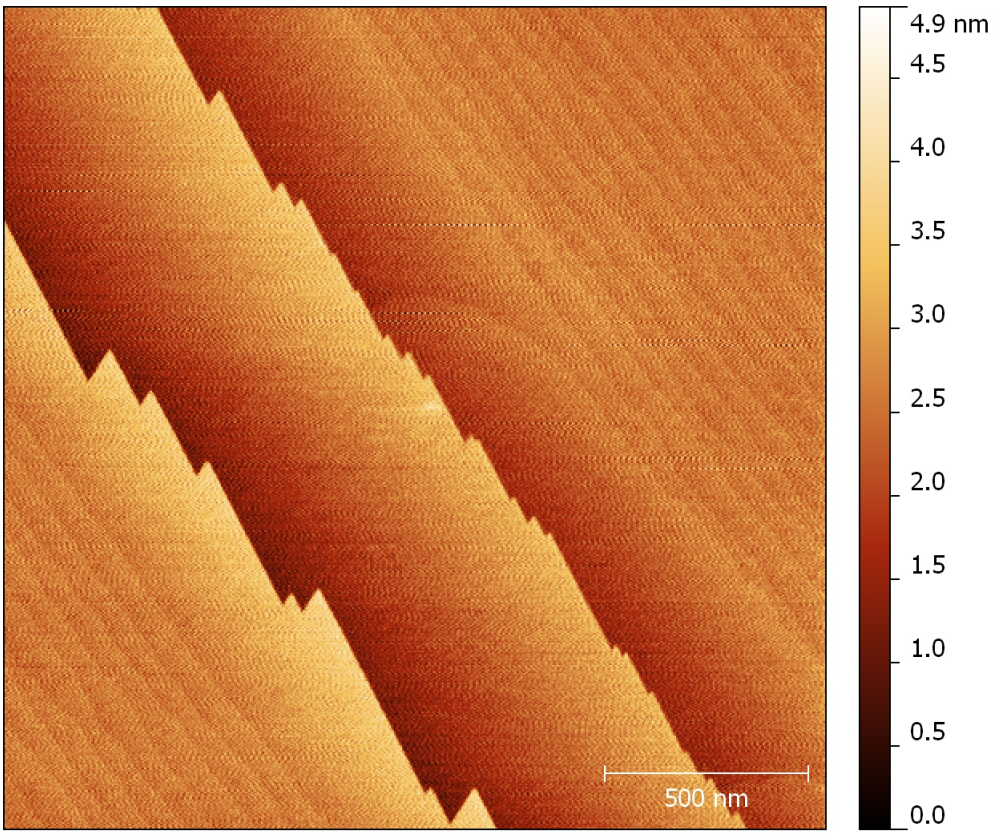

Figure 2.4: Atomic force microscopy (AFM) image of $SrTiO_3$ (111) substrate surface after oxygen annealing, showing lattice sized steps.

perature to 15 K. Because of this extreme operating temperature range, a platinum resistance thermometer was installed in the same position as the heater to provide thermal feedback control of the substrate growth temperature.

2.3.2.1 Substrate and Contact Preparation

For the experiments described in this thesis, $SrTiO_3$(111) is used as the substrate material. Annealing in oxygen produces an atomically-flat surface suitable for thin film growth [112]. The commercially procured substrate pieces were cleaned in solvent before being placed in a flow-through furnace. Under an oxygen gas flow

rate of 100 sccm, the substrates were heated from room temperature to 1050°C in one hour. 1050°C was maintained for 4-6 hours before cooling back down to room temperature at the natural rate of the furnace. Post annealing atomic force microscopy (AFM) was used to characterize the surface and determine the necessary length of time for the high temperature anneal. Figure 2.4 is a representative AFM image of the results of this annealing procedure, showing the atomically flat surface steps.

After annealing, a (wetting layer) 5 nm Ti (at 0.2 $\mathring{A}$/s) and 50 nm Au (2 $\mathring{A}$/s) are deposited by electron beam evaporation. A physical mask is used to deposit the contact pads underneath the corresponding ends of the Hall bar stencil mask, as indicated in figure 2.3. This thickness was chosen for ease of wire bonding; surprisingly electrical contact via growth of the sample film onto the gold pads was always reliably established even though the typical film thickness (10 nm) is much less than the gold contact height.

Single crystal strontium titanate has an exceptionally large (10^4) dielectric constant at cryogenic temperatures [113], making it possible to capacitively back-gate the film *in situ* despite the 500 μm substrate thickness. The maximum temperature of the cryostat growth stage prevent flash heating of the growth substrate to high temperatures, the typical method used for substrate surface preparation in vacuum [114].

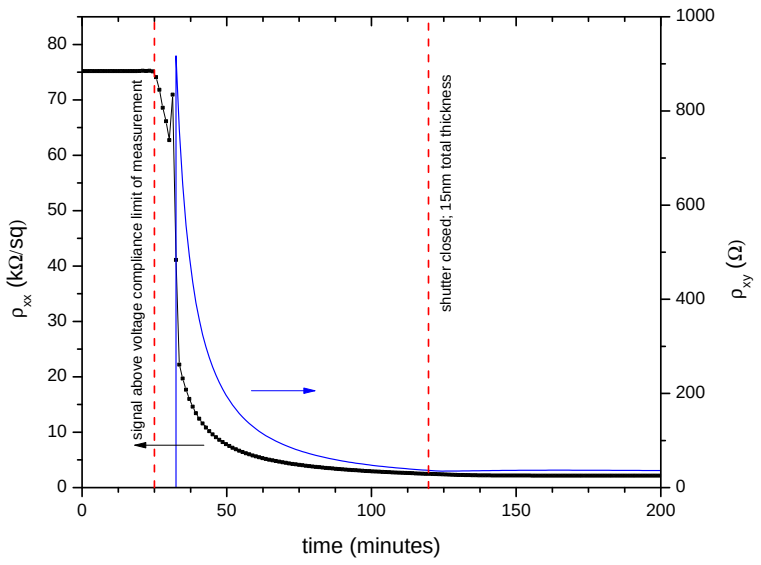

Figure 2.5: Two-dimensional longitudinal (left axis) and Hall resistivity (right axis) measured during film growth. 10μA DC excitation current. The red dashed line at 25 minutes denotes when the sample becomes measurably conductive; before that time, the compliance limit of the measuring instrument (>200kΩ) is exceeded. The second red line at 120 minutes indicates when the shutter was closed and substrate heating shut off; 15 nm of film was grown.

2.4 Demonstration of Technique

Figure 2.5 shows the zero-field, two-dimensional longitudinal (ρ_{xx}) and Hall (transverse) resistivity (ρ_{xy}) measured as a function of time during film growth. In this instance, the substrate temperature was a constant 115°C throughout the growth, from 0-120 minutes in figures 2.5 and 2.6. At 120 minutes, the shutter was closed and substrate heating shut off; the sample passively cooled to room temperature in three hours. The deposition rates at the substrate surface were nominally 0.1 nm/min for bismuth and 1.8 nm/min for selenium leading to a total film thickness of 12-15 nm. The substrate temperature for film growth is higher than the evaporation point of selenium in vacuum (∼100°C) but lower than that of bismuth (∼600°C). Bismuth deposition is then the controlling rate of film growth, done in an over-flux of selenium (typically 10-15 times the bismuth rate). Growing more quickly reduces total exposure to impurities/contaminants but compresses the available time for measurements, which are limited by the sweep rate of the magnet. Growing at a rate of minutes per nanometer allows for more data points to be collected during the initial formation stages of the film. The vertical red dotted line at 25 minutes is a guide to the eye to demarcate the time when the film has reliably measurable conductivity: before that time, the resistance between the electrodes is beyond the voltage compliance limit of the measuring instrument (>200kΩ). ρ_{xy} is measured while periodically sweeping the magnetic field: the slowly changing background due to parasitic ρ_{xx} contribution is subtracted out before fitting the $\rho_{xy}(B)$ data to extract the Hall carrier density.

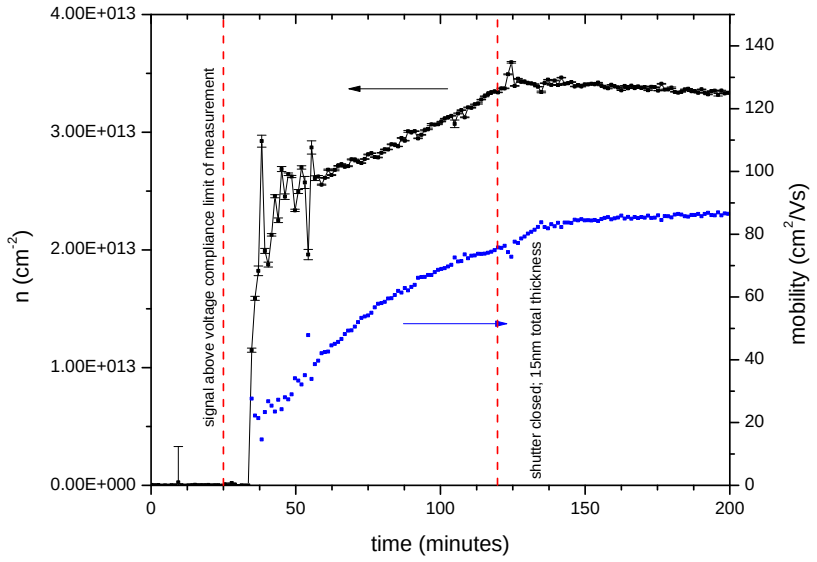

Figure 2.6: Two dimensional (electron) Hall carrier density (left axis) and mobility (right axis) plotted as a function of film growth time. Red dashed lines the same as in figure 2.5.

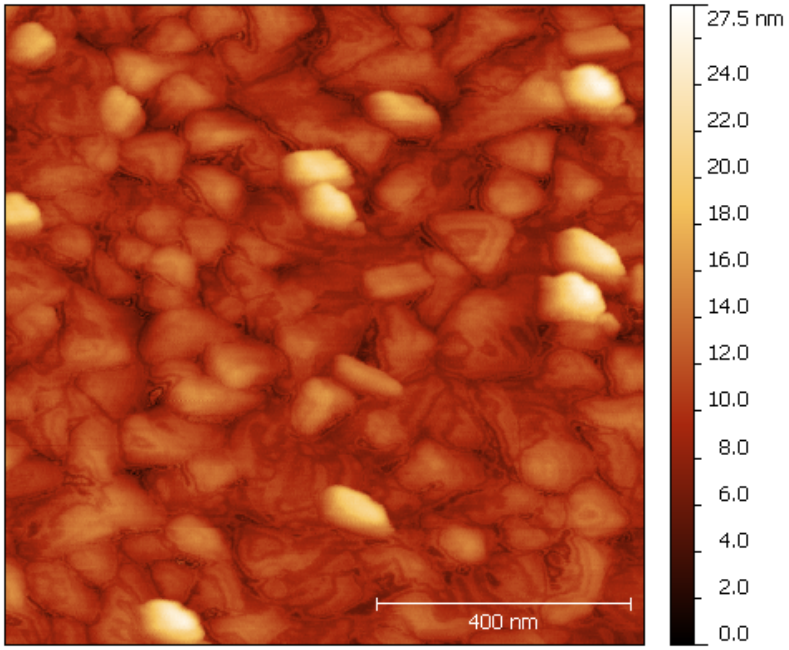

Figure 2.7: ex situ contact mode AFM image of Bi_2Se_3 film on STO(111)

μ and n are plotted as a function of film growth time in figure 2.6. For the growth in figures 2.5 and 2.6 we observe that the carrier density has a sharp increase to $\sim$2x10^{13} cm^{-2} at the onset of conduction, followed by a slower increase of 1.2 x10^{12} cm^{-2} for each nanometer of additional film growth. Figure 2.7 is an *ex situ* ambient AFM image of one of the first Bi_2Se_3 films successfully grown on strontium titanate STO(111) by this technique. These initial observations are studied in greater detail in chapter 3.

2.5 Source-Swapping for Capping Layer Deposition

The geometry of this system allows for vacuum to be maintained in the sample space while the source effusion cell is swapped. This aspect is exploited in chapter 6: after the growth and characterization of a 15 nm Bi_2Se_3 sample, the effusion cell was changed to deposit a molecular MoO_3 overlayer. In light of the problems in this material system with respect to ambient exposure, this methodology provided an unambiguous determination of the efficacy of MoO_3 as a p-doping capping layer.

Chapter 3: Results I: *In Situ* Bi_2Se_3 Growth Dynamics Study

3.1 Outline of Parameter Space Studied

Using the apparatus previously described in chapter **??**, we studied the real time evolution of carrier density and mobility as a function of film thickness during growth for different substrate temperature profiles. The dependence of transport parameters on film thickness have been reported previously for Bi_2Se_3 on Si(111) and Al_2O_3 substrates [72] [115], however in those studies multiple films of difference thicknesses were measured *ex situ*, and only one growth parameter regimen could be explored.

Samples were grown using a two-temperature method [116] [117] [118] where the first two nanometers are grown at 110°C and the remainder of the film grown at different temperatures between 200-230°C. I also measured a single-temperature growth at 210°C for comparison. The initial carrier density at the onset of conduction is approximately 1.5 x 10^{13} cm^{-2}, and the carrier density growth with thickness corresponds to a bulk dopant density of ∼5 x 10^{11} cm^{-2} per quintuple-layer unit (QL), with both values roughly independent of growth conditions. This suggests that a significant component of the observed doping in Bi_2Se_3 films is associated with the formation of the Bi_2Se_3-substrate and Bi_2Se_3-vacuum interfaces, even without expo-

sure to ambient. In contrast, the mobility depends strongly on growth conditions, with maximum mobility achieved for a two-step growth at 110°C and 210°C, consistent with the optimum growth temperatures observed by reflection high energy electron diffraction (RHEED) aided growth studies. [119] [116] [117] [72] [115] [118] The results are strongly suggestive that the charge carrier mobility in our Bi_2Se_3 films (and likely in the films prepared in other laboratories) is not limited by ionized impurities (dopants) but rather by structural uniformity. Atomic force microscopy (AFM) confirms a strong correlation between mobility and structural coherence of the films.

3.2 *In Situ* Transport for Different Growth Parameters

Two-stage growth is carried out at a temperature of 110°C for the first two nanometers of film deposition, before increasing the substrate temperature to a series of 'hot' temperatures between 200 and 230°C. Two additional samples were grown: in one instance the substrate temperature was maintained at 110°C, for the other, the substrate temperature was 210°C the entire time, forgoing the initial low temperature growth. Longitudinal and Hall resistivities are monitored continuously during film growth by periodic application of a magnetic field swept continuously between ± 1100 Gauss. The thickness of each sample is calculated from the bismuth rate using the empirically determined tooling factor for the growth chamber.

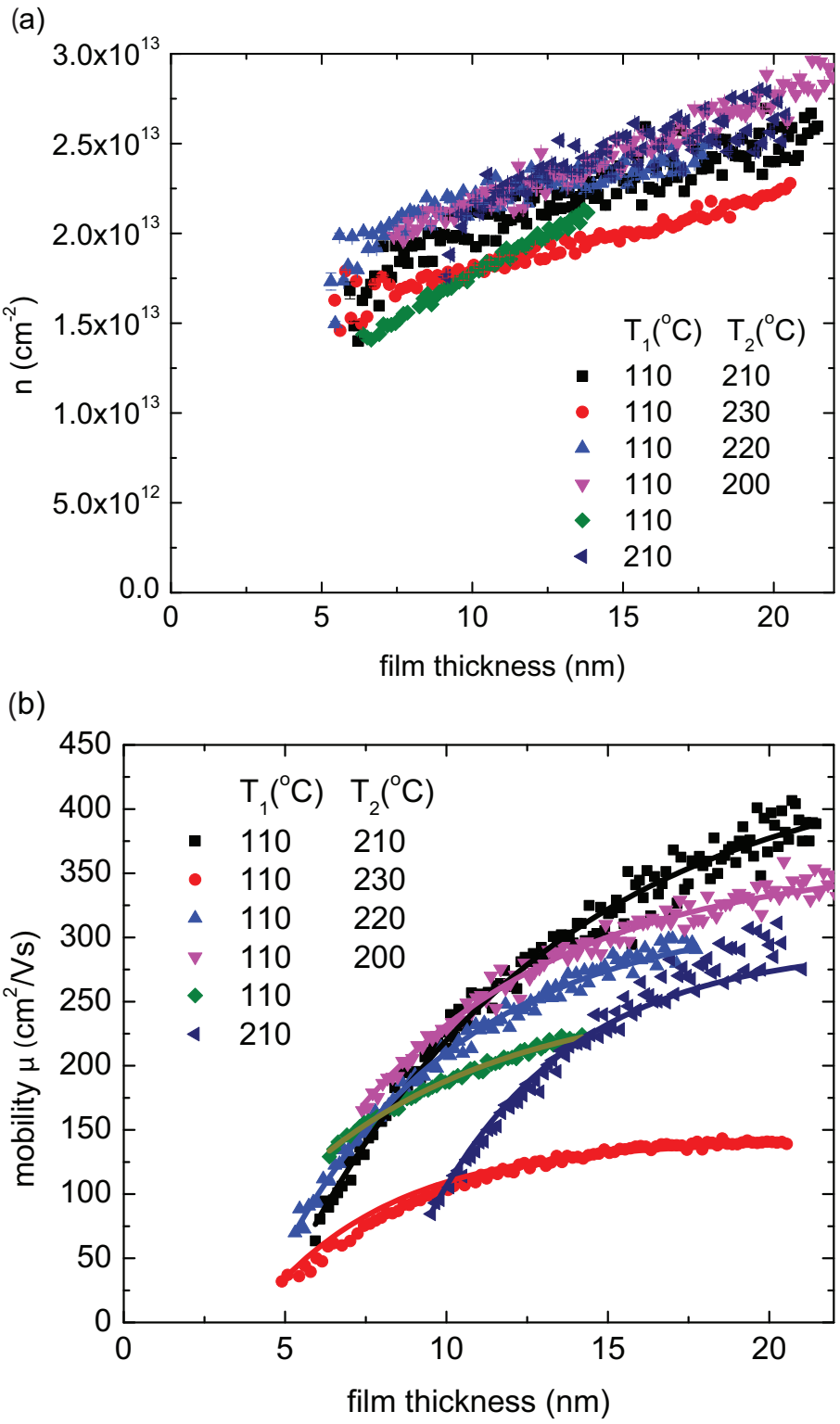

Figure 3.1: (a) Hall carrier density n and (b) mobility μ versus Bi_2Se_3 film thickness for various growth temperature profiles as shown in legend: T_1 is the substrate temperature for the first 2nm of film deposited, T_2 is the temperature for the remainder of the growth. In the cases where there is no T_2 the T_1 temperature was maintained for the whole growth.

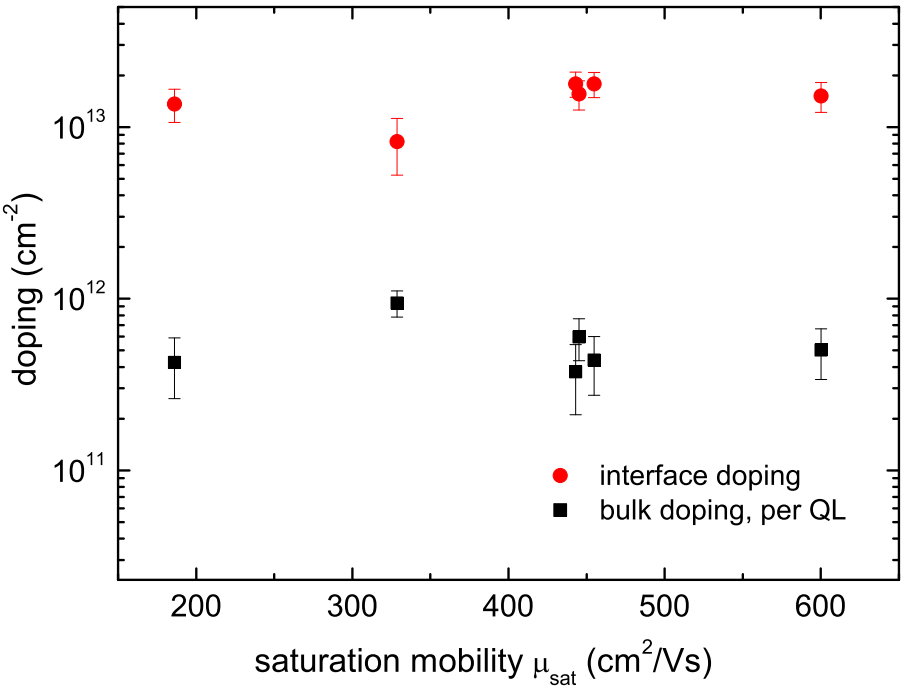

Figure 3.2: Bulk dopant concentration per QL $\mathrm{d}n/\mathrm{d}t$ (black squares) and interfacial dopant concentration n_0 (red circles) extracted from the slope and intercept, respectively, of linear fits to $n(t)$ in fig. 3.1(a), plotted against saturation mobilities extracted from the data in fig. 3.1(b).

3.3 Interfacial vs. Bulk Doping

Figure 3.1(a) shows $n(t)$ and fig. 3.1(b) shows $\mu(t)$ for the different growth temperature profiles (there are large fluctuations in the magnitude of ρ_{xy} with time during the initial growth when $\rho_{xx} > 100$ kΩ, typically for the first 5 nm of film growth, where presumably the film is highly non-uniform in thickness or possibly discontinuous. The reported data is for when $\rho_{xx} < 100$ kΩ, and when ρ_{xy} values become stable and presumably the film is continuous and uniform). As shown in fig. 3.1(a), $n(t)$ is very similar for all growth temperature profiles studied. $n(t)$ is roughly linear, with a positive intercept at zero thickness. The results are in contrast to *ex situ* measurements of Bi_2Se_3 on Si(111) where $n \sim \sqrt{t}$ [115], and Bi_2Se_3 on Al_2O_3 where n is independent of thickness [72]. A linear fit to the data in fig. 3.1(a) can be interpreted by ascribing the intercept $n_0 \approx$ (1-2) x 10^{13} cm^{-2} as an interface dopant concentration which is present as soon as the film is formed, and the slope $dn/dt \approx 5$ x 10^{11} cm^{-2} per QL as a bulk (3D) dopant concentration which scales linearly with thickness indicating a constant rate of new dopants added as new film is deposited. It is not possible to deduce from these measurements whether the interface dopants correspond to the Bi_2Se_3-vacuum or substrate-Bi_2Se_3 interfaces, or whether the interface dopants are at the interface itself or incorporated in the first few nanometers of film which may be more disordered. Regardless of the source, the *in situ* nature of our measurements shows that the doping is inherent to the initial formation of the interfaces and not due to reaction with ambient.

3.4 Dependence of Mobility on Growth Parameters

Figure 3.1(b) shows the thickness dependence of the mobility $\mu(t)$. In contrast to $n(t)$, $\mu(t)$ shows appreciable changes with different growth temperature profiles. Note that the reported mobilities are measured at the respective growth temperatures, explaining their somewhat lower magnitude relative to mobilities reported elsewhere in the literature. Solid lines in fig. 3.1(b) are fits to the measurement using the phenomenological relation [115]:

$$\mu(t) = \frac{\mu_{sat}}{1 + \frac{\lambda^*}{t - t_0}} \tag{3.1}$$

where μ_{sat} is interpreted as the saturation mobility in the thick-film limit. The uncertainties expressed in figures 3.2 and 3.4 for the interfacial and bulk doping, saturation mobility values respectively were estimated from the variance of a series of samples grown with nominally identical (110-210 °C) growth conditions. μ_{sat} varies by a factor of 3 for different growth conditions, while the carrier concentration at a given thickness varies by less than a factor of 1.5. This result is surprising, since the carrier concentration is expected to reflect the concentration of ionized impurities (dopants), which have been suspected as a major source of disorder (i.e. lowered mobility) in Bi_2Se_3 [12]. These results show that mobility varies strongly with growth conditions though dopant concentrations are nearly constant.

3.5 Structural Coherence Studied by Atomic Force Microscopy

To further explore the correlation between dopant concentration and mobility, fig. 3.2 shows the bulk dopant concentration $\mathrm{d}n/\mathrm{d}t$ and interfacial dopant concentration n_0 extracted from fig. 3.1(a) as a function of the μ_{sat} extracted from fig. 3.1(b). There is no clear correlation of either $\mathrm{d}n/\mathrm{d}t$ or n_0 with μ_{sat}, in fact the highest and lowest-mobility films have very similar concentrations of both bulk and interfacial dopants. This suggests that dopants are not the dominant disorder in these films, and that the changes in mobility with growth conditions are controlled by another variable.

Atomic force microscopy (AFM) was used to further investigate the crystal quality of the films as another possible variable controlling mobility. Figure 3.3 shows representative *ex situ* AFM images taken using a Bruker Dimension Icon using the contact mode of imaging. A clear difference is immediately evident between the two images: the sample grown at 110-210°C for which mobility is optimal shows evidence of van der Waals epitaxial growth, with atomically flat terraces of width ∼50 nm, while the sample grown at 110-230°C with lower mobility shows greater roughness and evidence of some crystallites with c-axes oriented non-parallel to the film normal. The differences are quantified using the height-height correlation function $H(x)$ (function of point-to-point distance x) computed for each sample and fit to:

$$f(x) = 2\sigma^2(1 - e^{-(x/T)^2}) \tag{3.2}$$

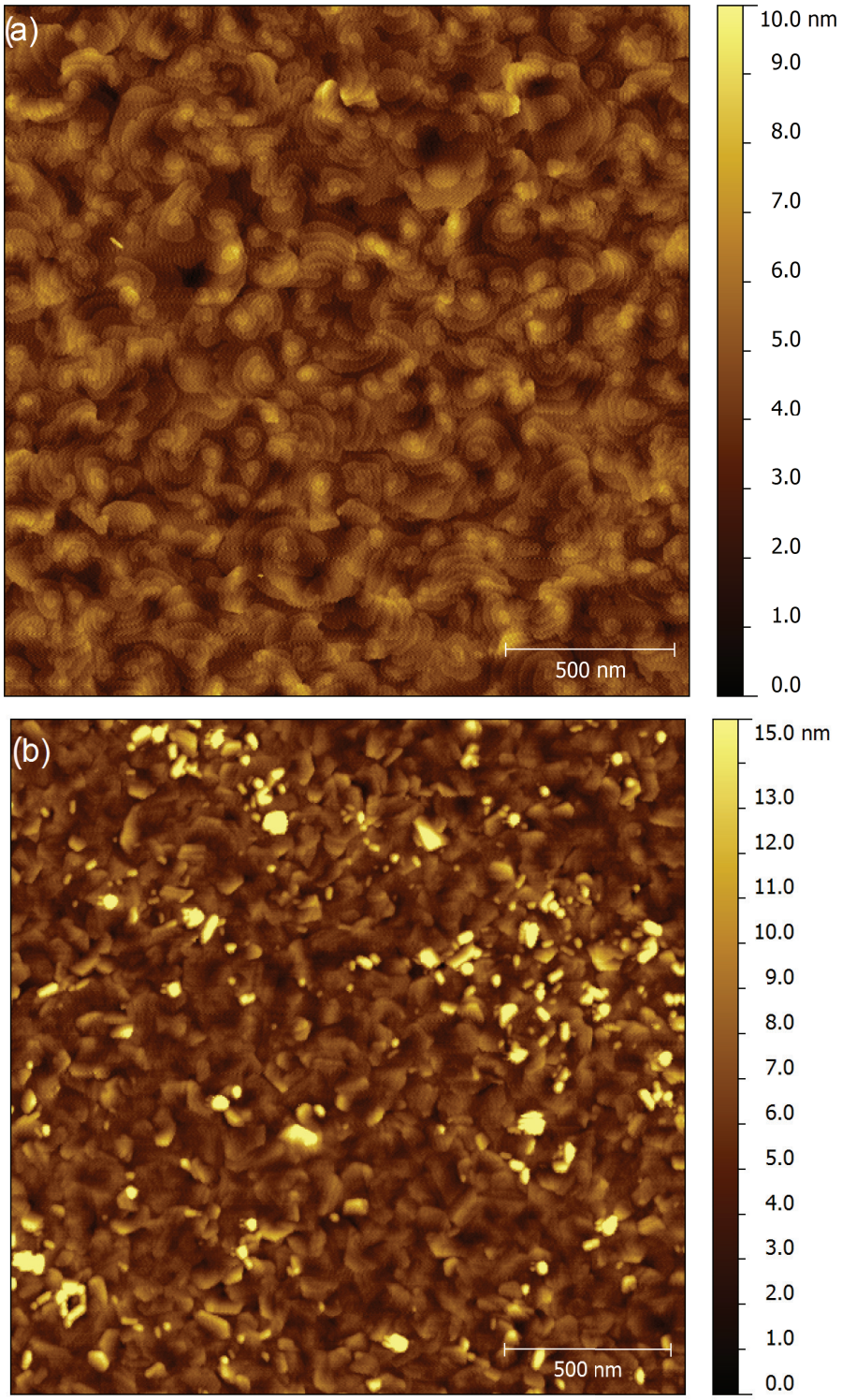

Figure 3.3: *ex situ* 2μm x 2μm atomic force microscope images of the a) 110-210°C and b) 110-230°C films.

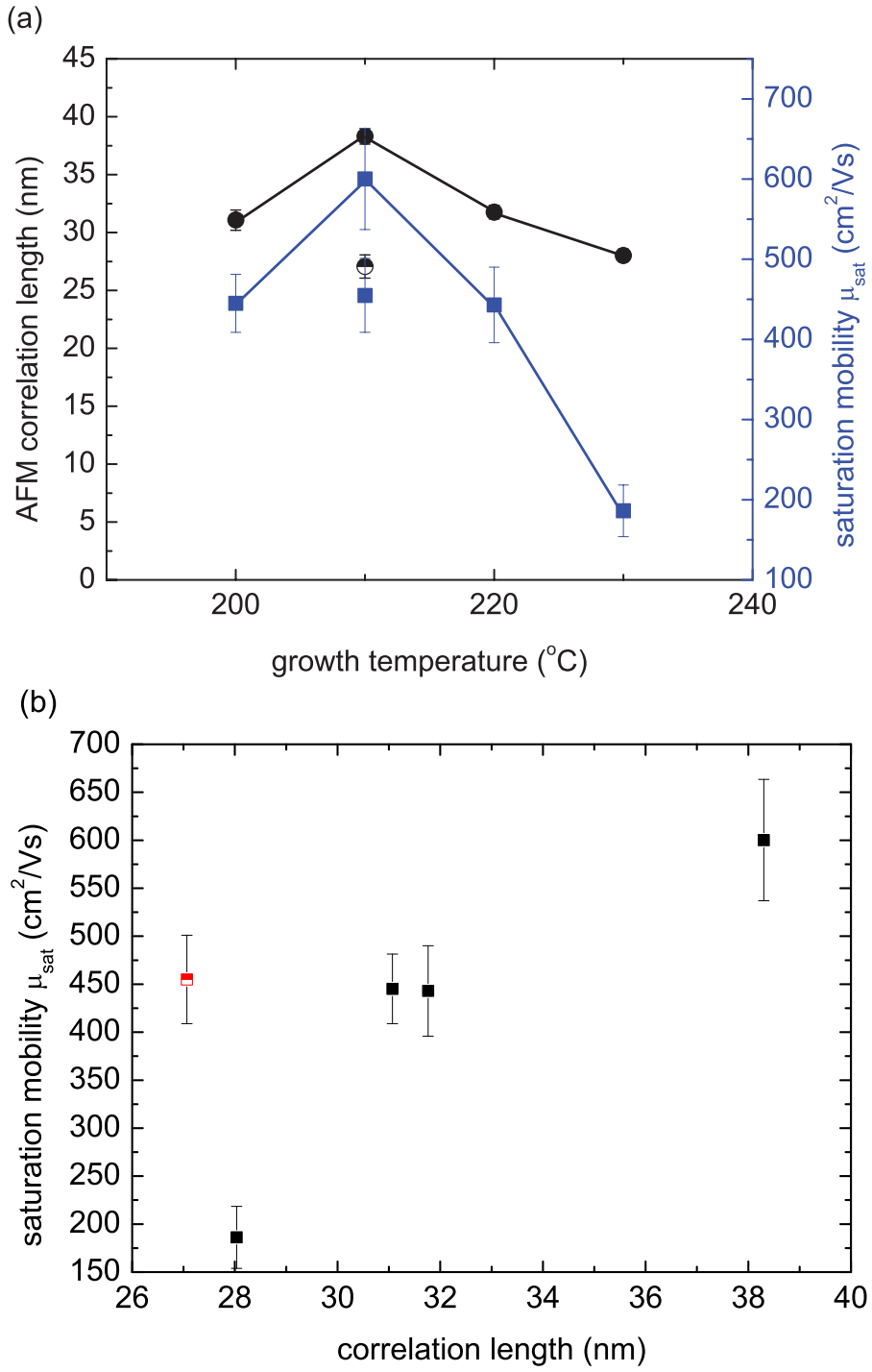

Figure 3.4: (a) Saturation mobilities μ_{sat} (squares) extracted from the data in fig. 3.1(b) and correlation lengths T (circles) from AFM images are plotted as a function of the highest temperature during growth for each respective sample. The half filled points at 210°C correspond to the single-step growth sample. (b) Saturation mobility plotted against AFM correlation length for each sample; black points are two-step growths, the red half-filled point is the single-step growth at 210°C.

In this case σ is the standard deviation in height, and T is the surface correlation length. T is interpreted as a measure of the structural coherence of the film. For an epitaxial film, T would be proportional to the mean terrace width.

Figure 3.4(a) shows the AFM correlation length and saturation mobility μ_{sat} as a function of the hot growth temperature for each sample, showing a peak both in the mobility and the correlation length for the two-step growth at 110-210°C. The single-step 210°C growth values are also shown, measurably lower than the two-step growth terminating at the same temperature. To further explore this relationship, in fig. 3.4(b) μ_{sat} is plotted against the AFM correlation length T. A high degree of correlation between μ_{sat} and T is observed for the two-step samples, strongly indicating that the structural coherence of the film is the driving variable behind mobility variation with growth conditions.

3.6 Summary of Findings

Bismuth selenide films grown according to widely employed methodology within the literature are substantially n-doped as grown in vacuum, before any exposure to atmosphere. Significant interface ($\sim$(1-2) x 10^{13} cm^{-2}) and bulk ($\sim$ 5 x 10^{11} cm^{-2} per QL) dopant concentrations are observed, nearly independent of growth conditions. Differences in mobility with respect to growth temperature appear to be driven by changes in film morphology, as quantified by *ex situ* AFM analysis, rather than variations in dopant concentrations. The implication is that work to date on Bi_2Se_3 film preparation has optimized the structural coherence of the films,

but significant gains remain to be made in reducing both bulk and interfacial dopant concentrations.

Chapter 4: Methods II: Photoemission Spectroscopy (XPS)

4.1 Introduction

This chapter presents the relevant background theory and methods for synchrotron based X-ray photoelectron spectroscopy (XPS), in the context of the results presented in chapter 5, namely, manipulating the doping of single crystal bismuth selenide with an overlayer of molecular MoO_3. These experiments were done at the soft x-ray end station of the Australian Synchrotron.

The photoelectric effect is the phenomena of electrons being emitted from conducting materials when they are exposed to photons. In an XPS experiment, samples are exposed to a light source, and the energy of the photoemitted electrons are measured (see figure 4.1). These data are analyzed to infer information about the nature of the electronic structure of the sample. In this specific instance XPS was used to measure Bi, Se, and Mo core level binding energies (see figure 4.3 as a representative example of core level spectra) and secondary electron cutoff, quantities that provide information about the doping and work function of Bi_2Se_3 and how these changed when MoO_3 was introduced, as well as the fraction of MoO_3 molecules that participated in the doping process.

The subsequent sections of this chapter detail a little bit more about the

photoemission process, how these samples are prepared and the data is collected, as well as how the measured spectroscopy peaks are analyzed.

4.2 Modeling the Photoemission Process

Figure 4.1 illustrates the basic quantities measured in an XPS experiment. The synchrotron provides high intensity incident photons at a selectable energy hν. The detector measures the kinetic energy of the photoemitted electrons. This zeroth order picture of XPS is too simple for meaningful use of the technique for the present work.

Figure 4.2 illustrates an incrementally more sophisticated way of thinking about this process. Photoexcitation is described using Fermi's Golden Rule; treating the penetration through the surface into the free electron state separately makes the initial problem more analytically tractable.

From a user standpoint this is a series of solved problems. Both the incident light and the detector (SPECS) have been extensively characterized. The synchrotron has selectable incident photon energy (in contrast to a fixed excitation from the lab based source). When changes to the photon energy are made it is standard practice to confirm the selected photon energy on a gold standard by measuring the Au $4f_{7/2}$ core level peak (84.00 eV), or Fermi edge (figure 4.3). This allows the binding energy scale of all Bi_2Se_3 related spectra to be referenced to the Fermi energy (E_F) by having the Au reference in electrical contact with the sample. For most photon energies the Au 4f peak is the preferred reference standard. At

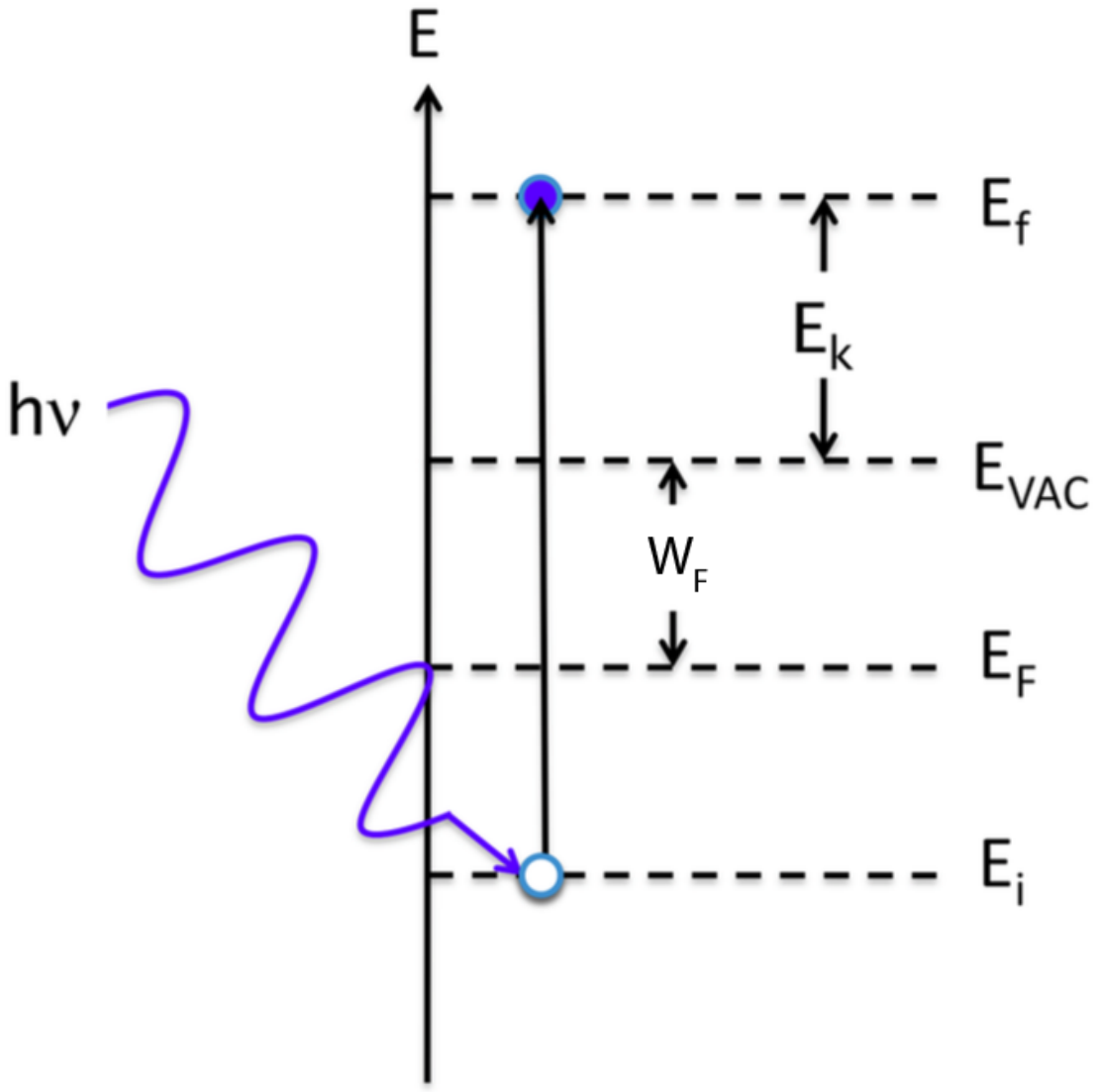

Figure 4.1: Illustration of the photoemission process for an incident photon of energy hν. The photoemitted electron has initial energy E_i and final energy E_f. The work function $W_F = E_{vac} - E_F$ is the energy difference between the vacuum energy (E_{vac}) and Fermi level (E_F). The kinetic energy of the electron $E_k = E_f - E_{vac}$ is the difference between the final energy (E_f) and vacuum energy. Taken from ref. [15].

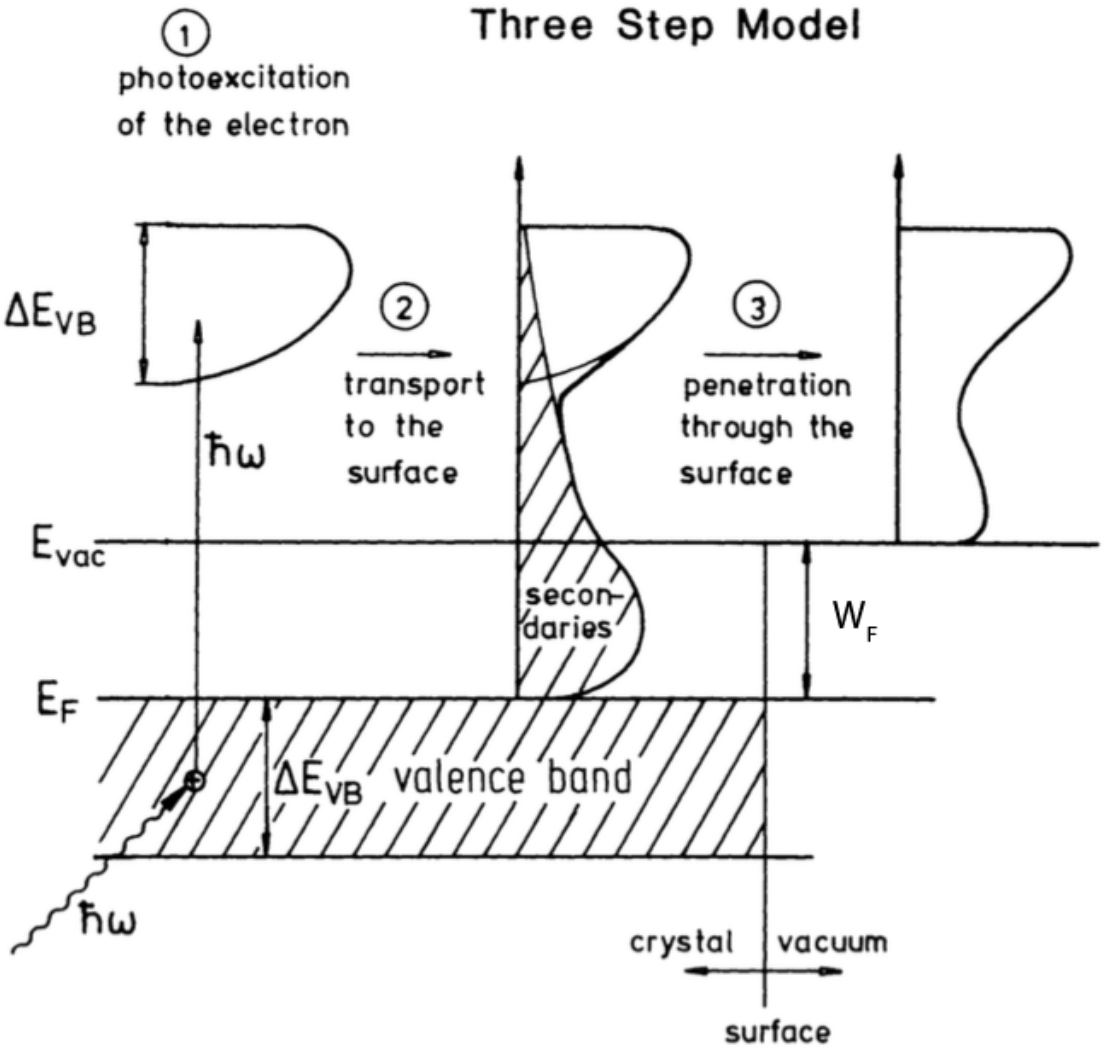

Figure 4.2: The "Three Step Model" divides the photoemission process into three separate analytical problems. From left to right, in chronological order: 1) photo excitation of the electron, 2) transport of the electron to the surface, and 3) penetration through the surface into free vacuum. Reproduced from ref. [16].

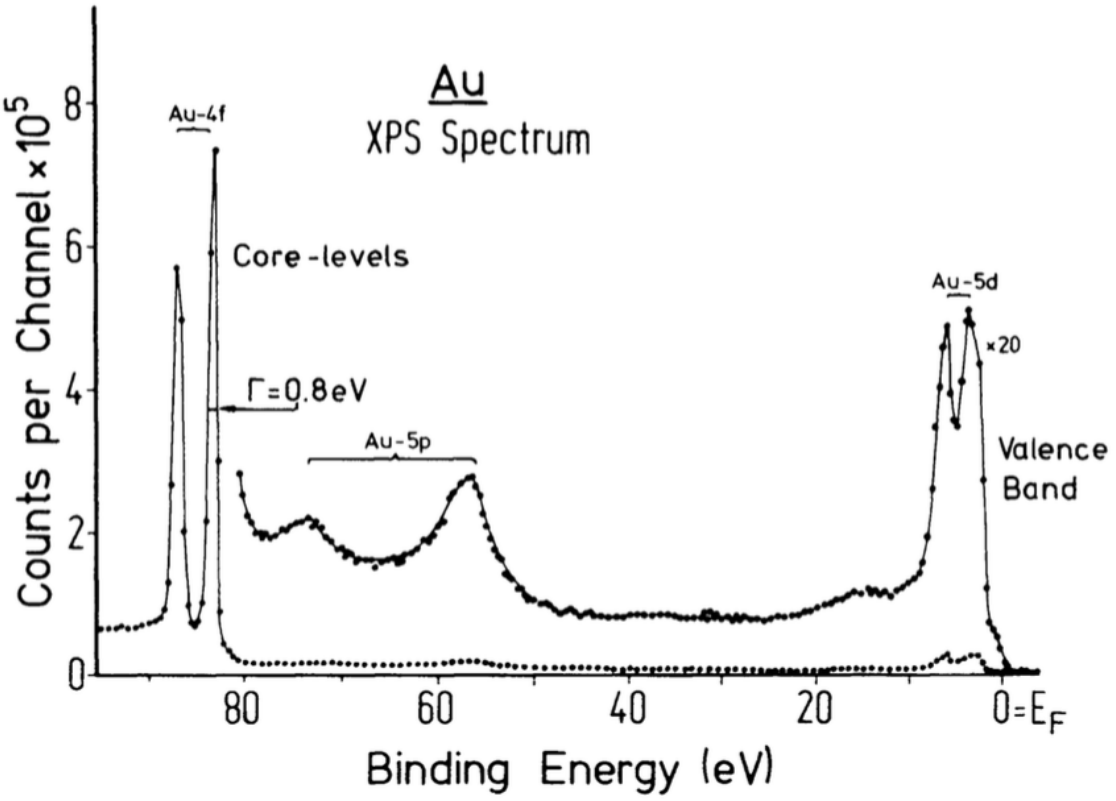

Figure 4.3: Example of XPS spectroscopy for polycrystalline Au sample. Reproduced from ref. [16].

lower photon energies, for example the 100 eV used for some of these experiments, the 4f binding energy of 84 eV is too close to be safely measured by the detector. The threshold would be below the secondary electron cutoff, meaning the detector would be flooded with excess electron signal, damaging the detector and distorting the desired measurement. Instead, the Fermi edge (through zero binding energy) is measured and fit to the Fermi-Dirac distribution. Prior to performing experiments a detailed beam damage study was performed to ensure the molecules were stable under prolonged beam exposure.

4.3 Surface Sensitivity, Auger Peaks, Photon Energy Selection

This study was performed at the synchrotron (as opposed to using a lab based instrument) because surface sensitivity was an important factor in performing a surface doping study. The continuously tunable photon energy available at the synchrotron enables surface sensitivity to be optimized as follows.

The typical energy range for XPS work is between 10 and 2000 eV (the soft X-ray bandwidth). Figure 4.4 makes clear why this technique is acutely surface sensitive: this so-called "universal curve" of mean free path for electrons can be as little as a few angstroms for the right excitation energy. A consequence of this surface sensitivity is the need for ultrahigh vacuum (UHV) conditions during measurement; the presence of surface contamination will further disrupt the unscattered primary photocurrent, reducing or even destroying the signal of interest. The UHV environment was an advantage in this instance because of the ambient instability of

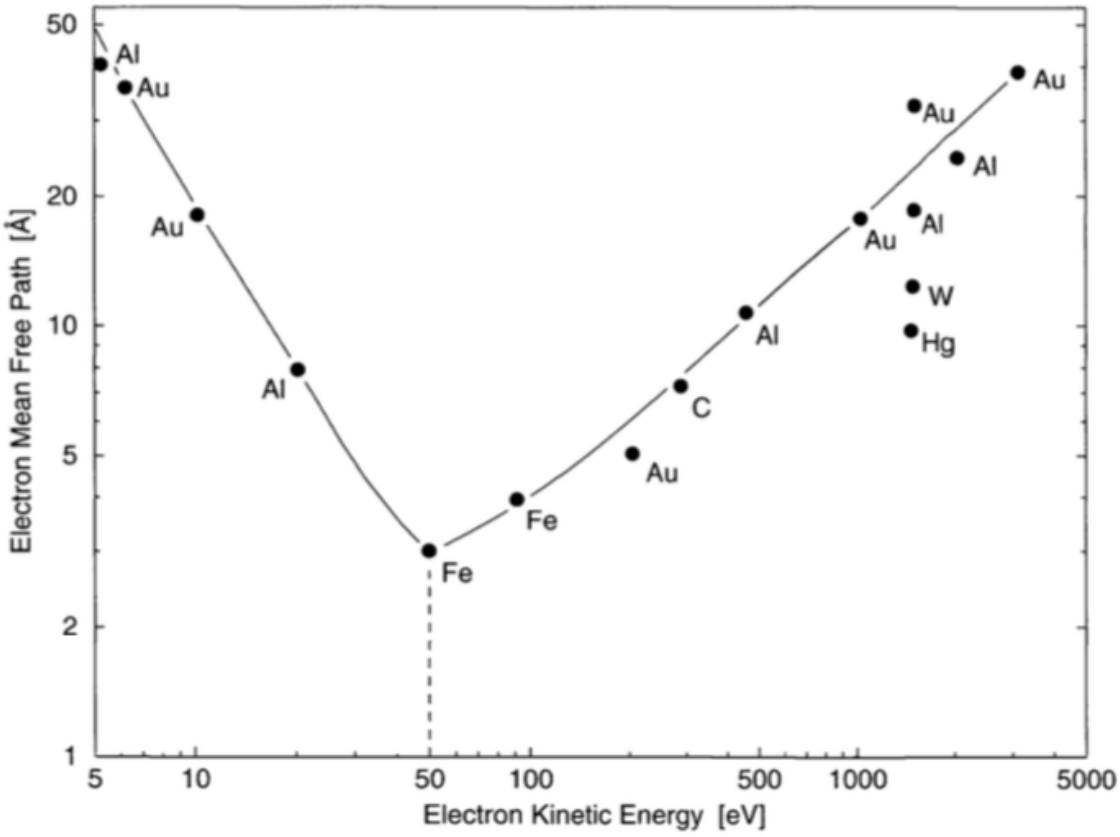

Figure 4.4: Electron mean free path plotted against photon energy for different metals. Taken from reference [16].

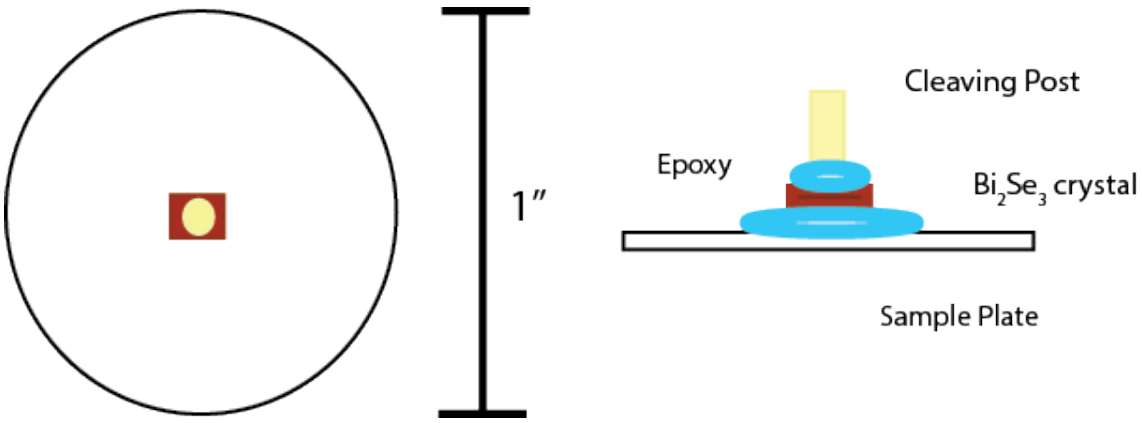

Figure 4.5: Schematic of single crystal Bi_2Se_3 flake (red) mounted on a synchrotron sample plate for *in situ* cleaving. Care is taken to avoid epoxy for the post covering the edges of the sample flake to ensure a clean cleave requiring relatively little force.

bismuth selenide.

Different elements have different characteristic core level spectra, one of the central utilities of this technique. In addition to the primary photoemission process, there are various inter- and intrastate transitions, in this context referred to as Auger electron spectra. These Auger peaks can coincide with core levels of interest. This complicates the selection of photon energy beyond merely the penetration depth/ surface sensitivity: energies have to be selected so Auger peaks don't collide with the core levels of interest.

4.4 Single Crystal Sample Preparation

These Bi_2Se_3 crystals were obtained from Paul Syers and Prof. Johnpierre Paglione of the University of Maryland. They were low-doped (carrier density $\sim 10^{17}$ cm^{-3}) with bulk resistivity exceeding 2 mΩ cm^{-1} at 300 K were grown by melting high purity bismuth (6N) and selenium (5N) in sealed quartz ampoules [120].

Figure 4.5 illustrates how ∼3x3 mm flakes were mounted to metal plate sample holders using a vacuum compatible conductive epoxy (Epotek H22). The flakes are mounted according to the preferred cleaving plane of the bismuth selenide to ensure a flat, high quality surface for the subsequent measurements. 4mm diameter stainless steel rod was cut into ∼1 cm lengths and filed at the end for a uniform bonding surface.

The samples were then introduced into the ultra-high vacuum photoemission endstation where they were subsequently cleaved *in situ* by using a mechanical manipulator to knock off the stainless steel cleaving post and kept at pressures $<10^{-9}$ mbar during experiments and deposition.

F4-TCNQ and MoO_3 (Sigma Aldrich) were deposited onto the cleaved samples at room temperature using commercial effusion cells (MBE Komponenten GmbH) operating at 135 °C and 525 °C respectively, with a quartz crystal microbalance (QCM) used as a guide for the deposition rate.

4.5 Secondary Electron Cutoff to Determine Work Function

In figure 4.2 one can think of the work function W_F as a threshold that eliminates a large portion of the secondary electrons produced in the photo excitation process in moving from step two to three. This secondary electron cutoff threshold can be measured to determine the work function using the following relation:

$$E_{kin} = \hbar\omega - W_{F_{Bi_2Se_3}} - |E_B|$$

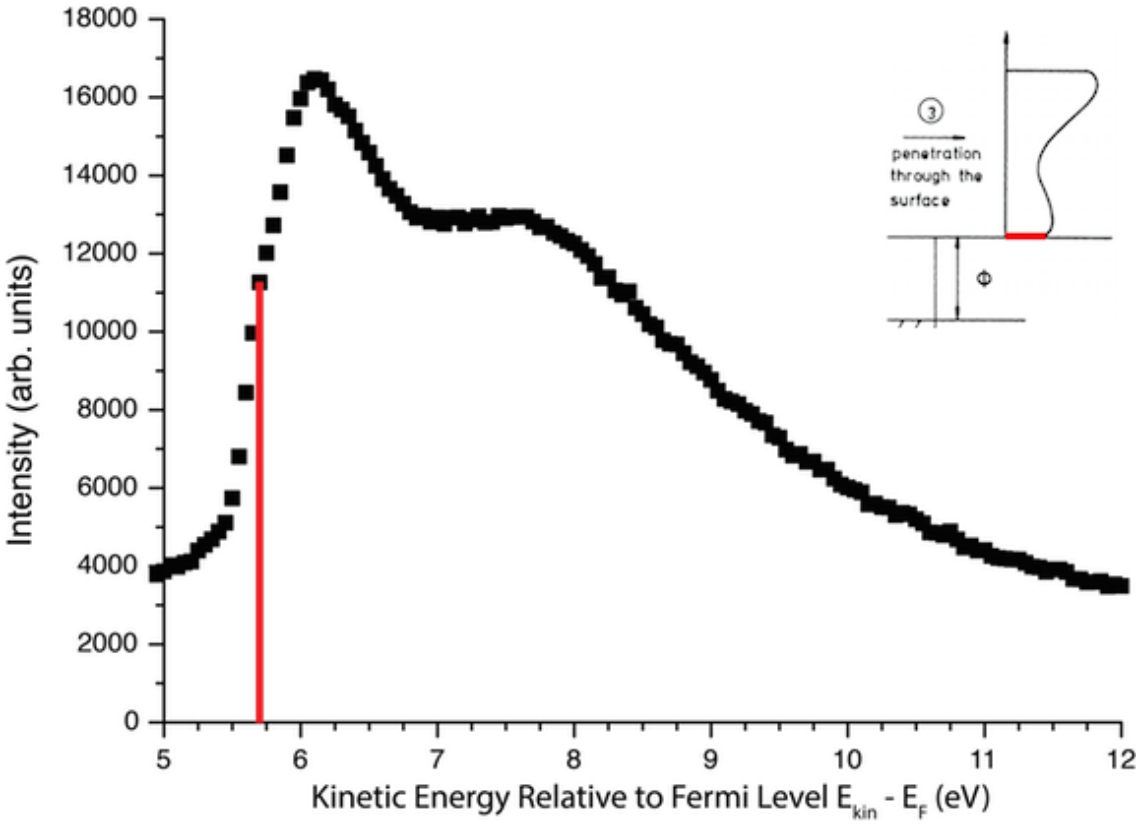

Figure 4.6: Example of secondary electron cutoff spectra taken on cleaved single crystal Bi_2Se_3 (100 eV photon energy). Compare for example to figure 1.7 in reference [16]. Inset is "step 3" from figure 4.2 with the red line highlighting the work function energy being measured.

$\hbar\omega$ is the (known) photon energy and the binding energy E_B is zero at the Fermi level. The cutoff is named for the threshold at which the kinetic energy E_{kin} is zero (at the vacuum energy E_{vac}), therefore determining the work function W_F. This is demonstrated in figure 4.6, a secondary electron cutoff measurement performed on Bi_2Se_3. The cutoff energy is indicated in red.

The SPECS detector at the soft X-ray end station where this work was done has an intrinsic work function of 4.5 eV. Because this is quite close in energy to the bismuth selenide work function, the sample is biased (-8V in this case) to experimentally deconvolve the two quantities. The experimental uncertainty is ± 0.03 eV for this measurement.

4.6 Peak Fitting

XPS data is peak fit in many different ways depending on the phenomenological circumstances. In this case, the core level positions and total areal intensity give information about doping changes and thickness of the molecular overlayer. The secondary electron emission contributions are a background that is removed before fitting the remaining peaks to a convolution of Lorentzian and Gaussian functions called a Voigt function [121]. Practically speaking this can be accomplished by a handful of different commercially available analysis programs. The data in this work was analyzed with Origin peak fitting routines.

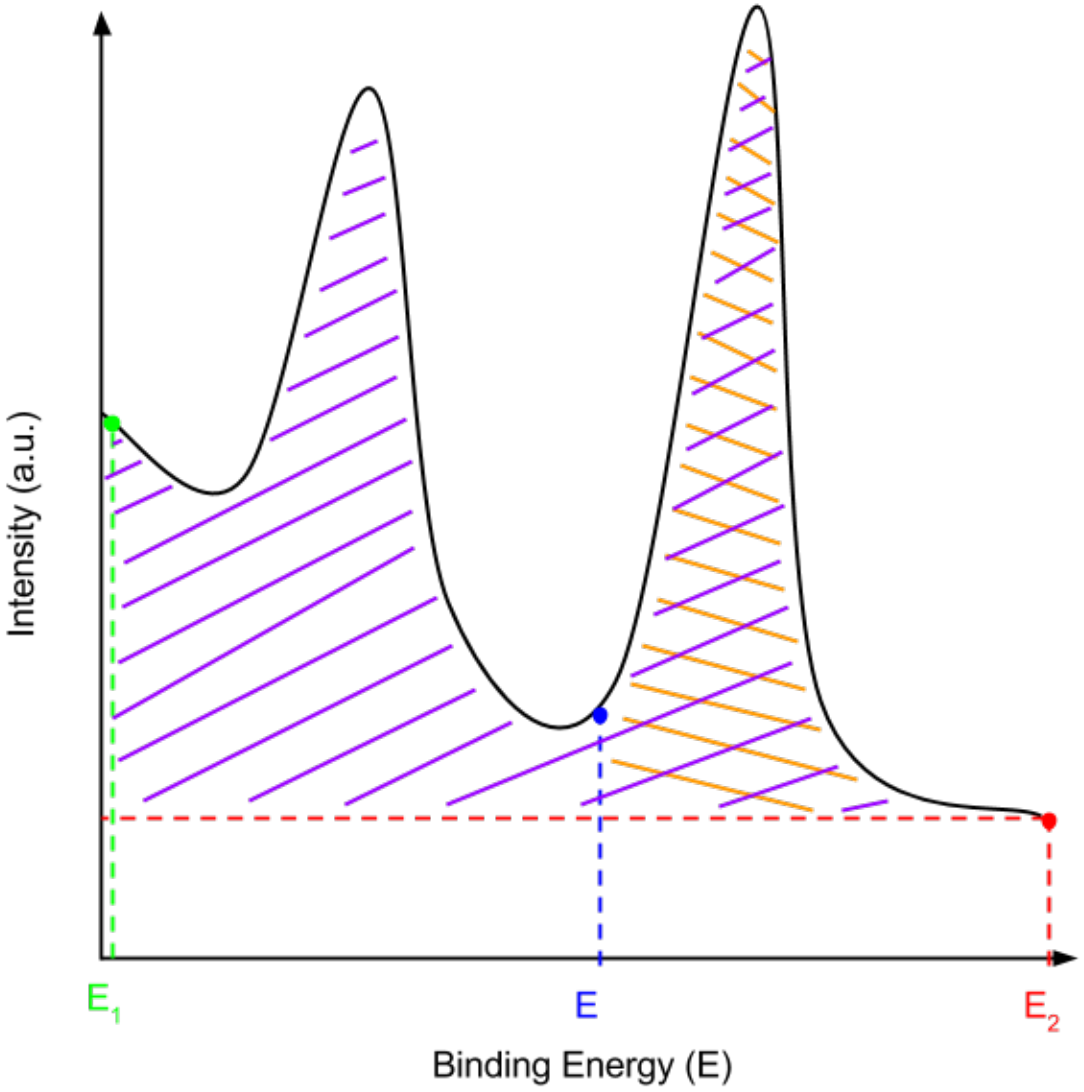

Figure 4.7: Arbitrary spectra illustrating the Shirley background subtraction algorithm. $E_{1,2}$ are endpoints of the binding energy range considered. The orange and purple cross hatching are the integrals in equation 4.1.

4.6.1 Shirley Background Subtraction

For quantitative analysis, peak intensities have to be normalized from scan to scan. The "Shirley" method is one of a variety of ways to subtract the background that was employed for this work [122]. This is an iterative method that accounts for background noise in the detector as well as inelastic scattering processes (see for example Hufner [16] for more information beyond Shirley's original work).

The intensity I at each point in the energy range of interest is iteratively rescaled using the following formula:

$$I'(E) = I(E) - [I(E_1) - I(E_2)]\frac{\int_E^{E_2} dE'[I(E') - I(E_2)]}{\int_{E_1}^{E_2} dE'[I(E') - I(E_2)]} \tag{4.1}$$

The numerator and denominator integral expressions are illustrated with orange and purple cross hatching respectively in figure 4.7. Repeating this procedure across different scans makes relative intensity changes in peak height and area quantitatively comparable.

4.6.2 Quantifying Peaks

Peak fitting is a field of study in itself. In this instance, we expect that the core-hole lifetime gives a Lorentzian (eqn. 4.3) distribution of energies, while thermal and instrumental signal broadening are described by a Gaussian (eqn. 4.2) distribution. Other inelastic processes may give more complex peak shapes such as the Doniach-Sunjic lineshape [123].

These two peak shape contributions can be convoluted in either product or sum fashion [121]. For this work, the product convolution referred to as a Voigt function was used. The Gaussian line shape is given by:

$$G(x) = G_0 + \frac{A}{\sqrt{\frac{\pi}{2}} W_G} e^{-\frac{2}{W_G^2}(x-x_c)^2} \tag{4.2}$$

The Lorentzian line shape by:

$$L(x) = L_0 + \frac{2A}{\pi} \frac{W_L}{4(x-x_c)^2 + W_L^2} \tag{4.3}$$

and the Voigt function is the convolution of $G(x)$ and $L(x)$:

$$\begin{aligned} V(x; W_G, W_L) &= \int_{-\infty}^{\infty} dt G(t) L(x-t) \\ &= V_0 + A \frac{2\ln 2}{\pi^{3/2}} \frac{W_L}{W_G^2} \int_{-\infty}^{\infty} dt \frac{e^{-t^2}}{\left(\sqrt{\ln 2}\frac{W_L}{W_G}\right)^2 + \left(\sqrt{4\ln 2}\frac{x-x_c}{W_G} - t\right)^2} \end{aligned} \tag{4.4}$$

In equations 4.2, 4.3, 4.4 A is the amplitude, x_c is the peak centre, W_G and W_L are the Gaussian and Lorentzian peak widths, respectively, and G_0, L_0, V_0 are offset terms.

4.7 Specific Application of Peak Fitting to Chapter 5 Results

For this experiment, the Gaussian and Lorentzian peak widths (W_G, W_L) were initially fixed using values from the literature [124], leaving the amplitude and peak

centre as the fit parameters for the fitting of the pristine cleaved Bi_2Se_3 samples. For subsequent fits, the Lorentzian contribution remained fixed with the literature value while the Gaussian width was used as an additional fitting parameter. Amplitude change corresponds to the core level signal attenuation as a result of depositing an thicker and thicker overlayer of MoO_3, while shifts in energy of the peak centre correspond to changes in the doping. These changes in Fermi level, E_F, in response to surface transfer doping were monitored using both the Bi 5d and Se 3d core level components of Bi_2Se_3 at a photon energy of 100 eV to ensure high surface sensitivity with an overall measurement uncertainty of ± 0.02 eV, where the error is defined as one standard deviation.

The shift to lower binding energy was the same for both core levels as expected so only the Bi 5d core level results are presented and discussed. In order to determine E_F - E_D from the Bi $5d_{5/2}$ binding energy we first measured the angle-integrated valence band of a freshly cleaved sample to determine that the Dirac point energy lies 0.27 ± 0.05 eV below the Fermi level (i.e. E_F - $E_D = 0.27 \pm 0.05$ eV), consistent with ARPES results on lightly doped Bi_2Se_3 crystals, where the Fermi level lies just above the bulk conduction band minimum [14].

From this we determine a fixed separation of the Dirac point to the Bi $5d_{5/2}$ orbital of 24.60 ± 0.05 eV. The $\pm$ 0.05 eV error represents a systematic uncertainty in determining E_F - E_D.

Chapter 5: Results II: Doping of Bi_2Se_3 with Molecular Electron Acceptor MoO_3

5.1 Overview of Results

Using the XPS techniques outlined in chapter 4, lightly-doped Bi_2Se_3 crystals (surface Fermi energy relative to Dirac point E_F - $E_D \sim 270$ meV) were cleaved in vacuum and exposed to the molecular dopant MoO_3. This was done in three aspects: 1) coverage-dependent photoemission spectroscopy of Bi core levels that tracked the Fermi energy shift, 2) Mo core level spectroscopy measured the fraction of charged MoO_3 molecules, and 3) low-energy cutoff spectroscopy to measure the work function. We find that MoO_3 is an efficient doping acceptor, saturating at E_F - $E_D = 100$ meV, well within the topological regime. An induced interface dipole of 0.74 eV was measured, corresponding to $\sim 10^{13}$ cm^{-2} electrons transferred from the Bi_2Se_3. A doping model based on Fermi-Dirac statistics was implemented to accurately describe the doping behavior including saturation.

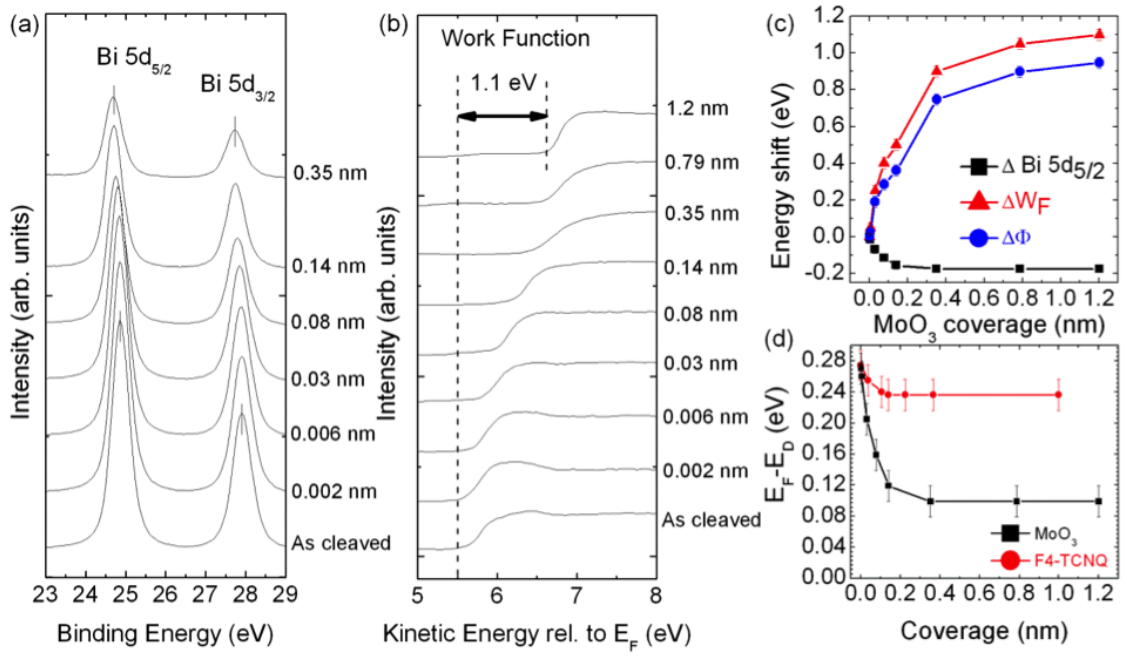

Figure 5.1: Molecular coverage dependent Fermi energy and surface dipole. (a) Bismuth 5d core level spectra taken at hν = 100 eV at selected MoO_3 coverages. (b) Secondary electron cut-off as a function MoO_3 coverage. (c) Energy level shifts for the Bi $5d_{5/2}$ core level (black squares), work function (red triangles), and interface dipole (blue circles) as a function of MoO_3 coverage. [Note: Error bars smaller than plot symbol]. (d) E_F - E_D plotted as a function of MoO_3 coverage (black squares) and F4-TCNQ coverage (red circles).

5.2 XPS Results

5.2.1 Bi Core Level and Low-energy Cutoff Spectroscopy

In Figure 5.1 the response of the Fermi level shift and work function of *in situ* cleaved Bi_2Se_3 samples to deposition of MoO_3 are measured using high-resolution surface sensitive photoemission spectroscopy. Figure 5.1(a) plots the evolution of the bismuth 5d core level (at photon energy hν = 100 eV) with increasing MoO_3 coverage. Both the Bi $5d_{5/2}$ and Bi $5d_{3/2}$ peak positions shift to lower binding energy (i.e. the Fermi energy moves towards the Dirac point) with increasing coverage, and

reach saturated positions at a coverage of 0.34 nm. In Fig. 5.1(b) the secondary electron cut-off is plotted as a function of MoO_3 coverage. The work function of the freshly cleaved sample is 5.40 ± 0.03 eV, and increases by up to 1.1 eV as the MoO_3 coverage increases. The saturated value of 6.5 eV at a coverage of 0.8 nm is in reasonable agreement with values reported for solid MoO_3 [125], indicating that the low energy cut-off spectra are no longer probing the Bi_2Se_3-MoO_3 interface but only the MoO_3 overlayer. In Fig. 5.1(c) the change in Bi $5d_{5/2}$ peak position (black squares), the change in work function, ΔW_F (red triangles) and the interface dipole, $\Delta\phi$ (blue circles), that forms as a result of the surface transfer doping process are plotted as a function of MoO_3 coverage. The binding energy of the Bi core level decreases by 0.18 ± 0.02 eV, consistent with the removal of electrons from the Bi_2Se_3. The work function increases by 1.1 eV, indicating the formation of a positive surface dipole that arises due to charge transfer across the Bi_2Se_3-MoO_3 interface. The interface dipole is given by $\Delta\phi = \Delta W_F - \Delta(E_F - E_D)$ where E_F - E_D is the position of the Fermi level relative to the Dirac point at each coverage plotted in Fig. 5.1(d) (black squares). However, the work function value used to determine the interface dipole is only valid at low coverages (i.e. up until charge transfer saturation), above which it starts to represent the measurement of the molecular overlayer, thus resulting in incorrect determination of the doping induced dipole. At 0.34 nm of MoO_3, an interface dipole of 0.73 ± 0.02 eV has built up at the Bi_2Se_3-MoO_3 interface. In Fig. 5.1(d) we plot E_F - E_D for both MoO_3 (black squares) and F4-TCNQ (red circles) as a function of respective molecular coverage. In both cases, the as-cleaved samples have E_F - E_D = 0.27 ± 0.05 eV (i.e. the Fermi level

lies 0.27 eV above the Dirac point energy). However, the response of E_F - E_D to the two molecules is very different, with only a shift of 40 meV observed for F4-TCNQ, consistent with previous reports of doping to near the conduction band edge [105]. In contrast, for increasing MoO_3 coverage the Fermi level moves towards the Dirac point, reaching a saturated value of 100 $\pm$ 20 meV above the Dirac point, placing the Fermi level well within the gap and in the topological regime. This difference could arise due to the significantly larger electron affinity of MoO_3 compared to F4-TCNQ, with values as high as 6.7 eV reported for thick MoO_3 films [125] compared to 5.24 eV for F4-TCNQ [126]. The measured work function of as-cleaved Bi_2Se_3 is 5.4 eV, placing the lowest unoccupied molecular orbital (LUMO) of F4-TCNQ above the Fermi level of the Bi_2Se_3 when the vacuum levels are aligned, meaning only a small amount of charge transfer is possible. In contrast, the larger electron affinity of MoO_3 places the LUMO position well below the Fermi level, allowing for charge transfer to take place.

5.2.2 Mo Core Level Spectroscopy

Measurement of the Mo core levels revealed three distinct features (figure 5.2(a)): peaks at binding energies of 231.5 eV and 234.7 eV which correspond to the Mo $3d_{5/2}$ and Mo $3d_{3/2}$ states respectively. A third small peak at 228.3 eV is assigned to the 2s core level of sulphur, which we associated with these Bi_2Se_3 samples. This was confirmed by taking angular-dependent spectra on as-cleaved samples and observing no change in intensity of the S 2s peak; its presence in the

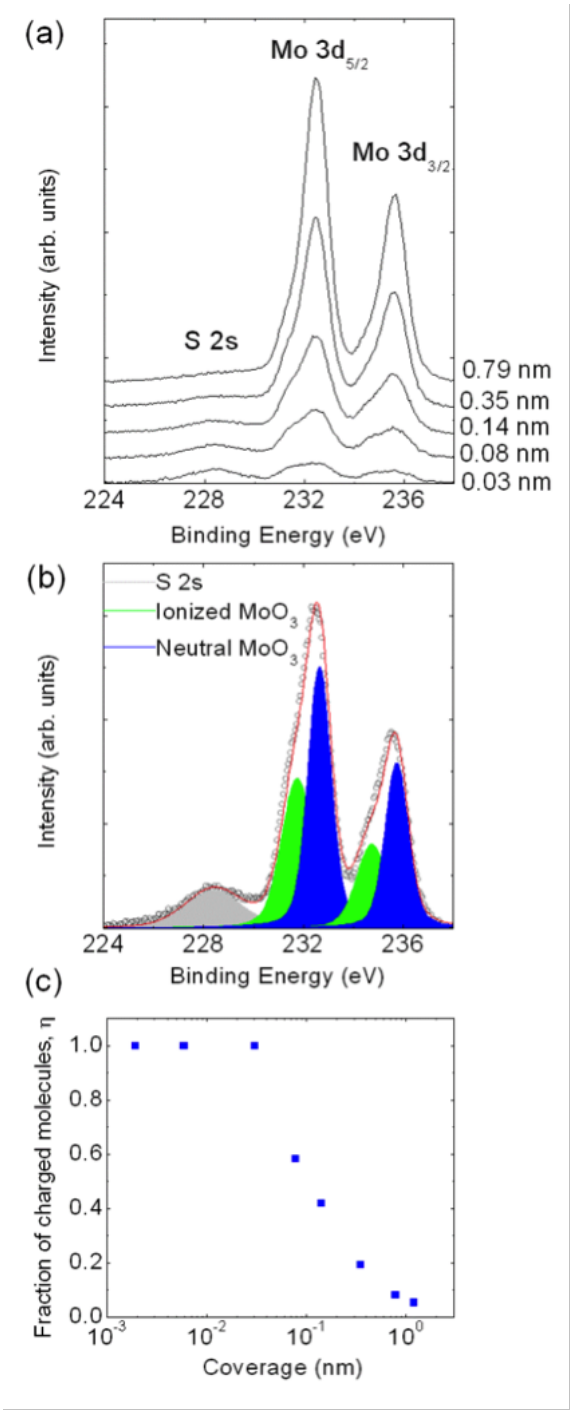

Figure 5.2: Measurement of the fraction of charged molecules using molybdenum core level spectroscopy. (a) Mo 3d core level spectra at selected MoO_3 coverages. (b) MoO_3 core level spectra at a coverage of 0.14 nm with peak fits illustrating the two clear MoO_3 charge states. (c) Relative fraction of ionized MoO_3 as a function of coverage of the two components: doping (N_{A^-}) and non-doping (N_A) that make up the Mo 3d core level of MoO_3 on Bi_2Se_3.

data has no bearing on the doping effects being studied. Remarkably, both the Mo $3d_{5/2}$ and Mo $3d_{3/2}$ features consist of two distinct peaks clearly separated in binding energy by ∼0.8 eV and whose relative intensities (branching ratios) are the same for both $3d_{5/2}$ and $3d_{3/2}$. In Fig. 5.2(b) the Mo 3d spectrum taken at 0.14 nm coverage is plotted showing the two distinct components necessary to represent the data. This observation is strong evidence for two chemically different states of the MoO_3 molecules on the surface of Bi_2Se_3 assigned to be neutral (N_A) and ionized (N_{A^-}) MoO_3 acceptors. These two species did not form during evaporation of MoO_3 (e.g. stoichiometric MoO_3 and MoO_3 with oxygen vacancies) because the relative intensities of the two components are strongly dependent on coverage. A similar effect was observed for surface transfer doping hydrogen-terminated diamond with the fluoro-fullerene $C_{60}F_{48}$ where the two species correspond to neutral and singly-ionized $C_{60}F_{48}$ [127]. The Mo 3d lines at lower binding energy are ionized molecules as the extra charge within a MoO_3 molecule is expected to lower all binding energies due to additional Coulomb repulsion.

The observation of neutral and charged MoO_3 in the photoemission spectra directly probes the fractional concentration $\eta = N_{A^-} / (N_A + N_{A^-})$ of ionized molecules, where N_{A^-} and N_A are the relative peak areas at each coverage. Figure 5.2(c) shows η plotted as a function of coverage. As expected, at low coverage η is near unity as all the molecules are ionized. At higher coverages η drops as the induced surface dipole retards further charge transfer; there is a transition between mainly ionized MoO_3 below 0.14 nm to an increasing contribution of non-doping neutral MoO_3 for higher coverages until the charge transfer process ceases at 0.35

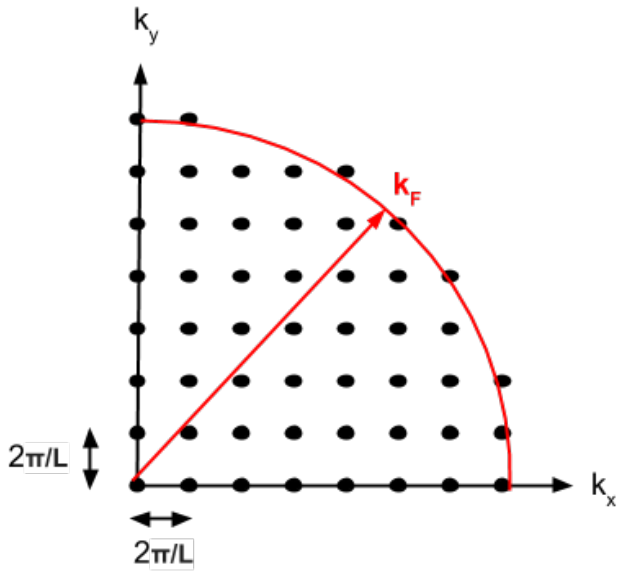

Figure 5.3: How to "count" the two dimensional density of states: 2d momentum space, with black dots representing allowed states, and the Fermi momentum arc indicated in red.

nm. Beyond this coverage additional MoO_3 remain neutral on the Bi_2Se_3 surface.

5.2.3 Charge Transfer Model

5.2.3.1 Bi_2Se_3 Surface States

The simplest way to consider the band structure of Bi_2Se_3 is to approximate it as an exactly linear dispersion relation near the Dirac point:

$$E_F - E_D = \hbar\nu_F|\mathbf{k}|$$

In two dimensions, enumerating the density of states is fairly straightforward. Figure 5.3 shows a representation of momentum space, where the allowed states are represented by black dots at $2\pi/L$ intervals, the condition for the wave function period to match the lattice spacing. The phase space area per state is then $4\pi^2/L^2$.

The total phase space area for a given k_F is πk_F^2. Divide the one by the other to count the number of states:

$$N = \frac{\pi k_F^2}{4\pi^2/L^2} = \frac{k_F^2 L^2}{4\pi} \rightarrow n \equiv \frac{N}{L^2} = \frac{k_F^2}{4\pi}$$

In the case of the topological insulator surface state, the spin-momentum locking means that the momentum states are not doubly spin degenerate, so this expression is not multiplied by two. Substitute this into the original assumption of a linear dispersion to arrive at the desired relationship between carrier density and energy:

$$E_F - E_D = \hbar\nu_F|\mathbf{k}| = \hbar\nu_F\sqrt{4\pi n} \rightarrow n(E_F) = \frac{|E_F - E_D|^2}{\pi(2\hbar\nu_F)^2} \tag{5.1}$$

5.2.3.2 MoO_3 Doping

The Fermi energy shift (figure 5.1d) can be understood by interpreting the concentration of ionized MoO_3 (figure 5.2(c)) in terms of the amount of charge removed form the surface. Figure 5.4(a) is a plot of the charged MoO_3 molecules, N_{A^-}, expressed in monolayers (1 ML corresponds to a thickness of 0.65 nm [128]) as a function of E_F - E_D. If only one electron is transferred per MoO_3 molecule, consistent with the observation of only two types of Mo core-level spectra, and the expectation that strong intermolecular Coulomb interaction should yield positive effective correlation energy, N_{A^-} can be equated with the change in charge density in the Bi_2Se_3. In this case, equation 5.1 can be modified to describe the behavior of N_{A^-} with respect to E_F - E_D:

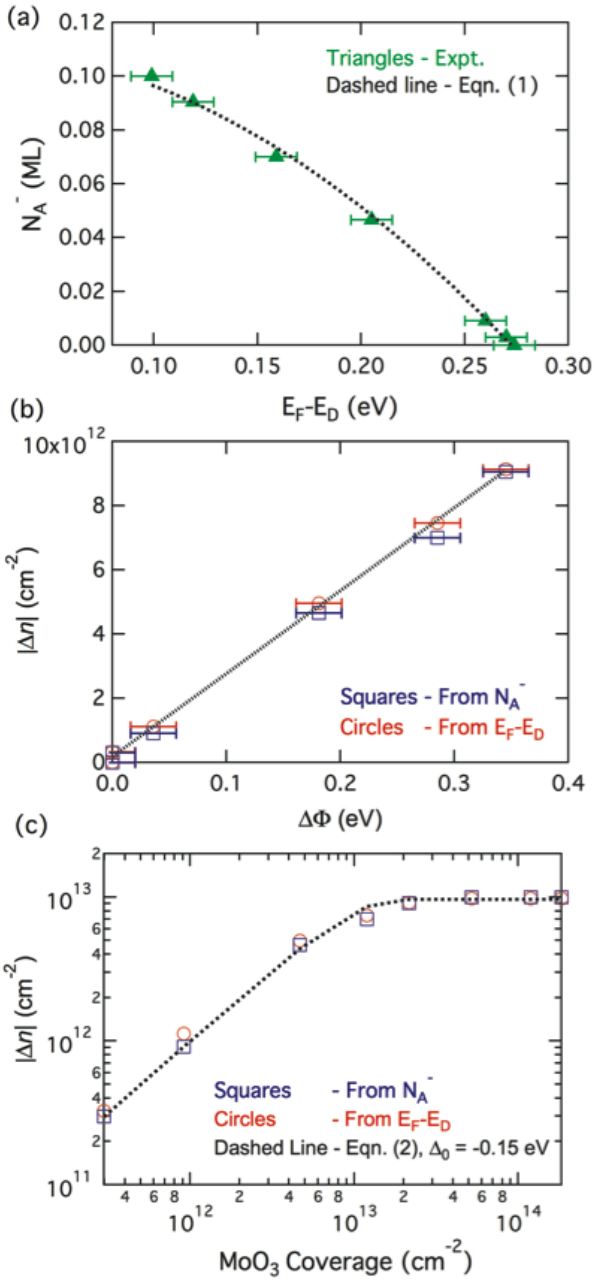

Figure 5.4: Comparison of experimental data and charge transfer model. (a) Number of charged MoO_3 molecules (monolayer, ML) plotted as a function of E_F - E_D. The black dashed line is a fit of the data using Eqn. (5.2). (b) Change in carrier density $|\Delta n|$ as a function of interface dipole $\Delta\phi$. (c) Change in carrier density $|\Delta n|$ as a function of MoO3 coverage. In (b-c) blue squares show $|\Delta n|$ determined from the number of charged MoO_3 molecules (data in Fig. 5.2c) and red circles show $|\Delta n|$ calculated from E_F - E_D assuming a linear surface state dispersion. In (c) the black dashed line corresponds to the change in density calculated using Eqn. (5.3) with initial activation energy of -0.15 eV.

$$N_{A^-} \equiv \frac{n_0}{\rho} - \frac{|E_F - E_D|^2}{\pi\rho(2\hbar\nu_F)^2} \tag{5.2}$$

ρ is the areal density of a monolayer of MoO_3 molecules per cm^2, n_0 is the initial sheet carrier density of the Bi_2Se_3 surface, and ν_F is the Fermi velocity of electrons in Bi_2Se_3. [Note that there should be some additional contribution from bulk states in Eqn. (5.2), however the low Fermi energy of the as-cleaved crystals E_F - E_D = 270 meV is near the bulk band edge, so the surface state is expected to dominate the density of states.] The dashed line in Fig. 5.4a is a fit to Eqn. (5.2). The fit does not determine both ρ and ν_F; however assuming a Fermi velocity of ν_F = 3.5 x 10^5 ms^{-1} [14] [129] yields a value for the areal density for 1 ML of, ρ = 1.0 x 10^{14} MoO_3 molecules cm^{-2}, in reasonable agreement with what would be expected from close packing arguments based on the size of the MoO_3 molecule. Using ν_F = 3.5x10^5 ms^{-1} and the linear band dispersion, the as-cleaved samples (E_F - E_D = 0.270 eV), have an initial surface carrier density of n_0 = 1.13 x 10^{13} cm^{-2}. Upon saturation of the charge transfer process at a coverage of 0.34 nm of MoO_3 and E_F - E_D = 0.10 eV the density is now n = 1.47 x 10^{12} cm^{-2}. Thus, almost $\sim 10^{13}$ cm^{-2} of electrons can be removed from the Bi_2Se_3 when MoO_3 is deposited onto the surface.

The change in charge density $|\Delta n| = |n - n_0|$ can be compared to the interface dipole, $\Delta\phi$. Δn is extracted from the experimentally measured E_F - E_D values (red circles) using ν_F = 3.5 x 10^5 ms^{-1}, as well as independently from the number of ionized MoO_3 molecules (blue squares) using the areal density, ρ = 1.0 x 10^{14} obtained from figure 5.4a. The result is shown in figure 5.4b. In both cases, Δn

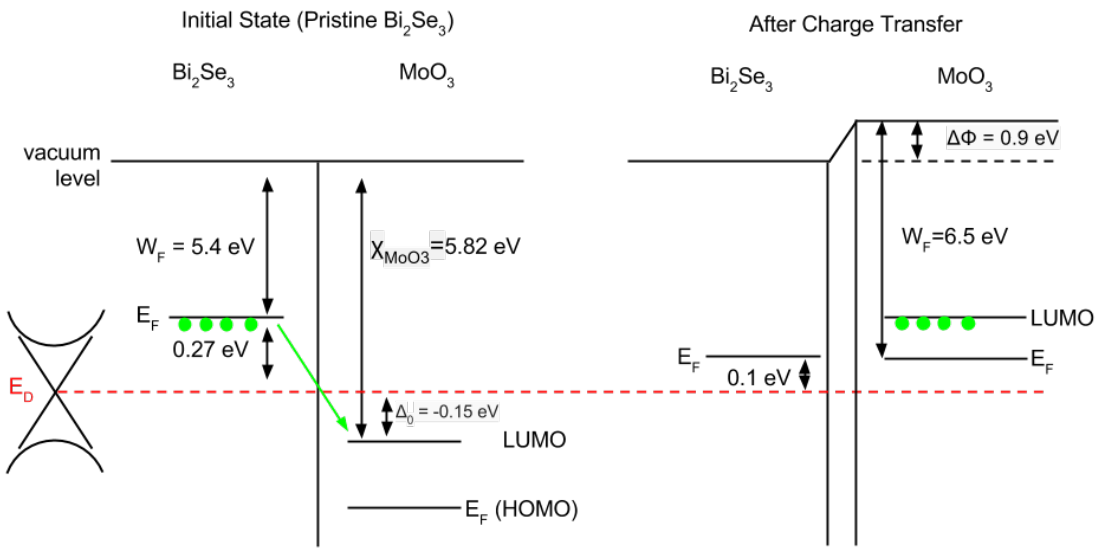

Figure 5.5: Diagram showing the various energies associated with the charge transfer (electrons, in green) from Bi_2Se_3 to MoO_3 molecules. The red dotted line is the Dirac point energy of the Bi_2Se_3. The left diagram shows the Fermi energy (E_F) relative to the Dirac point as well as the work function (W_F) of pristine Bi_2Se_3 prior to doping. The electron affinity of neutral MoO_3, χ_{MoO_3} is also labelled. When charge transfer occurs (right diagram), an interface dipole $\Delta\phi$ (labelled on right) develops.

is proportional to $\Delta\phi$, with the same constant of proportionality, consistent with a simple electrostatic (capacitive) interpretation where $\Delta n = (\frac{1}{e}\mathrm{C})\ \Delta\phi$ and C is the capacitance per area associated with the separation of charge across a charge-free region at the Bi_2Se_3-MoO_3 interface. A linear fit of the data yields C = 4.16 μF cm^{-2} for the interface capacitance.

The charge transfer mechanism between the Bi_2Se_3 and the MoO_3 overlayer can be thought of as a "band bending" of the MoO_3 lowest unoccupied molecular orbital (LUMO) and interface dipole formation to match the Fermi levels at the interface (figure 5.5). "Band bending" is strictly speaking a misnomer in this context because the MoO_3 layer is being considered as discrete molecules as opposed to some kind of crystalline structure. In molecular doping work on diamond, Fermi-Dirac

statistics have been successfully applied to model occupancy of the molecular level into which the electron is transferred [100] [130] [127] [131], in this case the LUMO of MoO_3.

With all energies referenced to the vacuum level, the LUMO energy corresponds to the electron affinity, χ_{MoO_3} of neutral MoO_3 in contact with the Bi_2Se_3. Then the doping fraction η can be expressed as:

$$\eta = \frac{N_{A^-}}{N_A + N_{A^-}} = \frac{1}{\frac{1}{g}\exp\left[\frac{\Delta_0 + \Delta\phi + (E_D - E_F)}{k_B T}\right] + 1} \tag{5.3}$$

Here g is the degeneracy factor of the MoO_3 LUMO. As above N_{A^-} is equated with the change in electron density in Bi_2Se_3, and Δ_0 is the initial activation energy before charge transfer has taken place, given by $\Delta_0 = W_{F,Bi_2Se_3} + (E_F - E_D) - \chi_{MoO_3}$ where W_{F,Bi_2Se_3} is the work function of Bi_2Se_3. Eqn. 5.3 determines the value of Δ_0 from the coverage dependence of η or Δn.

Fig. 5.4(c) plots the experimentally determined $|\Delta n|$ as a function of MoO_3 coverage. The red circles represent the change in density determined using the values of E_F - E_D in Fig. 5.1(d) and Eqn. 5.2. The blue squares are derived making use of the relative intensities of the MoO_3 core level components to determine the number of charged MoO_3 molecules at each coverage (Fig. 5.2c). Overall the agreement between these two independently derived values is very good. The dashed line in Fig. 5.4(c) corresponds to the change in density calculated using Eqn. 5.3 with initial acceptor energy of Δ_0 = -0.15 $\pm$ 0.01 eV. For the as-cleaved Bi_2Se_3 the work function was measured to be W_F = 5.4 eV, and the initial position of the Dirac

point relative to the Fermi level, E_F - E_D = 0.27 eV. This yields a value for the electron affinity of neutral MoO_3, $\chi = 5.82 \pm 0.05$ eV.

5.3 Summary of Results

The molecule MoO_3 is an effective acceptor dopant for Bi_2Se_3. High-resolution synchrotron-based photoelectron spectroscopy measurements indicate that MoO_3 doping can bring the surface Fermi energy of Bi_2Se_3 to ∼100 meV above the Dirac point, within the so-called 'topological regime'. There are two distinct molecular charge components in the Mo 3d core level spectra corresponding to charged and uncharged MoO_3 molecules, allowing a direct measurement of the coverage-dependent charge transfer efficiency. A simple model of charge transfer to a discrete molecular level from the Bi_2Se_3 topological surface state accurately describes the coverage dependence of the Fermi energy and interface dipole, and gives an initial activation energy for charge transfer of -0.15 eV.

Chapter 6: MoO_3 Doping Electrical Transport Results

The XPS study from chapter 5 demonstrated the ability of molecular MoO_3 to put the Fermi level of Bi_2Se_3 into the topological regime with a low enough initial doping. I extended this work using the film growth and transport techniques from chapters 2 and 3 in pursuit of an air-stable "topological" device.

After a 15 nm Bi_2Se_3 film had been grown and characterized, the source was changed (while maintaining the sample in vacuum) to deposit an overlayer of MoO_3 while simultaneously measuring the carrier density. After the capping layer was deposited, the same measurement was continued as the sample was vented to ambient.

Fig. 6.1(a) shows the change in carrier density, $|\Delta n|$ (blue squares) and mobility, μ (green circles) of the Bi_2Se_3 film as a function of MoO_3 coverage. The behavior of the change in carrier density is almost identical to that observed on the as-cleaved Bi_2Se_3 studied with photoemission: a rapid increase in the change in carrier density at low coverage, followed by a saturation after deposition of $\sim$0.1 nm. The overall amount of transferred charge is also very similar at $\sim 10^{13}$ cm^{-2}. The mobility of the film increases to $\sim$430 cm^{2}V^{-1}s^{-1} at low MoO_3 coverages then once the charge transfer process saturates returns to the initial value of $\sim$390 cm^{2}V^{-1}s^{-1}, clear evidence that MoO_3 does not degrade the film quality. A further 100 nm of MoO_3 was

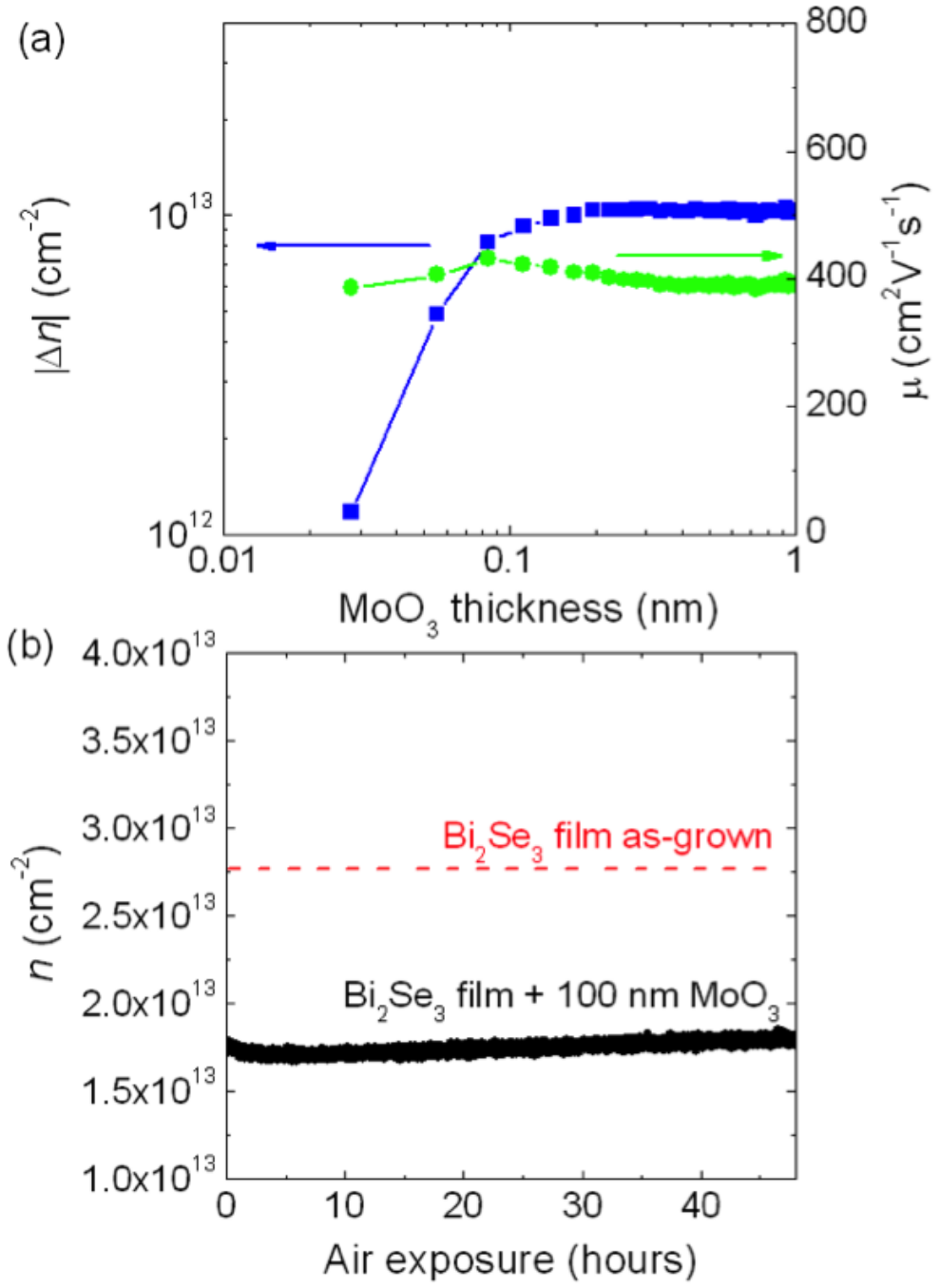

Figure 6.1: Air-stable acceptor doping of a Bi_2Se_3 film. (a) Change in carrier density $|\Delta n|$ determined from Hall effect measurements plotted as a function of MoO_3 thickness for an MBE-grown Bi_2Se_3 thin film. (b) Electron density of the Bi_2Se_3 film with 100 nm MoO_3 passivation layer plotted as a function of time the sample was exposed to ambient conditions (black circles). The red dashed line is a guide to the eye of the density of the as-grown film.

evaporated as a passivation layer, with negligible further change in carrier density. Following the deposition the film was exposed to atmosphere. Fig. 6.1(b) plots the carrier density as a function of exposure time to atmosphere (black circles), with the red dashed line the initial carrier density of the 15 nm film measured after growth but before MoO_3 deposition included as a reference. Over 48 hours the carrier density remains almost unchanged, with only $\sim$5 x 10^{11} cm^{-2} increase in density from the initial value upon atmosphere exposure of n = 1.75 x 10^{13} cm^{-2}. For N $\sim$ 6 different samples the same slow increase in density on exposure to ambient was observed, despite different initial values of the carrier density. This represents a retention of well over 90% of the initial electron depletion and still $\sim 10^{13}$ cm^{-2} lower than the n-type doping of the as-grown film. This time period is more than long enough for transfer to another cryostat or vacuum system, or deposition of additional capping layers. The change in carrier density, $|\Delta n|$, is quantitatively similar to that observed in photoemission for our Bi_2Se_3 crystal surfaces.

The thin film Bi_2Se_3 has higher doping than the single crystal material and hence higher E_F - E_D. The charge transfer saturation is limited primarily by the doping induced interface dipole, where $\Delta\phi \sim \Delta n$, hence we expect similar Δn, in agreement with the observation. This clearly demonstrates the effectiveness of MoO_3 as a passivation layer, protecting the Bi_2Se_3 from reaction with air, which is well known to increase the n-type doping [89] [132], and preserving the acceptor doping at the Bi_2Se_3-MoO_3 interface.

The exposure of MoO_3 to air results in a large decrease in the work function from 6.8 eV to 5.3 eV [133], which would limit the effectiveness of MoO_3 as an

electron acceptor. However, because the charge transfer process saturates well below 1 nm as seen from Fig. 6.1(a), the additional MoO_3 layers exposed to air play no role in surface transfer doping and simply act to prevent atmospheric species from reaching and reacting with either the MoO_3 molecules directly involved in charge transfer or the Bi_2Se_3 itself.

A thick (100 nm) passivation layer of MoO_3 can preserve the acceptor doping from MoO_3 and prevent degradation of Bi_2Se_3 when it is exposed to atmosphere, with the electron density remaining virtually unchanged after two days in ambient. These findings open up new pathways in Bi_2Se_3 devices, including electronic devices that not only operate in the topological regime but also are stable in air over prolonged periods of time.

Chapter 7: Final Summary, Conclusions, and Future Outlook

This project has demonstrated a viable pathway for measuring transport characteristics during epitaxial thin film growth. Contrary to expectation, Bi_2Se_3 is n-doped into the bulk conduction band as it grows in vacuum, before exposure to ambient. Furthermore, the data suggest that the majority of this undesirable doping occurs at the substrate-film and/or film-vacuum interfaces. The molecular doping work was a natural extension of these capabilities, demonstrating the efficacy of molecular MoO_3 as a p-dopant and capping layer against ambient exposure.

The achieved resistivity values of $\sim$1-3 mΩ·cm make these thin film samples very metallic compared to what has been done in creating bulk insulating single crystals ($\sim$60 mΩ·cm at low temperature, [54]), but comparable to other thin film efforts (for example, [115], [72]). The MoO_3 capping layer experiments showed nearly a factor of two increase in the sample resistivity. It would be interesting to see if this enhancement also happened with bulk crystals of Bi_2Se_3 or different topological insulator candidate materials.

The method of the measurement makes it difficult to be more specific about the nature of the doping (if it is the substrate or the vacuum interface, for example). Low temperature, high magnetic field, gated measurements could help to resolve this

ambiguity. The resulting Shubnikov-de Haas oscillations and non-linear magnetoresistance data can be fit to multiple carrier models that have been variously ascribed to bulk, top and bottom surface, and impurity channels (see for example, references in chapter 1.2.1.3, or appendix A), where the regime explored in this thesis has been limited to a single channel analysis. Gating of the top surface independently of the back surface could also providing clarifying data, but that would take substantial changes to the growth technique to avoid additional *ex situ* fabrication steps.

As the field moves forward in measuring spin effects of these topological states, re-engineering the growth stage for devices with contacts on the length scale of the spin coherence length would be an attractive capability. Work is already underway to prepare such a structure with *ex situ* lithography.

This is the first demonstration of growing film by MBE and measuring the *in situ* electrical properties. Beyond bismuth selenide, Na_3Bi has recently been predicted to behave like a Weyl semimetal [134] [135], evincing similar electronic properties to graphene, but in three dimensions instead of two. A glaring experimental complication is that sodium is a highly reactive alkali metal making the standard techniques of film growth and *ex situ* device preparation impossible. This novel, all-vacuum-side technique makes it possible to do electrical characterization of this material without exposure to air. Growth on $SrTiO_3$ substrate material would allow for effective back gating of the device at low temperature; using $Si:SiO_2$ as a (back-gateable) substrate is another possibility if growth is possible on an amorphous template.

The experience of this project has already partially informed the design of a

more powerful instrument incorporating aspects of this technique. Adding *in situ* transport to a combined MBE/ scanning tunneling microscopy (STM) system opens up exciting new experimental possibilities. This combination of techniques might be a necessary precursor to making spin-polarized STM measurements on topological insulators, as one example [136].

Appendix A: Localization and Magnetoresistence

A vast majority of the published low temperature transport data on topological insulators focusses on measurements of resistance versus magnetic field data, specifically weak anti-localization and weak localization. This is one of the best experimental signatures of 2D transport in a topological surface state. These phenomena, in the context of transport studies, were quantitatively explained by Hikami, Larkin and Nagaoka (HLN) [137]. This appendix briefly reviews this effect.

A.1 Weak Localization

Localization, or Anderson localization, is a quantum mechanical interference phenomenon occurring in low temperature, highly disordered systems. When electrons are in a disordered system, they undergo diffusive transport, scattering off the disorder sites. If the scattering is strong enough, coherent interference induced by the scattering will completely stop the macroscopic diffusion (the electrons are 'localized'). Figure (A.1) illustrates two such paths, whose constructive interference would lead to the electron getting stuck at A.

Weak localization, intuitively named, is a partial manifestation of this effect: constructive interference of the two paths leads to enhanced backscattering.

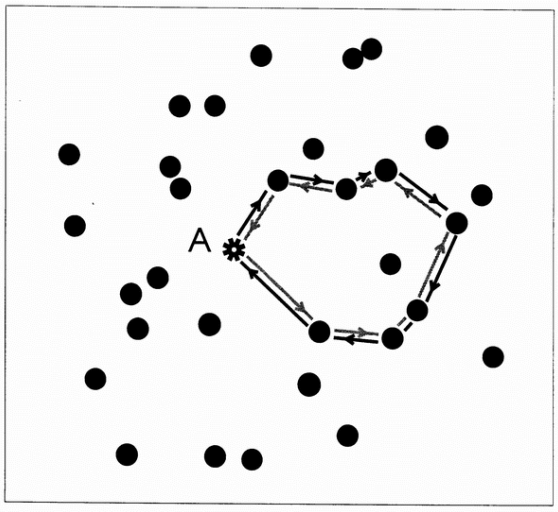

Figure A.1: Illustration of a scattering path of diffusive electron transport in a disordered system (clockwise arrows), with a coherent interfering path (counterclockwise arrows), leading to a tendency for the electron to 'dwell' at point A. Figure reproduced from reference [17].

This leads to an increase in resistivity beyond the classical (Drude) expectation. When a magnetic field is applied, the necessary presence of a magnetic potential introduces a phase to the counterpropagating wavefunctions (the Aharanov-Bohm effect), reversing their constructive interference, destroying the localization, lowering the resistivity. Magnetoresistance is therefore a way to experimentally measure weak localization.

A.2 Weak Anti-Localization

Weak anti-localization is the exact opposite of weak localization. If electron wavefunctions have an additional momentum-dependent phase, the two opposing 'paths' will destructively interfere, leading to a suppression of resistivity relative to the classical expectation. The application of a magnetic field will then increase

wavefunction coherence, increasing the resistivity.

The surface states of topological insulators exist as a result of the spin-orbit interaction. This coupling of spin and momentum means that electrons with opposite momentum have opposite spin direction, mathematically manifest as a π Berry phase in their wavefunctions. Weak anti-localization should then be the expected magnetoresistive effect for these materials.

In 1980, Hikami, Larkin and Nagaoka studied the spin-orbit interaction in two dimensions using the renormalization group method, obtaining the following result for the localization effects as a function of the magnetic field in the weak-field limit [137]:

$$\Delta\sigma = -\frac{\alpha e^2}{2\pi^2\hbar}[\ln\frac{1}{\tau_\epsilon a} - \psi(\frac{1}{2}+\frac{1}{\tau_\epsilon a})] \tag{A.1}$$

where τ_ϵ is the energy relaxation time, $a = 4DeH/\hbar c$ (D the diffusion constant, H the magnetic field). $\tau_\epsilon a$ is then proportional to the coherence length (owing to its relaxation time and diffusion constant dependence). ψ is the Digamma function. α is a parameter whose sign and magnitude determines whether it is weak localization (+1) or anti-localization (-1/2).

Bibliography

[1] M. Paalanen, D. Tsui, and A. Gossard. Quantized Hall effect at low temperatures. *Physical Review B*, 25(8):5566–5569, April 1982.

[2] Xiao Liang Qi and Shou Cheng Zhang. The quantum spin Hall effect and topological insulators. *Physics Today*, 63(1):33–38, 2010.

[3] Charles L. Kane and Eugene J. Mele. Physics. A new spin on the insulating state. *Science (New York, N.Y.)*, 314(5806):1692–3, December 2006.

[4] F. D. M. Haldane. Model for a Quantum Hall Effect without Landau Levels: Condensed-Matter Realization of the "Parity Anomaly". *Physical Review Letters*, 61(18):2015–2018, October 1988.

[5] Liang Fu, C. Kane, and E. Mele. Topological Insulators in Three Dimensions. *Physical Review Letters*, 98(10):1–4, March 2007.

[6] D Hsieh, D Qian, L Wray, Y Xia, Y S Hor, R J Cava, and M Z Hasan. A topological Dirac insulator in a quantum spin Hall phase. *Nature*, 452(7190):970–4, April 2008.

[7] Haijun Zhang, Chao-Xing Liu, Xiao-Liang Qi, Xi Dai, Zhong Fang, and Shou-Cheng Zhang. Topological insulators in Bi2Se3, Bi2Te3 and Sb2Te3 with a single Dirac cone on the surface. *Nature Physics*, 5(6):438–442, May 2009.

[8] Y. Xia, D. Qian, D. Hsieh, L. Wray, A. Pal, H. Lin, A. Bansil, D. Grauer, Y. S. Hor, R. J. Cava, and M. Z. Hasan. Observation of a large-gap topological-insulator class with a single Dirac cone on the surface. *Nature Physics*, 5(6):398–402, May 2009.

[9] Y. Hor, a. Richardella, P. Roushan, Y. Xia, J. Checkelsky, a. Yazdani, M. Hasan, N. Ong, and R. Cava. p-type Bi2Se3 for topological insulator and low-temperature thermoelectric applications. *Physical Review B*, 79(19):2–6, May 2009.

[10] Seung Sae Hong, Judy J Cha, Desheng Kong, and Yi Cui. Ultra-low carrier concentration and surface-dominant transport in antimony-doped BiSe topological insulator nanoribbons. *Nature communications*, 3:757, September 2012.

[11] H. Steinberg, J.-B. Laloë, V. Fatemi, J. Moodera, and P. Jarillo-Herrero. Electrically tunable surface-to-bulk coherent coupling in topological insulator thin films. *Physical Review B*, 84(23):5–8, December 2011.

[12] Dohun Kim, Sungjae Cho, Nicholas P. Butch, Paul Syers, Kevin Kirshenbaum, Shaffique Adam, Johnpierre Paglione, and Michael S. Fuhrer. Surface conduction of topological Dirac electrons in bulk insulating Bi2Se3. *Nature Physics*, 8(6):460–464, April 2012.

[13] T. Valla, Z.-H. Pan, D. Gardner, Y. Lee, and S. Chu. Photoemission Spectroscopy of Magnetic and Nonmagnetic Impurities on the Surface of the Bi_{2}Se_{3} Topological Insulator. *Physical Review Letters*, 108(11), March 2012.

[14] Z.-H. Zhu, G. Levy, B. Ludbrook, C. Veenstra, J. Rosen, R. Comin, D. Wong, P. Dosanjh, A. Ubaldini, P. Syers, N. Butch, J. Paglione, I. Elfimov, and A. Damascelli. Rashba Spin-Splitting Control at the Surface of the Topological Insulator Bi_{2}Se_{3}. *Physical Review Letters*, 107(18):1–5, October 2011.

[15] Mark T Edmonds. *Electronic properties of surface conducting hydrogen-terminated diamond*. PhD thesis, La Trobe University, 2013.

[16] Stefan Hüfner. *Photoelectron Spectroscopy*. Advanced Texts in Physics. Springer Berlin Heidelberg, Berlin, Heidelberg, 2003.

[17] Diederik S. Wiersma, Paolo Bartolini, Ad Lagendijk, and Roberto Righini. Localization of light in a disordered medium. *Nature*, 390(6661):671–673, December 1997.

[18] Yoichi Ando. Topological Insulator Materials. *Journal of the Physical Society of Japan*, 82(10):102001, October 2013.

[19] Xiao-Liang Qi and Shou-Cheng Zhang. Topological insulators and superconductors. *Reviews of Modern Physics*, 83(4):1057–1110, October 2011.

[20] Dimitrie Culcer. Transport in three-dimensional topological insulators: Theory and experiment. *Physica E: Low-dimensional Systems and Nanostructures*, 44(5):884–860, November 2011.

[21] Tomas Jungwirth, Jörg Wunderlich, and Kamil Olejník. Spin Hall effect devices. *Nature materials*, 11(5):382–90, May 2012.

[22] Dmytro Pesin and Allan H MacDonald. Spintronics and pseudospintronics in graphene and topological insulators. *Nature Materials*, 11(5):409–16, May 2012.

[23] M. Hasan and C. Kane. Colloquium: Topological insulators. *Reviews of Modern Physics*, 82(4):3045–3067, November 2010.

[24] K. Klitzing, G. Dorda, and M. Pepper. New Method for High-Accuracy Determination of the Fine-Structure Constant Based on Quantized Hall Resistance. *Physical Review Letters*, 45(6):494–497, August 1980.

[25] R. Laughlin. Quantized Hall conductivity in two dimensions. *Physical Review B*, 23(10):5632–5633, May 1981.

[26] D. DJ Thouless, M. Kohmoto, MP Nightingale, M. den Nijs, and M Den. Quantized Hall conductance in a two-dimentional periodic potential. *Physical Review Letters*, 49(6):405–408, August 1982.

[27] Shiing-shen Chern. On the Curvatura Integra in a Riemannian Manifold. *The Annals of Mathematics*, 46(4):674, October 1945.

[28] M. V. Berry. Quantal Phase Factors Accompanying Adiabatic Changes. *Proceedings of the Royal Society A: Mathematical, Physical and Engineering Sciences*, 392(1802):45–57, March 1984.

[29] J. Avron, R. Seiler, and B. Simon. Homotopy and Quantization in Condensed Matter Physics. *Physical Review Letters*, 51(1):51–53, July 1983.

[30] Qian Niu, D. Thouless, and Yong-Shi Wu. Quantized Hall conductance as a topological invariant. *Physical Review B*, 31(6):3372–3377, March 1985.

[31] S C Zhang and J Hu. A four-dimensional generalization of the quantum Hall effect. *Science (New York, N.Y.)*, 294(5543):823–8, October 2001.

[32] Shuichi Murakami, Naoto Nagaosa, and Shou-Cheng Zhang. Dissipationless quantum spin current at room temperature. *Science (New York, N.Y.)*, 301(5638):1348–51, September 2003.

[33] B. Andrei Bernevig and Shou-Cheng Zhang. Quantum Spin Hall Effect. *Physical Review Letters*, 96(10):1–4, March 2006.

[34] C. L. Kane and E. J. Mele. Z_{2} Topological Order and the Quantum Spin Hall Effect. *Physical Review Letters*, 95(14), September 2005.

[35] C. L. Kane and E. J. Mele. Quantum Spin Hall Effect in Graphene. *Physical Review Letters*, 95(22):1–4, November 2005.

[36] Yugui Yao, Fei Ye, Xiao-Liang Qi, Shou-Cheng Zhang, and Zhong Fang. Spin-orbit gap of graphene: First-principles calculations. *Physical Review B*, 75(4), January 2007.

[37] Cenke Xu and J. Moore. Stability of the quantum spin Hall effect: Effects of interactions, disorder, and Z2 topology. *Physical Review B*, 73(4), January 2006.

[38] B Andrei Bernevig, Taylor L Hughes, and Shou-Cheng Zhang. Quantum spin Hall effect and topological phase transition in HgTe quantum wells. *Science (New York, N.Y.)*, 314(5806):1757–61, December 2006.

[39] Markus König, Steffen Wiedmann, Christoph Brüne, Andreas Roth, Hartmut Buhmann, Laurens W Molenkamp, Xiao-Liang Qi, and Shou-Cheng Zhang. Quantum spin hall insulator state in HgTe quantum wells. *Science (New York, N.Y.)*, 318(5851):766–70, November 2007.

[40] J. Moore and L. Balents. Topological invariants of time-reversal-invariant band structures. *Physical Review B*, 75(12), March 2007.

[41] Tsuneya Ando, Takeshi Nakanishi, and Riichiro Saito. Berry's Phase and Absence of Back Scattering in Carbon Nanotubes. *Journal of the Physical Society of Japan*, 67(8):2857–2862, August 1998.

[42] Shuichi Murakami. Quantum Spin Hall Effect and Enhanced Magnetic Response by Spin-Orbit Coupling. *Physical Review Letters*, 97(23), December 2006.

[43] Liang Fu and C. Kane. Topological insulators with inversion symmetry. *Physical Review B*, 76(4):1–17, July 2007.

[44] Jeffrey Teo, Liang Fu, and C. Kane. Surface states and topological invariants in three-dimensional topological insulators: Application to Bi1xSbx. *Physical Review B*, 78(4), July 2008.

[45] P W Anderson. More is different. *Science (New York, N.Y.)*, 177(4047):393–6, August 1972.

[46] J.R. Wiese and L. Muldawer. Lattice constants of Bi2Te3-Bi2Se3 solid solution alloys. *Journal of Physics and Chemistry of Solids*, 15(1-2):13–16, August 1960.

[47] G.R. GR Hyde, HA H.A. Beale, I.L. IL Spain, and JA J.A. Woollam. Electronic properties of Bi2Se3 crystals. *Journal of Physics and*, 35(12):1719–1728, January 1974.

[48] V. a. Greanya, W. C. Tonjes, Rong Liu, C. G. Olson, D.-Y. Chung, and M. G. Kanatzidis. Determination of the valence band dispersions for Bi[sub 2]Se[sub 3] using angle resolved photoemission. *Journal of Applied Physics*, 92(11):6658, December 2002.

[49] SN Chizhevskaya and LE Shelimova. Electroactive and electroinactive dopants in. *Inorganic materials*, 1995.

[50] K S Novoselov, a K Geim, S V Morozov, D Jiang, Y Zhang, S V Dubonos, I V Grigorieva, and a a Firsov. Electric field effect in atomically thin carbon films. *Science (New York, N.Y.)*, 306(5696):666–9, October 2004.

[51] Guanhua Zhang, Huajun Qin, Jing Teng, Jiandong Guo, Qinlin Guo, Xi Dai, Zhong Fang, and Kehui Wu. Quintuple-layer epitaxy of thin films of topological insulator Bi[sub 2]Se[sub 3]. *Applied Physics Letters*, 95(5):053114, 2009.

[52] J. Chen, H. Qin, F. Yang, J. Liu, T. Guan, F. Qu, G. Zhang, J. Shi, X. Xie, C. Yang, K. Wu, Y. Li, and L. Lu. Gate-Voltage Control of Chemical Potential and Weak Antilocalization in Bi_{2}Se_{3}. *Physical Review Letters*, 105(17):1–4, October 2010.

[53] Yao-Yi Li, Guang Wang, Xie-Gang Zhu, Min-Hao Liu, Cun Ye, Xi Chen, Ya-Yu Wang, Ke He, Li-Li Wang, Xu-Cun Ma, Hai-Jun Zhang, Xi Dai, Zhong Fang, Xin-Cheng Xie, Ying Liu, Xiao-Liang Qi, Jin-Feng Jia, Shou-Cheng Zhang, and Qi-Kun Xue. Intrinsic topological insulator Bi2Te3 thin films on Si and their thickness limit. *Advanced materials (Deerfield Beach, Fla.)*, 22(36):4002–7, September 2010.

[54] Paul Syers and Johnpierre Paglione. Toward true bulk insulating behavior in a stoichiometric topological insulator. *ArXiv*, 2014.

[55] Chris Mann, Damien West, Ireneusz Miotkowski, Yong P. Chen, Shengbai Zhang, and Chih-Kang Shih. Mapping the 3D surface potential in Bi2Se3. *Nature Communications*, 4:2277, 2013.

[56] D Hsieh, Y Xia, D Qian, L Wray, J H Dil, F Meier, J Osterwalder, L Patthey, J G Checkelsky, N P Ong, a V Fedorov, H Lin, A Bansil, D Grauer, Y S Hor, R J Cava, and M Z Hasan. A tunable topological insulator in the spin helical Dirac transport regime. *Nature*, 460(7259):1101–5, August 2009.

[57] J. Checkelsky, Y. Hor, R. Cava, and N. Ong. Bulk Band Gap and Surface State Conduction Observed in Voltage-Tuned Crystals of the Topological Insulator Bi_{2}Se_{3}. *Physical Review Letters*, 106(19), May 2011.

[58] Yi Zhang, Cui-Zu Chang, Ke He, Li-Li Wang, Xi Chen, Jin-Feng Jia, Xu-Cun Ma, and Qi-Kun Xue. Doping effects of Sb and Pb in epitaxial topological insulator Bi[sub 2]Se[sub 3] thin films: An in situ angle-resolved photoemission spectroscopy study. *Applied Physics Letters*, 97(19):194102, November 2010.

[59] A. A. Taskin, Zhi Ren, Satoshi Sasaki, Kouji Segawa, and Yoichi Ando. Observation of Dirac Holes and Electrons in a Topological Insulator. *Physical Review Letters*, 107(1):016801, June 2011.

[60] Sunghun Kim, Shunsuke Yoshizawa, Yukiaki Ishida, Kazuma Eto, Kouji Segawa, Yoichi Ando, Shik Shin, and Fumio Komori. Unexpectedly robust protection from backscattering in the topological insulator Bi$_{1.5}$Sb$_{0.5}$Te$_{1.7}$Se$_{1.3}$. *ArXiv*, November 2013.

[61] H Lin, Tanmoy Das, L A Wray, S-Y Xu, M Z Hasan, and A Bansil. An isolated Dirac cone on the surface of ternary tetradymite-like topological insulators. *New Journal of Physics*, 13(9):095005, September 2011.

[62] Wei Wang, Li Li, Wenqin Zou, Liang He, Fengqi Song, Rong Zhang, Xiaoshan Wu, and Fengming Zhang. Intrinsic Topological Insulator Bi1.5Sb0.5Te3-xSex Thin Crystals. *Scientific Reports*, 5:7931, 2015.

[63] Su-Yang Xu, L. A. Wray, Y. Xia, R. Shankar, A. Petersen, A. Fedorov, H. Lin, A. Bansil, Y. S. Hor, D. Grauer, R. J. Cava, and M. Z. Hasan. Discovery of several large families of Topological Insulator classes with backscattering-suppressed spin-polarized single-Dirac-cone on the surface. *ArXiv*, page 11, July 2010.

[64] M. Neupane, S.-Y. Xu, L. A. Wray, A. Petersen, R. Shankar, N. Alidoust, Chang Liu, A. Fedorov, H. Ji, J. M. Allred, Y. S. Hor, T.-R. Chang, H.-T. Jeng, H. Lin, A. Bansil, R. J. Cava, and M. Z. Hasan. Topological surface states and Dirac point tuning in ternary topological insulators. *Physical Review B*, 85(23):235406, June 2012.

[65] Chandra Shekhar, C. E. Viol Barbosa, Binghai Yan, Siham Ouardi, W. Schnelle, Gerhard H. Fecher, and Claudia Felser. Evidence of surface transport and weak antilocalization in a single crystal of the Bi2Te2Se topological insulator. *Physical Review B*, 90(16):165140, October 2014.

[66] Janghee Lee, Joonbum Park, Jae Hyeong Lee, Jun Sung Kim, and Hu Jong Lee. Gate-tuned differentiation of surface-conducting states in Bi 1.5Sb0.5Te1.7Se1.3 topological-insulator thin crystals. *Physical Review B - Condensed Matter and Materials Physics*, 86, 2012.

[67] Wonhee Ko, Insu Jeon, Hyo Won Kim, Hyeokshin Kwon, Se-Jong Kahng, Joonbum Park, Jun Sung Kim, Sung Woo Hwang, and Hwansoo Suh. Atomic and electronic structure of an alloyed topological insulator, Bi1.5Sb0.5Te1.7Se1.3. *Scientific Reports*, 3:2656, 2013.

[68] T. Arakane, T. Sato, S. Souma, K. Kosaka, K. Nakayama, M. Komatsu, T. Takahashi, Zhi Ren, Kouji Segawa, and Yoichi Ando. Tunable Dirac cone in the topological insulator Bi2-xSbxTe3-ySey, 2012.

[69] Desheng Kong, Jason C Randel, Hailin Peng, Judy J Cha, Stefan Meister, Keji Lai, Yulin Chen, Zhi-Xun Shen, Hari C Manoharan, and Yi Cui. Topological insulator nanowires and nanoribbons. *Nano letters*, 10(1):329–33, January 2010.

[70] Hongtao Yuan, Hongwen Liu, Hidekazu Shimotani, Hua Guo, Mingwei Chen, Qikun Xue, and Yoshihiro Iwasa. Liquid-gated ambipolar transport in ultrathin films of a topological insulator Bi2Te3. *Nano letters*, 11(7):2601–5, July 2011.

[71] J. Chen, X. He, K. Wu, Z. Ji, L. Lu, J. Shi, J. Smet, and Y. Li. Tunable surface conductivity in Bi_{2}Se_{3} revealed in diffusive electron transport. *Physical Review B*, 83(24):5, June 2011.

[72] Namrata Bansal, Yong Kim, Matthew Brahlek, Eliav Edrey, and Seongshik Oh. Thickness-Independent Transport Channels in Topological Insulator Bi_{2}Se_{3} Thin Films. *Physical Review Letters*, 109(11), September 2012.

[73] Hadar Steinberg, Dillon R Gardner, Young S Lee, and Pablo Jarillo-Herrero. Surface State Transport and Ambipolar Electric Field Effect in Bi(2)Se(3) Nanodevices. *Nano letters*, 10(12):5032–5036, November 2010.

[74] Brian Skinner, Tianran Chen, and B. Shklovskii. Why Is the Bulk Resistivity of Topological Insulators So Small? *Physical Review Letters*, 109(17), October 2012.

[75] Qin Liu, Chao-Xing Liu, Cenke Xu, Xiao-Liang Qi, and Shou-Cheng Zhang. Magnetic Impurities on the Surface of a Topological Insulator. *Physical Review Letters*, 102(15), April 2009.

[76] Tome Schmidt, R. Miwa, and A. Fazzio. Spin texture and magnetic anisotropy of Co impurities in Bi_{2}Se_{3} topological insulators. *Physical Review B*, 84(24), December 2011.

[77] J. Henk, A. Ernst, S. Eremeev, E. Chulkov, I. Maznichenko, and I. Mertig. Complex Spin Texture in the Pure and Mn-Doped Topological Insulator Bi_{2}Te_{3}. *Physical Review Letters*, 108(20), May 2012.

[78] L. Andrew Wray, Su-Yang Xu, Yuqi Xia, David Hsieh, Alexei V. Fedorov, Yew San Hor, Robert J. Cava, Arun Bansil, Hsin Lin, and M. Zahid Hasan. A topological insulator surface under strong Coulomb, magnetic and disorder perturbations. *Nature Physics*, 7(1):32–37, December 2010.

[79] Y. L. Chen, J-H Chu, J. G. Analytis, Z. K. Liu, K. Igarashi, H-H Kuo, X. L. Qi, S. K. Mo, R. G. Moore, D. H. Lu, M. Hashimoto, T. Sasagawa, S. C. Zhang, I. R. Fisher, Z. Hussain, and Z. X. Shen. Massive Dirac fermion on the surface of a magnetically doped topological insulator. *Science (New York, N.Y.)*, 329(5992):659–62, August 2010.

[80] M. Scholz, J. Sánchez-Barriga, D. Marchenko, A. Varykhalov, A. Volykhov, L. Yashina, and O. Rader. Tolerance of Topological Surface States towards Magnetic Moments: Fe on Bi_{2}Se_{3}. *Physical Review Letters*, 108(25):10, June 2012.

[81] J. Honolka, A. Khajetoorians, V. Sessi, T. Wehling, S. Stepanow, J.-L. Mi, B. Iversen, T. Schlenk, J. Wiebe, N. Brookes, A. Lichtenstein, Ph. Hofmann, K. Kern, and R. Wiesendanger. In-Plane Magnetic Anisotropy of Fe Atoms on Bi_{2}Se_{3}(111). *Physical Review Letters*, 108(25), June 2012.

[82] L. Shelford, T. Hesjedal, L. Collins-McIntyre, S. Dhesi, F. Maccherozzi, and G. van der Laan. Electronic structure of Fe and Co magnetic adatoms on Bi_{2}Te_{3} surfaces. *Physical Review B*, 86(8), August 2012.

[83] M. Ye, S. Eremeev, K. Kuroda, E. Krasovskii, E. Chulkov, Y. Takeda, Y. Saitoh, K. Okamoto, S. Zhu, K. Miyamoto, M. Arita, M. Nakatake, T. Okuda, Y. Ueda, K. Shimada, H. Namatame, M. Taniguchi, and A. Kimura. Quasiparticle interference on the surface of Bi_{2}Se_{3} induced by cobalt adatom in the absence of ferromagnetic ordering. *Physical Review B*, 85(20), May 2012.

[84] Minhao Liu, Jinsong Zhang, Cui-Zu Chang, Zuocheng Zhang, Xiao Feng, Kang Li, Ke He, Li-li Wang, Xi Chen, Xi Dai, Zhong Fang, Qi-Kun Xue, Xucun Ma, and Yayu Wang. Crossover between Weak Antilocalization and Weak Localization in a Magnetically Doped Topological Insulator. *Physical Review Letters*, 108(3):1–5, January 2012.

[85] Duming Zhang, Anthony Richardella, David Rench, Su-Yang Xu, Abhinav Kandala, Thomas Flanagan, Haim Beidenkopf, Andrew Yeats, Bob Buckley, Paul Klimov, David Awschalom, Ali Yazdani, Peter Schiffer, M. Hasan, and Nitin Samarth. Interplay between ferromagnetism, surface states, and quantum corrections in a magnetically doped topological insulator. *Physical Review B*, 86(20):205127, November 2012.

[86] Joseph G. Checkelsky, Jianting Ye, Yoshinori Onose, Yoshihiro Iwasa, and Yoshinori Tokura. Dirac-fermion-mediated ferromagnetism in a topological insulator. *Nature Physics*, advance on, August 2012.

[87] Tong Zhang, Peng Cheng, Xi Chen, Jin-Feng Jia, Xucun Ma, Ke He, Lili Wang, Haijun Zhang, Xi Dai, Zhong Fang, Xincheng Xie, and Qi-Kun Xue. Experimental Demonstration of Topological Surface States Protected by Time-Reversal Symmetry. *Physical Review Letters*, 103(26):1–4, December 2009.

[88] M. Ye, S. V. Eremeev, K. Kuroda, M. Nakatake, S. Kim, Y. Yamada, E. E. Krasovskii, E. V. Chulkov, M. Arita, H. Miyahara, T. Maegawa, K. Okamoto, K. Miyamoto, T. Okuda, K. Shimada, H. Namatame, M. Taniguchi, Y. Ueda, and A. Kimura. Relocation of the topological surface state of Bi$_{2}$Se$_{3}$ beneath the surface by Ag intercalation. *ArXiv*, page 5, December 2011.

[89] Desheng Kong, Judy J. Cha, Keji Lai, Hailin Peng, James G. Analytis, Stefan Meister, Yulin Chen, Hai-Jun Zhang, Ian R. Fisher, Zhi-Xun Shen, and Yi Cui.

Rapid Surface Oxidation as a Source of Surface Degradation Factor for Bi2Se3. *ACS nano*, 5(6):4698–703, February 2011.

[90] Hadj Benia, Chengtian Lin, Klaus Kern, and Christian Ast. Reactive Chemical Doping of the Bi_{2}Se_{3} Topological Insulator. *Physical Review Letters*, 107(17):4, October 2011.

[91] Chaoyu Chen, Shaolong He, Hongming Weng, Wentao Zhang, Lin Zhao, Haiyun Liu, Xiaowen Jia, Daixiang Mou, Shanyu Liu, Junfeng He, Yingying Peng, Ya Feng, Zhuojin Xie, Guodong Liu, Xiaoli Dong, Jun Zhang, Xiaoyang Wang, Qinjun Peng, Zhimin Wang, Shenjin Zhang, Feng Yang, Chuangtian Chen, Zuyan Xu, Xi Dai, Zhong Fang, and X J Zhou. Robustness of topological order and formation of quantum well states in topological insulators exposed to ambient environment. *Proceedings of the National Academy of Sciences of the United States of America*, 109(10):3694–8, March 2012.

[92] Matthew Brahlek, Yong Seung Kim, Namrata Bansal, Eliav Edrey, and Seongshik Oh. Surface versus bulk state in topological insulator Bi2Se3 under environmental disorder. *Applied Physics Letters*, 99(1):012109, July 2011.

[93] Xiaoxiong Wang, Guang Bian, T. Miller, and T.-C. Chiang. Fragility of Surface States and Robustness of Topological Order in Bi_{2}Se_{3} against Oxidation. *Physical Review Letters*, 108(9), February 2012.

[94] Marco Bianchi, Richard C Hatch, Zheshen Li, Philip Hofmann, Fei Song, Jianli Mi, Bo B Iversen, Zakaria M Abd El-Fattah, Peter Löptien, Lihui Zhou, Alexander A Khajetoorians, Jens Wiebe, Roland Wiesendanger, and Justin W Wells. Robust Surface Doping of Bi(2)Se(3) by Rubidium Intercalation. *ACS nano*, August 2012.

[95] Murong Lang, Liang He, Faxian Xiu, Xinxin Yu, Jianshi Tang, Yong Wang, Xufeng Kou, Wanjun Jiang, Alexei V Fedorov, and Kang L Wang. Revelation of topological surface states in Bi2Se3 thin films by in situ Al passivation. *ACS nano*, 6(1):295–302, January 2012.

[96] Namrata Bansal, Yong Seung Kim, Eliav Edrey, Matthew Brahlek, Yoichi Horibe, Keiko Iida, Makoto Tanimura, Guo-Hong Li, Tian Feng, Hang-Dong Lee, Torgny Gustafsson, Eva Andrei, and Seongshik Oh. Epitaxial growth of topological insulator Bi2Se3 film on Si(111) with atomically sharp interface. *Thin Solid Films*, 520(1):224–229, October 2011.

[97] Jixia Dai, Wenbo Wang, Matthew Brahlek, Nikesh Koirala, Maryam Salehi, Seongshik Oh, and Weida Wu. Restoring pristine Bi2Se3 surfaces with an effective Se decapping process. *Nano Research*, 2014.

[98] Su-Yang Xu, Nasser Alidoust, Ilya Belopolski, Anthony Richardella, Chang Liu, Madhab Neupane, Guang Bian, Song-Hsun Huang, Raman Sankar, Chen Fang, Brian Dellabetta, Wenqing Dai, Qi Li, Matthew J. Gilbert, Fangcheng

Chou, Nitin Samarth, and M. Zahid Hasan. Momentum-space imaging of Cooper pairing in a half-Dirac-gas topological superconductor. *Nature Physics*, 2014.

[99] N. V. Tarakina, S Schreyeck, T. Borzenko, C. Schumacher, G. Karczewski, K. Brunner, C. Gould, H. Buhmann, and L. W. Molenkamp. Comparative Study of the Microstructure of Bi 2 Se 3 Thin Films Grown on Si(111) and InP(111) Substrates. *Crystal Growth & Design*, 12:1913–1918, 2012.

[100] P Strobel, M Riedel, J Ristein, and L Ley. Surface transfer doping of diamond. *Nature*, 430(6998):439–41, July 2004.

[101] Mark T Greiner, Michael G Helander, Wing-Man Tang, Zhi-Bin Wang, Jacky Qiu, and Zheng-Hong Lu. Universal energy-level alignment of molecules on metal oxides. *Nature materials*, 11(1):76–81, January 2012.

[102] A. Tadich, M. T. Edmonds, L. Ley, F. Fromm, Y. Smets, Z. Mazej, J. Riley, C. I. Pakes, Th. Seyller, and M. Wanke. Tuning the charge carriers in epitaxial graphene on SiC(0001) from electron to hole via molecular doping with C60F48. *Applied Physics Letters*, 102(24):241601, June 2013.

[103] Yaou Smets, Christian B. Stark, Felix Schmitt, Mark T. Edmonds, Stefan Lach, Christopher A. Wright, Daniel P. Langley, Kevin J. Rietwyk, Alex Schenk, Anton Tadich, Martina Wanke, Christiane Ziegler, Lothar Ley, and Christopher I. Pakes. Doping efficiency and energy-level scheme in C60F48-doped zinctetraphenylporphyrin films. *Organic Electronics*, 14(1):169–174, January 2013.

[104] Dohun Kim, Qiuzi Li, Paul Syers, Nicholas P. Butch, Johnpierre Paglione, S. Das Sarma, and Michael S. Fuhrer. Intrinsic Electron-Phonon Resistivity of Bi_{2}Se_{3} in the Topological Regime. *Physical Review Letters*, 109(16):166801, October 2012.

[105] Dohun Kim, Paul Syers, Nicholas P. Butch, Johnpierre Paglione, and Michael S. Fuhrer. Coherent topological transport on the surface of BiSe. *Nature communications*, 4:2040, January 2013.

[106] S. Adam, E. Hwang, and S. Das Sarma. Two-dimensional transport and screening in topological insulator surface states. *Physical Review B*, 85(23):235413–, June 2012.

[107] Haim Beidenkopf, Pedram Roushan, Jungpil Seo, Lindsay Gorman, Ilya Drozdov, Yew San Hor, R. J. Cava, and Ali Yazdani. Spatial fluctuations of helical Dirac fermions on the surface of topological insulators. *Nature Physics*, 7(12):939–943, October 2011.

[108] Gregory A Fiete. Topological insulators: Crystalline protection. *Nature materials*, 11(12):1003–4, November 2012.

[109] Jack Hellerstedt, J. H. Chen, Dohun Kim, William G. Cullen, C. X. Zheng, and Michael S. Fuhrer. In situ monitoring of resistivity and carrier concentration during molecular beam epitaxy of topological insulator Bi 2 Se 3. In James Friend and H. Hoe Tan, editors, *SPIE 8923, Micro/Nano Materials, Devices, and Systems*, page 89230P, December 2013.

[110] Jack Hellerstedt, Mark T. Edmonds, J. H. Chen, William G. Cullen, C. X. Zheng, and Michael S. Fuhrer. Thickness and growth-condition dependence of in-situ mobility and carrier density of epitaxial thin-film Bi2Se3. *Applied Physics Letters*, 105(17):173506, October 2014.

[111] Mark T. Edmonds, Jack T. Hellerstedt, Anton Tadich, Alex Schenk, Kane Michael O'Donnell, Jacob Tosado, Nicholas P. Butch, Paul Syers, Johnpierre Paglione, and Michael S. Fuhrer. Air-Stable Electron Depletion of Bi2Se3 Using Molybdenum Trioxide into the Topological Regime. *ACS Nano*, 8(6):6400–6406, June 2014.

[112] Jaewan Chang, Yoon-Seok Park, and Sang-Koog Kim. Atomically flat single-terminated SrTiO[sub 3] (111) surface. *Applied Physics Letters*, 92(15):152910, 2008.

[113] MA Saifi and LE Cross. Dielectric Properties of Strontium Titanate. *Physical Review B*, 1970.

[114] M. Kawasaki, A. Ohtomo, T. Arakane, K. Takahashi, M. Yoshimoto, and H. Koinuma. Atomic control of SrTiO3 surface for perfect epitaxy of perovskite oxides. *Applied Surface Science*, 107:102–106, November 1996.

[115] Yong Seung Kim, Matthew Brahlek, Namrata Bansal, Eliav Edrey, Gary A. Kapilevich, Keiko Iida, Makoto Tanimura, Yoichi Horibe, Sang-Wook Cheong, and Seongshik Oh. Thickness-dependent bulk properties and weak antilocalization effect in topological insulator Bi_{2}Se_{3}. *Physical Review B*, 84(7):073109, August 2011.

[116] Namrata Bansal, Yong Seung Kim, Eliav Edrey, Matthew Brahlek, Yoichi Horibe, Keiko Iida, Makoto Tanimura, Guo-Hong Li, Tian Feng, Hang-Dong Lee, Torgny Gustafsson, Eva Andrei, and Seongshik Oh. Epitaxial growth of topological insulator Bi2Se3 film on Si(111) with atomically sharp interface. *Thin Solid Films*, 520(1):224–229, October 2011.

[117] A. Taskin, Satoshi Sasaki, Kouji Segawa, and Yoichi Ando. Manifestation of Topological Protection in Transport Properties of Epitaxial Bi_{2}Se_{3} Thin Films. *Physical Review Letters*, 109(6):066803, August 2012.

[118] Guanhua Zhang, Huajun Qin, Jun Chen, Xiaoyue He, Li Lu, Yongqing Li, and Kehui Wu. Growth of Topological Insulator Bi2Se3 Thin Films on SrTiO3 with Large Tunability in Chemical Potential. *Advanced Functional Materials*, 21(12):2351–2355, June 2011.

[119] H D Li, Z Y Wang, X Kan, X Guo, H T He, Z Wang, J N Wang, T L Wong, N Wang, and M H Xie. The van der Waals epitaxy of Bi 2 Se 3 on the vicinal Si(111) surface: an approach for preparing high-quality thin films of a topological insulator. *New Journal of Physics*, 12(10):103038, October 2010.

[120] N. P. Butch, K. Kirshenbaum, P. Syers, a. B. Sushkov, G. S. Jenkins, H. D. Drew, and J. Paglione. Strong surface scattering in ultrahigh-mobility Bi_{2}Se_{3} topological insulator crystals. *Physical Review B*, 81(24):241301, June 2010.

[121] Stephen Evans. Curve synthesis and optimization procedures for X-ray photoelectron spectroscopy. *Surface and Interface Analysis*, 17(2):85–93, February 1991.

[122] D. Shirley. High-Resolution X-Ray Photoemission Spectrum of the Valence Bands of Gold. *Physical Review B*, 5(12):4709–4714, June 1972.

[123] S Doniach and M Sunjic. Many-electron singularity in X-ray photoemission and X-ray line spectra from metals. *Journal of Physics C: Solid State Physics*, 3(2):285–291, February 1970.

[124] Kenta Kuroda, Mao Ye, Eike Schwier, Munisa Nurmamat, Kaito Shirai, Masashi Nakatake, Shigenori Ueda, Koji Miyamoto, Taichi Okuda, Hirofumi Namatame, Masaki Taniguchi, Yoshifumi Ueda, and Akio Kimura. Experimental verification of the surface termination in the topological insulator TlBiSe2 using core-level photoelectron spectroscopy and scanning tunneling microscopy. *Physical Review B*, 88(24):245308, December 2013.

[125] Michael Kröger, Sami Hamwi, Jens Meyer, Thomas Riedl, Wolfgang Kowalsky, and Antoine Kahn. P-type doping of organic wide band gap materials by transition metal oxides: A case-study on Molybdenum trioxide. *Organic Electronics*, 10(5):932–938, August 2009.

[126] C. Coletti, C. Riedl, D. S. Lee, B. Krauss, L. Patthey, K. von Klitzing, J. H. Smet, and U. Starke. Charge neutrality and band-gap tuning of epitaxial graphene on SiC by molecular doping. *Physical Review B*, 81(23):1–8, June 2010.

[127] M T Edmonds, M Wanke, A Tadich, H M Vulling, K J Rietwyk, P L Sharp, C B Stark, Y Smets, A Schenk, Q-H Wu, L Ley, and C I Pakes. Surface transfer doping of hydrogen-terminated diamond by C60F48: energy level scheme and doping efficiency. *The Journal of chemical physics*, 136(12):124701, March 2012.

[128] Kourosh Kalantar-zadeh, Jianshi Tang, Minsheng Wang, Kang L Wang, Alexandros Shailos, Kosmas Galatsis, Robert Kojima, Veronica Strong, Andrew Lech, Wojtek Wlodarski, and Richard B Kaner. Synthesis of nanometre-thick MoO3 sheets. *Nanoscale*, 2(3):429–33, March 2010.

[129] K. Kuroda, M. Arita, K. Miyamoto, M. Ye, J. Jiang, A. Kimura, E. E. Krasovskii, E. V. Chulkov, H. Iwasawa, T. Okuda, K. Shimada, Y. Ueda, H. Namatame, and M. Taniguchi. Hexagonally Deformed Fermi Surface of the 3D Topological Insulator Bi_{2}Se_{3}. *Physical Review Letters*, 105(7):076802, August 2010.

[130] Paul Strobel, Marc Riedel, Jürgen Ristein, Lothar Ley, and Olga Boltalina. Surface transfer doping of diamond by fullerene. *Diamond and Related Materials*, 14(3-7):451–458, March 2005.

[131] Lothar Ley, Yaou Smets, Christopher I. Pakes, and Jürgen Ristein. Calculating the Universal Energy-Level Alignment of Organic Molecules on Metal Oxides. *Advanced Functional Materials*, 23(7):794–805, February 2013.

[132] James G. Analytis, Ross D. McDonald, Scott C. Riggs, Jiun-Haw Chu, G. S. Boebinger, and Ian R. Fisher. Two-dimensional surface state in the quantum limit of a topological insulator. *Nature Physics*, 6(12):960–964, November 2010.

[133] Lanfei Xie, Xiao Wang, Hongying Mao, Rui Wang, Mianzhi Ding, Yu Wang, Barbaros Ozyilmaz, Kian Ping Loh, Andrew T. S. Wee, and Wei Chen. Electrical measurement of non-destructively p-type doped graphene using molybdenum trioxide. *Applied Physics Letters*, 99(1):012112, 2011.

[134] S. M. Young, S. Zaheer, J. C. Y. Teo, C. L. Kane, E. J. Mele, and A. M. Rappe. Dirac Semimetal in Three Dimensions. *Physical Review Letters*, 108(14):140405, April 2012.

[135] Zhijun Wang, Yan Sun, Xing-Qiu Chen, Cesare Franchini, Gang Xu, Hongming Weng, Xi Dai, and Zhong Fang. Dirac semimetal and topological phase transitions in A_{3}Bi (A=Na, K, Rb). *Physical Review B*, 85(19):195320, May 2012.

[136] K. Saha, Sourin Das, K. Sengupta, and Diptiman Sen. Spin-polarized STM spectra of Dirac electrons on the surface of a topological insulator. *Physical Review B*, 84(16):165439, October 2011.

[137] Shinobu Hikami, Anatoly I. Larkin, and Yosuke Nagaoka. Spin-Orbit Interaction and Magnetoresistance in the Two Dimensional Random System. *Progress of Theoretical Physics*, 63(2):707–710, February 1980.